Fall 12-2020

Parametric Study of Residual Stresses in Wire and Arc Additive Manufactured Parts

Hisham Khaled Jamil Abusalma
Old Dominion University, habus001@odu.edu

PARAMETRIC STUDY OF RESIDUAL STRESSES IN WIRE AND ARC ADDITIVE MANUFACTURED PARTS

by

Hisham Khaled Jamil Abusalma
B.S. August 2018, Hashemite University, Jordan

A Thesis Submitted to the Faculty of
Old Dominion University in Partial Fulfilment of
Requirements for the Degree of

MASTER OF SCIENCE

MECHANICAL & AEROSPACE ENGINEERING

OLD DOMINION UNIVERSITY
December 2020

Approved by:

Dr. Abdelmageed Elmustafa (Co-Chair)

Dr. Sebastian Y. Bawab (Member)

Dr. Vukica Jovanovic (Member)

Dr. Hamid Eisazadeh (Co-Chair)

ABSTRACT

PARAMETRIC STUDY OF RESIDUAL STRESSES IN WIRE AND ARC ADDITIVE MANUFACTURED PARTS

Hisham Khaled Jamil Abusalma
Old Dominion University, 2020
Advisor: Dr. Hamid Eisazadeh

Wire and Arc Additive Manufacturing (WAAM) is a cost-effective additive manufacturing process due to its capability to fabricate large metal parts with high deposition rate and low equipment cost. Although this method is gaining popularity in manufacturing industry, more research is needed to understand process parameters' effects on residual stress (RS) distribution and part distortion. As such, a 3D thermo-elastic-plastic transient model was established in ABAQUS and employed to investigate the effect of process parameters such as the torch speed, the deposition power and the interlayer dwell time on RS distribution and distortion in WAAM part. The numerical model utilized a comprehensive three-dimensional transient heat transfer model to calculate the temperature distribution and gradient in WAAM process for various process parameters. The heat source was reproduced by a user subroutine DFLUX in ABAQUS. The calculated temperature was exported into mechanical model to predict residual stress and distortion. Variation of microstructural morphology in WAAM components is also critical as it can influence RS in the part. Therefore, the USDFLD user subroutine was utilized to incorporate mechanical property change due to microstructure variation in the mechanical analysis. Both thermal and mechanical models were validated with the experimental data. A 30-layer high wall was built using a GMA-WAAM process with a collaboration with students at Clarkson University.

The WAAM setup utilized a gas metal arc welding process for deposition of hot 718 Inconel electrode on a A36 steel substrate. Temperature histories, which is necessary for validating the thermal model, were collected at five locations on the substrate. Lattice spacing for strain calculation was measured by neutron diffraction technique on ex-situ basis, at Oak Ridge National Laboratory. The numerical results showed process parameters can induce significant impact on RS and distortion in the WAAM part. As such, these parameters should be optimized to produce WAAM parts with low RS.

I dedicate this thesis to my family whom without their support I would not have succeeded, especially my loving parents, Khaled Abusalma and Eman Haj-Hassan.

I would also like to give thanks to my advisor Dr. Hamid Eisazadeh who was an excellent mentor and provided me with financial assistant I needed to complete my degree.

I want to extend thanks to my close friends who supported me during my work especially Abdulrahman Al-Badawi, Mohammad Shabara, Ahmad Al-Shammari, Yousef Al-Sharif, and Tariq Al-Jawhari.

Special thanks to Dr. Usama Hussain and Dr. Ameera Yousef for their continuous support throughout my master's studies.

I wish to thank my committee members for their time guiding the research and editing the manuscript. I wish to extend thanks to my advisor Dr. Hamid Eisazadeh for his outstanding advice and efforts. I also want to acknowledge the efforts of Dr. Fatemeh Hejripour at Binghamton University and Dr. Daryush Aidun at Clarkson University for conducting the experiment and providing the data. I want to also thank Mr. Paris Cornwell, Dr. Jeff Bunn and Dr. Andrew Payzant at Oak Ridge National Laboratories for providing their expertise in Neutron Diffraction measurements and conducting the measurements on the sample part.

TABLE OF CONTENTS

Page

LIST OF TABLES ix

LIST OF FIGURES x

I. INTRODUCTION 14

Categories of metallic AM 15

Defects and disadvantages of AM for metals 17

Wire and Arc Additive Manufacturing (WAAM) 19

Literature review 21

History of WAAM 21

Types of WAAM processes 21

Materials used with WAAM 23

Previous work 25

II. EXPERIMENTAL SETUP 27

Neutron diffraction (ND) measurement 30

III. NUMERICAL MODELING 32

Mechanics and mathematical model 32

Thermal model 34

Mechanical model 35

Microstructural model 38

Numerical model 39

Thermal analysis 40
Microstructural analysis 53
Mechanical analysis 55
IV. RESULTS AND DISCUSSION 56
Experimental results and model validation 56
Thermal analysis 56
Microstructure analysis 61
Mechanical analysis 65
Parametric study 72
Travel speed 72
Input power 80
Interlayer dwell time 88
V. CONCLUSION AND FUTURE WORK 97
REFERENCES 99

LIST OF TABLES

Table Page

1. WAAM process parameters 29

2. Thermo-physical properties of Inconel 718 [11],[40] 43

3. Thermo-physical properties of A36 [41] 43

4. Heat source parameters 52

5. Heat input at different travel speeds using 1850 and 1000 Watts of power 72

6. Heat input per unit length using different input powers and 9 mm/s travel speed 80

LIST OF FIGURES

Figure Page

1. Schematic diagram of laser DED using powder 16

2. Schematic diagram of WAAM process 19

3. Diagram of AM process using PAW 23

4. Detailed dimensioning of the WAAM wall and the location of thermocouples on the substrate 27

5. Illustration of welding direction for WAAM wall 28

6. The AM part after completion with thermocouples attached (Done at Clarkson University) .. 28

7. The final AM part in scale (Done at Clarkson University) 29

8. Vickers hardness test indentations on the sample (Done at Clarkson University) 30

9. Measurement setup using ND in different directions 31

10. Relation between different fields in the welding process The solid lines represent a strong relation and the dashed lines represent a weak relation 33

11. The relationship between the clamping and residual stresses 36

12. Rod-spring model illustrating the residual stress inside the material 38

13. An illustration that shows the direction of the grain growth (R), solidification velocity (V) (striped lines represent columnar grains and dots represent equiaxed grains) 39

14. Substrate of the WAAM wall 41

15. Weld bead of WAAM wall 41

16. WAAM wall geometric model 41

17. WAAM wall mesh model with mechanical boundary conditions 42

18. Thermo-physical properties of Inconel 718 [11],[40] 44

19. Temperature dependent properties of Inconel 718 [11] 44

20. Thermo-physical properties of A36 [42] 45

21. Temperature dependent properties of A36 [42] 45

22. Hybrid element activation method used in the thermal model (8^{th} layer) Red elements are dormant elements and blue elements are active ones 48

23. Illustration of thermal boundary conditions 49

24. Gaussian surface heat distribution [45] 50

25. Goldak heat source power distribution[45] 52

26. Thermal histories of different heat distribution models (Goldak, Hemispherical, Ellipsoidal) 57

27. Temperature distributions during the WAAM process a) Layer 1 b) Layer 15 c) Layer 30 . 58

28. Thermocouple results from experiment and simulation (TC1) 59

29. Thermocouple results from experiment and simulation (TC2) 59

30. Thermocouple results from experiment and simulation (TC3) 60

31. Thermocouple results from experiment and simulation (TC4) 60

32. Thermocouple results from experiment and simulation (TC5) 61

33. Hardness profile of the WAAM wall (Results obtained from Clarkson University) 62

34. Microstructure of WAAM part a) Layers 3,4 and 8 b)12,13 and 15 (Done at Clarkson University) 63

35. Microstructure of WAAM part a)16 and 17 b)18 (Done at Clarkson University) 63

36. Microstructure of WAAM part a)19 b)20 (Done at Clarkson University) 64

37. Microstructure of WAAM part a)25 b)30 (Done at Clarkson University) 64

38. Longitudinal stress during the deposition process (layer 11) 65

39. Longitudinal stress distributions during the WAAM process a) Layer 1 b) Layer 15 c) Layer 30..... 66

40. Longitudinal strain: (a) Model without the effect of MS (b) Model with the effect of MS (c) Experimental results (Done at Oak Ridge Lab)..... 68

41. Build direction strain: (a) Model without the effect of MS (b) Model with the effect of MS (c) Experimental results (Done at Oak Ridge Lab)..... 69

42. Stress analysis location in the model 70

43. Longitudinal stress on the mid line of the WAAM wall..... 71

44. Longitudinal stress distribution along the midline of the WAAM wall after 15^{th} and 30^{th} layers 71

45: Temperatures at thermocouple 3 location using different travel speeds 73

46. Longitudinal stress distribution before unclamping (a) 8 mm/s (b) 9 mm/s (Original) (c) 10.8 mm/s..... 74

47. Longitudinal stress distribution after unclamping a) 8 mm/s (b) 9 mm/s (Original) (c) 10.8 mm/s..... 75

48. Build direction stress distribution before unclamping a) 8 mm/s (b) 9 mm/s (Original) (c) 10.8 mm/s..... 76

49. Build direction stress distribution after unclamping a) 8 mm/s (b) 9 mm/s (Original) (c) 10.8 mm/s..... 77

50. Displacement in y direction (in mm) after unclamping a) 8 mm/s (b) 9 mm/s (Original) (c) 10.8 mm/s..... 79

51. Temperatures at thermocouple 3 location using different deposition power..... 81

52. Longitudinal stress distribution before unclamping (a) 1480W (b) 1850W (Original) (c) 2220W 82

53. Longitudinal stress distribution after unclamping (a) 1480W (b) 1850W (Original) (c) 2220W 83

54. Build direction stress distribution before unclamping (a) 1480W (b) 1850W (Original) (c) 2220W 84

55. Build direction stress distribution after unclamping (a) 1480W (b) 1850W (Original) (c) 2220W 85

56. Displacement in y direction (in mm) after unclamping (a) 1480W (b) 1850W (Original) (c) 2220W 87

57. Temperatures at thermocouple 3 location using different dwell times 89

58. Longitudinal stress distribution before unclamping (a) 50 seconds (b) 1 minute (Original) (c) 2 minutes 90

59. Temperature distribution at the end of the deposition of the 30th layer 91

60. Longitudinal stress distribution after unclamping (a) 50 seconds (b) 1 minute (Original) (c) 2 minutes 92

61. Build direction stress distribution before unclamping (a) 50 seconds (b) 1 minute (Original) (c) 2 minutes 93

62. Build direction stress distribution after unclamping (a) 50 seconds (b) 1 minute (Original) (c) 2 minutes 94

63. Displacement in y direction (in mm) after unclamping (a) 50 seconds (b) 1 minute (Original) (c) 2 minutes 96

I. INTRODUCTION

Additive manufacturing (AM) is the process of building a 3D part by depositing one thin layer of material at a time following the digitized geometry from a computer aided design (CAD) file [1]. This method allows for creating complex or customized parts directly from the design without the need for expensive tooling such as casting molds or dyes as well as reducing the number of steps required to produce the final product as some parts can be made in only one step. Also, AM is a very important tool for parts with modern designs which cannot be produced using conventional manufacturing methods like forging and casting. Furthermore, AM technology can be used to reduce the number of parts of a mechanism, as it is capable to assemble multiple components. This method is called part consolidation [1]. AM parts are produced on demand, which significantly reduces the need for storage of spare parts and decreases lead times [1]. In addition, AM has higher material utilization when compared to other modern manufacturing processes such as CNC machining. Because of the recent and significant advancements in AM technology such as in computational hardware and software, higher efficiency and more advanced heat sources, the process shifted from prototyping and modeling into creating high performance and structural parts. Currently, AM is used for various applications such as aerospace, medicine and the automotive industry [1]. AM is also used to produce tools for conventional manufacturing which inherently designed for high production such molds and dyes as well since it requires less time and expense using this process [1].

Categories of metallic AM

While AM can be used with diverse materials, such as metals, polymers and ceramics, this work is only concerned on metal based AM. Metal AM is categorized in multiple ways, either by material deposition technique or by the nature of the heat source. Categorized by material deposition technique, AM can be one of three types as follows:

- *Powder bed fusion (PBF)*: PBF is carried out by creating a bed of powder and directing heat source towards the bed [2]. The generated heat melts the powder, producing a thin solid layer upon solidification. Afterwards, a new layer of powder coating is added to the solidified layer, and the process is repeated until the part is completed. This method produces parts with high dimensional accuracy, intricate features and excellent surface finish. However, this method is inefficient compared with other metal AM methods in terms of material utilization since it produces lots of waste powders. These powders are generally expensive since they have to be produced through specialized gas or water atomization processes with carefully atmosphere-controlled environments. Also, the part size is very limited in size because this method is constrained by the size of the powder bed and vacuum chamber which is used to make a part without inclusions, defects, and oxidation.
- *Direct energy deposition (DED)*: Another widely used metal AM technology is DED. Instead of using a powder bed, the DED process uses a directed flow of powder feed or wire feed along with an energy intensive source such as laser, electric arc or electron beam. DED is a direct-write process where the location of material deposition is determined by movement of the deposition head; this allows large metal structures to be built without the constraints of a powder bed [3]. Powder based DED method has relatively good surface

finish and can create parts with fine features. Nonetheless, the deposition rate is low compared to feed-wire based DED. Moreover, powder based DED needs a chamber for an atmosphere-controlled environment which limits the produced part size. This method is shown in Figure 1 [1].

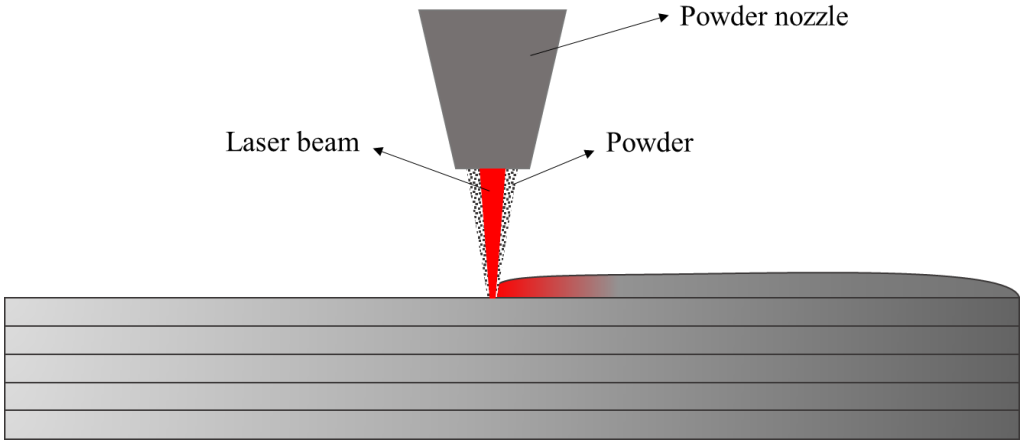

Figure 1. Schematic diagram of laser DED using powder

- *Ultrasonic AM (UAM)*: UAM joins sheets of metal together using ultrasonic vibrations. These vibrations weld the sheets in solid-state at temperatures lower than the melting temperature [4]. This method uses metal foil or laminate instead of powder or wire like in DED process. Nevertheless, this method cannot produce parts with complex geometries without significant machining. UAM has few applications in the industry.

AM of metallic parts can also be classified by the energy source as follows:

- *Laser*: This energy source uses concentrated high energy light to melt the AM material. It is used with PBF or DED method. Two important features of this heat source are high efficiency and high equipment costs [1].
- *Electron beam (EB)*: EB is a flow of high energy electrons produced between a cathode and an anode. This heat source offers higher efficiency, deposition rates, scanning speed,

and larger component production than laser [5]. Nonetheless, this source requires expensive equipment for electron beam as well as a vacuum chamber to avoid oxidation [6]. Additionally, EB only works with conductive powder or wire-feed.

- *Ultrasonic vibrations*: This method uses ultrasonic vibration to join to bind metal layers to produce 3D part [4].
- *Electric arc*: Similar to arc welding, the electric arc is used to deposit material to produce 3D part. Electric arc-based AM is also known as *Wire Arc Additive Manufacturing* and it is the main topic of discussion in this work. More explanation will be provided in the literature review section.

Defects and disadvantages of AM for metals

As all manufacturing methods AM have multiple defects and disadvantages that reduces the produced part quality and performance. Theses disadvantages are shared by all metallic AM methods with varying severity.

- *Loss of alloying element*: loss of alloying element happens in AM because of vaporization alloying elements at the melting pool, influencing the alloy composition thus its mechanical properties. This happens mainly for volatile elements in the material [1].
- *Porosity*: it is one of the most common defects in metallic AM and can largely affect the mechanical properties of the printed part [7]. Porosity happens when high energy density heat sources are utilized. Keyholing, which is basically a vertically elongated welding pool, occurs in such kinds of AM processes [8]. However, the keyholes are not always stable and may collapse, entrapping vapor inside the melt pool which results porosity in the final part. Also, porosity can be the result of trapped vapor produced from inert shielding gas or vaporizing alloying elements.

- *Lack of fusion*: lack of fusion is caused by poor penetration of welding pool into the previous layer[9].
- *Surface roughness*: Surface roughness varies depending on various dependent or independent factors such as the materials used, form of the material (powder or feedstock), process type and parameter, part design, post processing and finishing. In general, powder-based AM have relatively better surface condition than wire-based AM with little to no finishing required [1].
- *Cracking and delamination*: there are two types of cracking: solidification cracking and delamination cracking. Solidification cracking happens when the thermal stresses in the material are excessive. It can be the result of high cooling rates, and liquation cracking which happens in the partially melted zone (PMZ) [10]. When new layer of material is deposited, rapid heating below the liquidus temperature occurs in the PMZ. This causes some of the precipitates in the grain boundaries of the material to melt. During the cooling of the AM part, thermal contraction causes tensile forces in the material and liquid precipitates act like cracking sites in between grains [10]. Delamination is the separation of two consecutive layers in the parts because of the residual stress at the interface of layers. If the magnitude of residual stress exceeds the yield strength, it causes failure in the part [11].
- *Anisotropy*: AM parts have anisotropic mechanical properties because grain growth along the build direction [12]. These parts have columnar grains in the direction of building which are due to the repeated rapid heating and cooling thermal cycling during AM process. The elongated grains lowers the part strength in the building direction compared to the other directions [6].

- *Residual stresses and distortion*: Residual stresses forms in AM parts due to local thermal expansion and contraction. Distortion is a byproduct of the residual stress. More explanation will be provided in a coming chapter of this work.

Wire and Arc Additive Manufacturing (WAAM)

Wire and Arc Additive Manufacturing (WAAM) is a DED process that uses wire-feed as a raw material and electric arc as an energy source. Similar to the electric arc in arc welding process, an electric arc is created between the workpiece and the electrode. The large electric resistance between the electrode and the work piece as well as the high electric current produce sufficient heat for melting the metal wire and depositing it onto the built part [13]. This method works with conductive substrate and electrode only. WAAM process is illustrated in Figure 2.

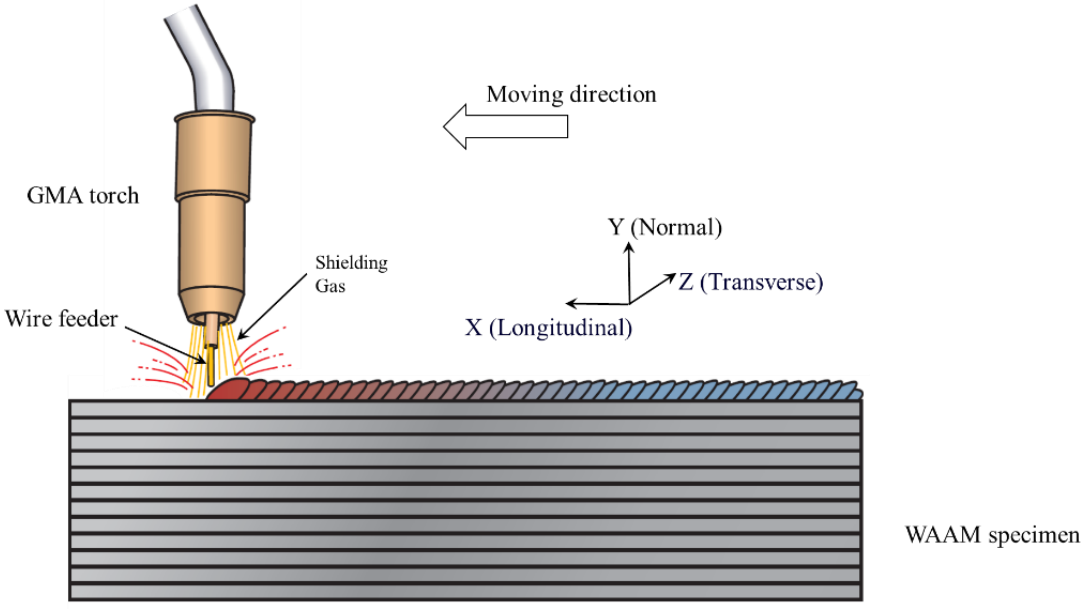

Figure 2. Schematic diagram of WAAM process

WAAM has become an active research topic because of the increasing popularity of this process. High deposition rate and low capital cost of WAAM process makes it a cost effective alternative

for low production number or custom parts compared to PBF and powder-based DED [6]. For example, WAAM can achieve deposition rates up to 10 kg/hr. This rate is far larger than that of powder-based processes with a maximum of 600 g/hr [14]. Additionally, WAAM can produce larger parts compared to EB, AM, or PBF as they require vacuum chamber to reduce defects and oxidation which limits the part size. These additional equipment also increases expense [14]. Also, WAAM feedstock materials are less expensive. And their material utilization, which is represented with the buy-to-fly (BTF) ratio or the amount of raw material used to the amount of material the final part , is higher compared with EB, AM, or PB [6]. Last but not least, WAAM uses an electric arc as its heat source which can be utilized in ambient atmosphere and out-of-chamber environment. These features offer WAAM to save significant expense, especially for expensive materials like titanium [14].

However, WAAM has some disadvantages that may hinder its adaptation. The major disadvantage is residual stress (RS) which is a product of local heating and cooling thermal cycles. Great heating and cooling rates at different location of the part is caused by high thermal gradient around the heat source [12]. These factors cause nonuniform expansions and contractions throughout the part. RS remain in the part even after the heat source is removed and it is cooled down. RS have detrimental effects on WAAM part such is distortion, delamination, lower fatigue life, and lower mechanical strength. Another drawback is resultant microstructure. WAAM parts contain large columnar grains, causing lower strength and toughness compared to forging process [6]. These grains are produced because of low energy density of the arc in WAAM, which has low thermal gradient comparison with laser and electron beam heat sources [6]. Higher thermal gradients produce finer grains. WAAM also requires more machining compared to powder-based process because of its higher surface roughness and layer thickness [14].

Literature review

History of WAAM

The idea of using arc and feedstock to additively manufacture components is not a recently conceived idea. The first patent with regard to this method was put on record in 1925 [15]. The production method of a pressure vessel using WAAM was patented in 1971 [16]. Serious research about this method started in the beginning of the 1990s [17]. Continuous advancements in computer technology, control systems and robotics in the past 30 years greatly improved WAAM process [14]. Currently, investigation of WAAM process includes the quality and surface finish of the component, microstructure, distortion, residual stress, strength, and ductility in the part.

Types of WAAM processes

- *Gas metal arc welding (GMAW)*: GMAW is considered a very flexible WAAM method, since the wire is the consumable electrode which eliminates the need. Also, higher deposition rates are achievable using this welding method compared with GTAW and PAW [18]. However, this method is susceptible to splatter and arc instability, which produces lower quality parts. Some techniques can be used to alleviate these shortcomings. [19] demonstrated the effect of implementing cold metal transfer (CMT), which is a technique that is based on shot-circuiting arc by dipping the arc wire into the welding pool resulting in high deposition rate and low input heat [20], in GMAW AM of aluminum. CMT was used with other techniques such as pulsing the welding current. Using these techniques resulted in parts with less porosity, more equiaxed grains, oxidation clear welds and less splatter. Also, [21] concluded that CMT for hot work tool steel eliminates welding cracks, create a product with homogeneous hardness profile, and produces welds with more

equal layer width which improves the quality of the part. Nevertheless, CMT is not suitable for titanium alloy welding because of the presence of arc wandering which produces rough weld surfaces [12].

- *Gas tungsten arc welding (GTAW)*: GTAW uses a tungsten wire as an electrode and another wire as the material source. GTAW is used extensively in WAAM, especially for titanium and aluminum welding. The advantages of GTAW include smooth layer appearance, oxidation cleaning of the cathode and arc stability compared to GMAW [22]. GTAW has an additional challenge next to their GMAW counterpart, because of their reliance on an external wire feed that has to be in fixed position and angle relative to the electrode [12].
- *Plasma arc welding (PAW)*: Similar to GTAW, PAW uses a non-consumable electrode like in Figure 3. PAW has higher energy concentration, improved arc stability and lower amount of inclusions compared to GTAW, which allows for higher travel speeds and part quality [23]. Also, pulsed PAW technique (PPAW) is used to provide lower heat input and higher tensile strength but at the cost of lower elongation [24]. However, PAW is more expensive than GTAW and GMAW due to capital cost involved in this process. PAW also needs an external feed-wire moving relative to the electrode.

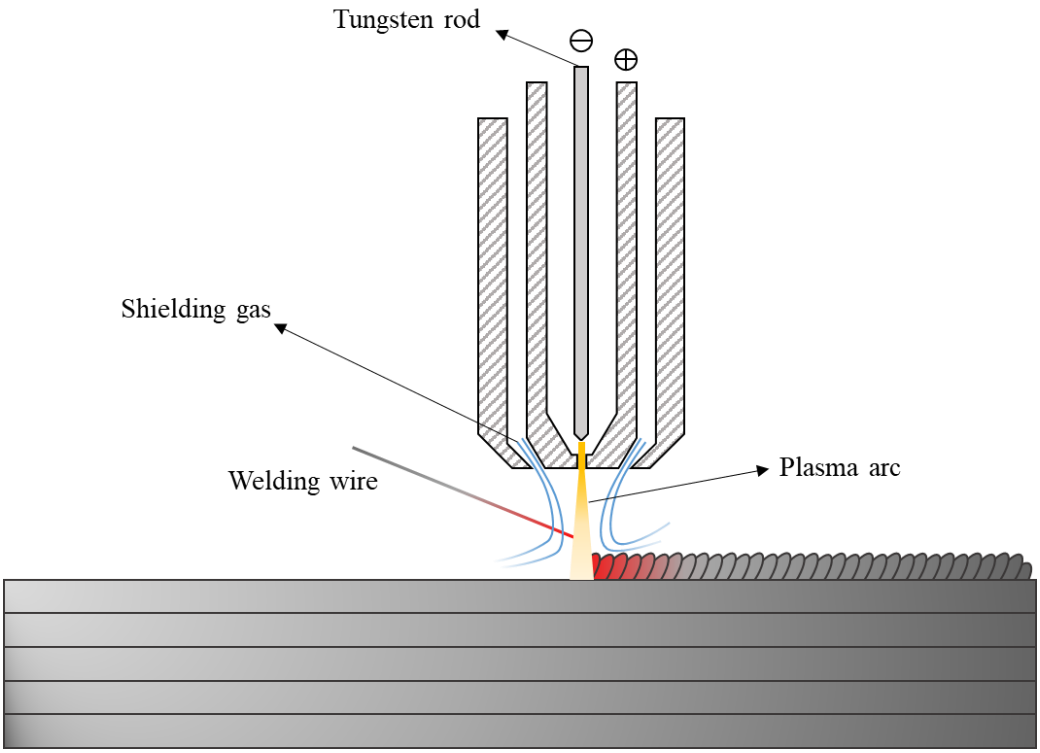

Figure 3. Diagram of AM process using PAW

Materials used with WAAM

Materials vary widely in WAAM even when using the same process. In this section the most used materials will be discussed, showing their strengths and weaknesses.

- *Titanium alloys*: Titanium alloys are mostly used in aerospace and biomedical applications, due to its high strength, toughness, corrosion resistance [25] and high strength-to-weight ratio [18]. Additionally, AM titanium alloys have higher damage tolerance properties and fatigue life compared to its wrought counterpart [12]. It is very compelling to use titanium in WAAM instead of conventional subtractive manufacturing because of its high cost. However, titanium in WAAM suffers from anisotropy because it produces columnar grains due to its solidification characteristics. The use of inoculants refines the microstructure of titanium in WAAM [25].

- *Nickel-based super alloys (Inconel)*: This material is very popular in WAAM because of its high strength at high temperatures and its oxidation resistance in addition of being difficult to machine and having a high cost of fabrication using traditional manufacturing methods [25], [18]. Nickel-based alloys are used in aerospace, chemical, and nuclear applications because of its high strength and chemical resistance. Nevertheless, these alloys are susceptible to solidification and liquation cracking, and its high concentration of alloying elements result in segregation of those elements during the process [25]. Also, parts made from these alloys using WAAM have long columnar vertical grains and does not have homogenous hardness along the build direction of the part. Properties of parts made from Inconel using WAAM have slightly lower mechanical properties than those in wrought conditions [25].
- *Aluminum alloys*: The use of aluminum in WAAM is researched extensively and it was concluded that using it in WAAM is not viable most of the time, mainly because the parts produced are inferior to machine aluminum parts as well as the relatively insignificant cost saving compared to machining since aluminum is not expensive [18]. Also, aluminum has oxidation and solidification behavior problems in addition to porosity, that reduces the quality of the parts [25]. Alumina has a higher melting point than aluminum which can be trapped in the welding pool causing defects and pores. Nonetheless, porosity problems can be mitigated though CMT welding [14]. Furthermore, the turbulent welding pool dynamics result in poor dimensional accuracy. Aluminum has high thermal conductivity, thermal expansion, wide solidification range and high solubility to hydrogen [25]. Some of the drawback of aluminum can be mitigated by heat treatment. However, not all aluminum alloys are heat treatable [25].

- *Steel alloys*: Generally, because of the low cost of steel, only large parts with complex geometry are viable to manufacture using WAAM. Stainless steels are used in WAAM for chemical and nuclear application due to their corrosion resistance. High carbon steels are found to experience cold cracking, hydrogen entrapment, and RS. These problems were mitigated by using pre-heating techniques [25].

Previous work

The RS in the WAAM process was examined with various heat sources. Ding et al. 2011 [26] studied the GMA-WAAM process using mild steel. The work included experimental and FE analysis. However, it did not include parametric or microstructural analyses. Colegrove et al. 2013 [27] and Hoye et al. 2013 [28] have studied the GMA-WAAM using structural steel and GTAW-WAAM using Titanium (Ti-6Al-4V) experimentally, respectively. They included the RS and microstructure analyses with minimal work concerning process parameters. Zhang et al. 2015 [29] studied the fatigue crack propagation in PA-WAAM numerically and experimentally without providing analysis of the effect of parameters on the fatigue life. Cao et al. 2016 [5] established an experimentally verified numerical model of an EB-WAAM wall for the purpose of process optimization. However, the sample walls used only have 6 and 11 layers and the model was not utilized for studying the effects of large parts.

Even though WAAM has become an active topic of research, the thermal, mechanical, and microstructural characteristics of this method have not been investigated thoroughly, particularly in larger parts. Additionally, the effect of the process parameters on the RS have not been studied extensively due to the complex physical interaction involved in the AM process.

This study focuses on studying the effects of the WAAM process parameters on the RS in a large WAAM wall. The wall was made using GMA-WAAM method at Clarkson University. The

substrate temperatures were measured during the process and the micro strains were measured non-destructively after building using Neutron Diffraction method at Oak Ridge National Laboratories. The microhardness and microstructure of the wall were also investigated along the build direction. The wall was modeled numerically and verified using the experimental data. Different process parameters were changed in the numerical model to evaluate their effects on the RS and distortion of the part.

The second chapter of this work explains the experimental process, methodologies measurement techniques. The third chapter discusses the numerical modeling process and its mathematical representation. The fourth chapter compares the experimental data with the numerical results. The effect of process parameters on the thermal profile, RS and distortion will be displayed in this chapter. Finally, the fifth chapter summaries the outcome of this work and provides several possible future works.

II. EXPERIMENTAL SETUP

In collaboration with students at Clarkson University, the experiment was conducted by fixing a A36 steel substrate, that is 304.8 mm long, 101.6 mm wide and 6.35 mm thick, with a screw on each side. Five thermocouples are then attached to the substrate. The thermocouples are equally spaced by 2.5 cm and they are all 1 cm away from the wall. Figure 4 shows the dimensions of the part as well as the locations of the thermocouples on the substrate. Moving the thermocouples any closer to the wall might cause them to malfunction during the welding process.

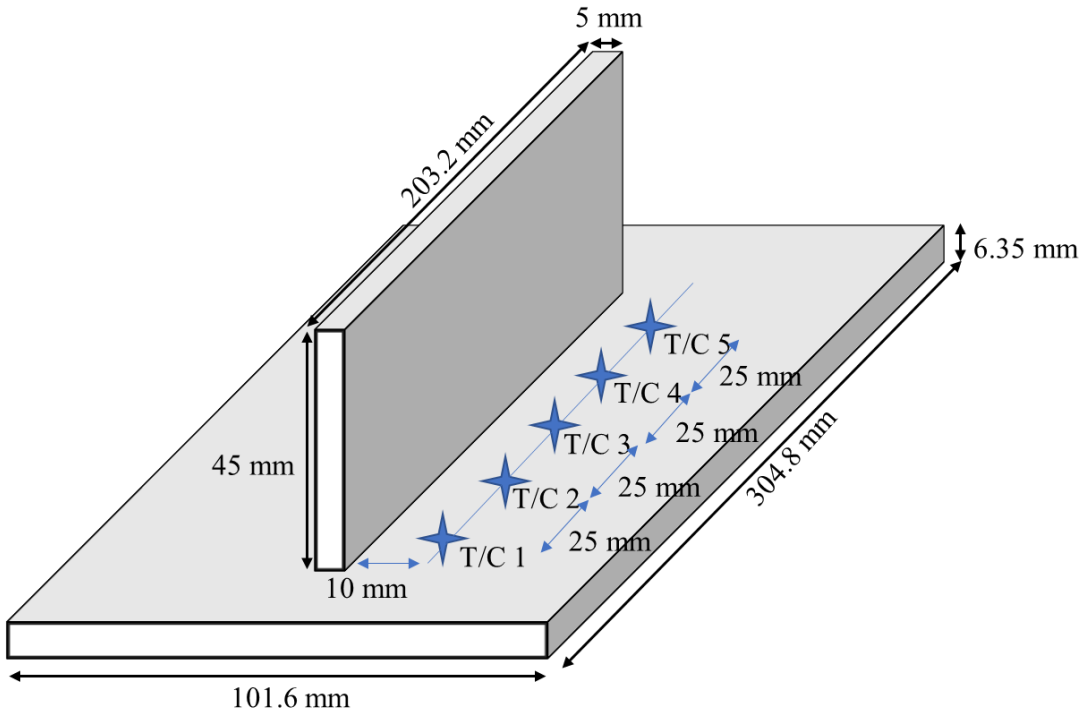

Figure 4. Detailed dimensioning of the WAAM wall and the location of thermocouples on the substrate

The printing process was done using a semi-automatic GMAW system with a 0.9 mm diameter Inconel 718 solid filler wire for depositing the material and pure Argon as shielding gas. The wall was centered in the middle of the substrate. Thirty layers were deposited to produce the WAAM

wall. Each layer of the wall was 1.5 mm high, 5 mm wide, and 203.2 mm long, on average. The deposition speed was 9 mm/s with a 60s dwell time between the deposition of each layer. The welding direction is alternated for every layer for optimal heat distribution as shown in Figure 5. 1850 W of power was supplied to melt the welding wire for the first 10 layers of the build. After that, the welding power was reduced to 1000 W because the electrode would stick to the bead while welding with high power. After completion, the part was left to cool completely and then it was unclamped. Figures 6 and 7 show the built wall with the thermocouples attached and dimensioning provided. Table 1 shows the process parameters used by the GMAW machine.

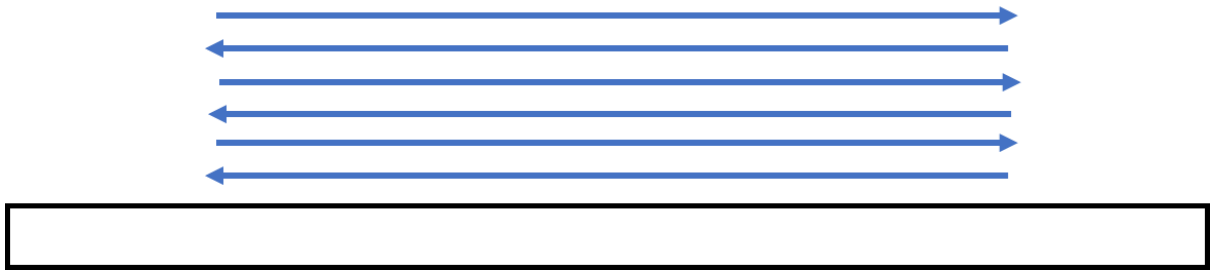

Figure 5. Illustration of welding direction for WAAM wall

Figure 6. The AM part after completion with thermocouples attached
(Done at Clarkson University)

Figure 7. The final AM part in scale
(Done at Clarkson University)

Table 1. WAAM process parameters

Parameter	Value
Voltage	22 V
Current	140 A
Travel speed	9 mm/s
Wire diameter	0.9 mm
Wire-feed speed	150 mm/s
Dwell time	60 s

For microstructural evaluation, the cross section of the wall was sectioned. The samples were ground using abrasive papers and polished using 3 and 1µm diamond suspensions. Afterward, they were etched using "6 ml HNO3 + 6 ml HCl + 3 ml glycerol" to reveal the microstructure. The microstructure was observed using an optical microscope.

The Hardness was also measured along the build direction using Vickers hardness test with a diamond head. The indentations were distanced by 0.5 mm from each other. Figure 8 show the indentations on the produced AM part.

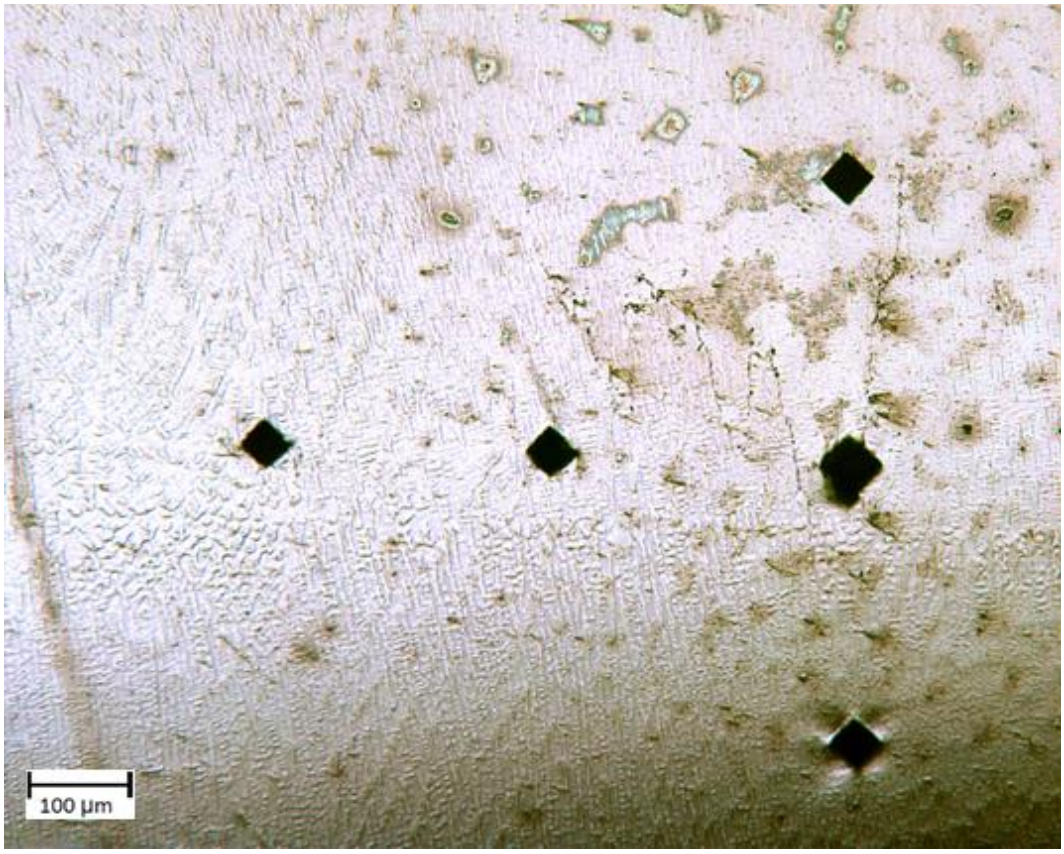

Figure 8. Vickers hardness test indentations on the sample
(Done at Clarkson University)

Neutron diffraction (ND) measurement

Neutron diffraction (ND) is powerful tool to determine residual stresses within a large thickness of an engineering material due to its high penetration power. Additionally, ND can provide three-dimensional mapping and volume-averaged bulk measurements. In this study, the lattice spacing between the atoms in the WAAM part was examined using ND method at the Oak Ridge National Laboratory's High Flux Isotope Reactor (HFIR). The lattice spacing measurements were done in

the X, Y directions, as shown in Figure 9. Measurement through the thickness of WAAM part was not measured since the specimen was thin. The lattice spacing measurements in X and Y are converted into microstrain data according to the following equation [30]:

$$\varepsilon_{ii} = \frac{d - d_o}{d_o} = -cot\theta(\theta - \theta_o) \quad i = 1,2,3 \qquad (1)$$

where the d and d_o are the interplanar spacing under the stressed and stress-free state, respectively. And θ and θ_o are the diffraction angles for the stressed and stress-free specimens at each location, respectively [30].

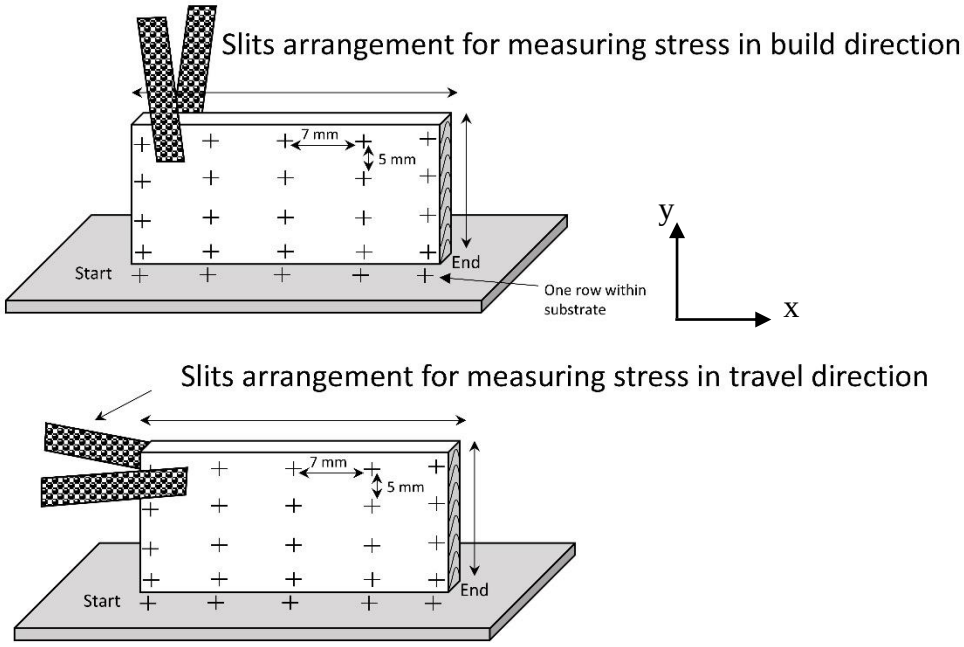

Figure 9. Measurement setup using ND in different directions

III. NUMERICAL MODELING

Many physical phenomena occur during WAAM process. It is crucial to define and analyze these phenomena to predict their effects on AM. Heat transfer processes, fluid flow in the welding pool, microstructure evolution, plastic deformation and thermal stresses are some of those physical processes that happen in WAAM. This chapter will provide some background about those processes as well as mathematical representation of them and numerical techniques used to solve the mathematical models.

Mechanics and mathematical model

The introduction of a concentrated heat source to the welded parts produces multiple effects. The high thermal gradient and uneven cooling cause thermal expansion and contraction at different rates and magnitudes throughout these parts. These factors create residual stress (RS) and distortion within the component [31]. Additionally, small grains and segregation of material components are results of a high cooling rate at some regions of the part and slow cooling at other regions, respectively [6]. Other phenomena like hydrogen embrittlement occur during the welding process [32]. These phenomena affect each other in a reciprocal manner [33], which is illustrated in Figure 10. These effects are not symmetric in both directions. This information is important since it helps decoupling the governing equations simplifying the model without sacrificing accuracy.

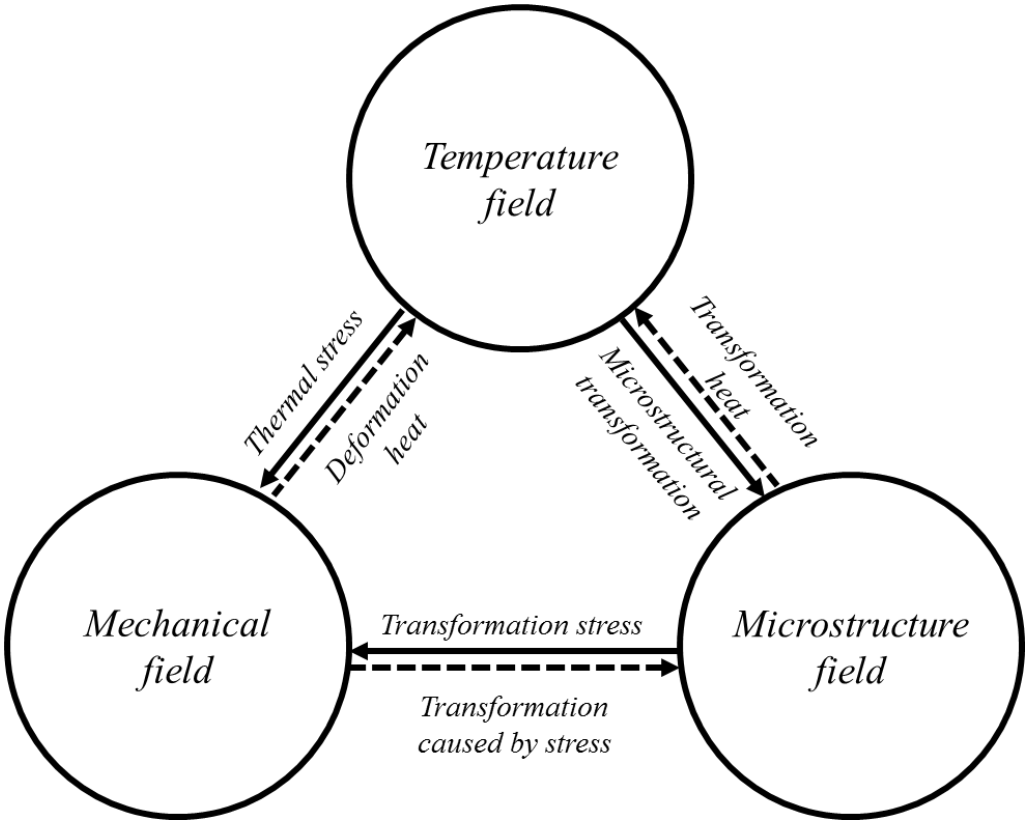

Figure 10. Relation between different fields in the welding process
The solid lines represent a strong relation and the dashed lines represent a weak relation

The model must abide to the conservation laws of mass (*2*), momentum (*3*) and energy (*4*), which are the base points for modeling the system mathematically.

$$\frac{D\rho}{Dt} + \rho \frac{\partial v_i}{\partial x_i} = 0 \tag{2}$$

$$\rho \frac{Dv_i}{Dt} = \frac{\partial \sigma_{ji}}{\partial x_j} + \rho f_i \tag{3}$$

$$\rho \frac{Dh}{Dt} = -\frac{\partial q_j}{\partial x_j} + q''' + \sigma_{ji} \frac{\partial v_i}{\partial x_j} \tag{4}$$

Where ρ is density, v is particle velocity, σ is the stress tensor, f is the body force, h is enthalpy, q is heat flux and q''' is heat generation in the material [34]. The system must always follow these laws.

Thermal model

The thermal process in WAAM is the driving force of all mechanical effects such as thermal stresses, and microstructural effects like the shape and size of the grains, in the built part. For this reason, the thermal profile must be modeled accurately to predict the stress and microstructure in the WAAM part.

Employing the energy conservation of the thermal model with ignoring mechanical effects, equation (*4*) can be written as:

$$\rho C_p \frac{\partial T}{\partial t} = -\frac{\partial q_i}{\partial x_i} + q''' \tag{5}$$

where $q'''$is the input/output heat per unit volume, T is the temperature, ρ is the density, C_p is the specific heat and q_i is the heat conduction rate vector.

The $\frac{\partial q_i}{\partial x_i}$ represents the heat flux in the system. The heat flux inside the material is done through conduction modeled with Fourier's law:

$$q_{i_{conduction}} = -k \frac{\partial T}{\partial x_i} \tag{6}$$

where k is the thermal conductivity of the material.

Additionally, heat flux happens at the boundaries of the system through convection (*7*) and surface radiation (*8*).

$$q_{i_{convection}} = h_i(T - T_\infty) \tag{7}$$

$$q_{i_{radiation}} = \varepsilon_i \sigma (T^4 - T_{surr}^4) \tag{8}$$

Where T_∞ is the average temperature of the surrounding air and T_{surr} is the temperature of the surrounding environment, far away from the part. (T_{surr} must be in K not C). Convection and radiation are considered surface conditions in the system. Some heat source models, such as the Gaussian heat flux model, are classified as surface energy sources that fall under the heat flux category in the system.

q''' is the volumetric heat generation in the system, which accounts for volumetric radiation (not applicable for opaque materials) and volumetric heat sources like the Goldak model. The classification of heat sources for WAAM will be discussed in the numerical modeling section.

Mechanical model

The mechanical model is considered to be in quasi-static equilibrium. This can be represented by employing the momentum equation (*3*):

$$\frac{\partial \sigma_{ji}}{\partial x_j} = 0 \tag{9}$$

RS are internal forces in a mechanical part without any external loads exerted on it [33]. There are multiple orders of RS that exist inside the material. First order stresses that happen on the macroscale, which are in interest in this work. Second order stresses form between the grains at the grain boundaries on the microscale. Third order stresses form interatomically in the nanoscale [35].

WAAM parts suffer from severe distortion if carried out without clamping. On the other hand, increasing the fixation of the part during building reduces the distortion significantly but increases the RS and can lead to cracking and part failure. The relationship between clamping and RS is shown in Figure 11.

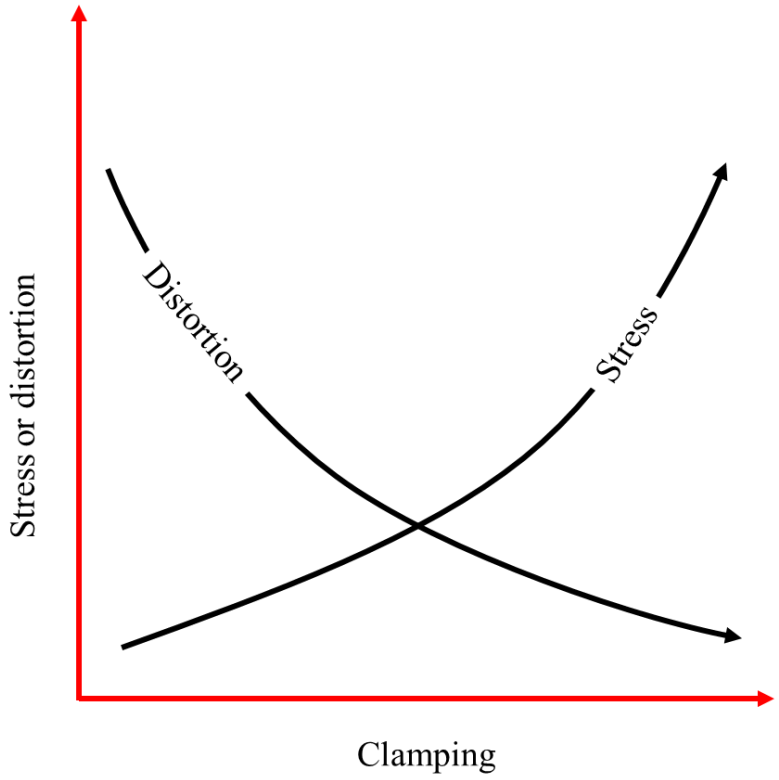

Figure 11. The relationship between the clamping and residual stresses

These stresses in WAAM parts are a direct result of the heating and cooling during the material addition process. Uneven temperature distribution and heating/cooling rates will cause thermal expansion and contractions with different magnitudes across the part [31]. This uneven distribution due to the localized heating of the welded part causes volumetric changes near the heat source. On the other hand, regions far away from the heat sources will restrain the volume changes. If the temperature is high enough, subsequently the increase in volume is large enough, plastic deformation will occur. After the cooling process the material will contract leaving some residual stress in the part. In some cases, the material will contract greatly such that it causes yielding during the cooling process. In such case the residual stress will be equal to the yielding strength of the material in some regions of the part [36]. During the welding process in WAAM, compression

stresses are formed in front of the heat source because of the expansion due to heat, while tensional stresses are induced behind the heat source because of contraction. The thermal expansion is modeled using equation (*10*).

$$\varepsilon^{(T)} = \alpha \Delta T \tag{10}$$

$\varepsilon^{(T)}$ is the dilatoric thermal strain, α is the thermal expansion coefficient and ΔT is the temperature difference from a reference temperature.

By employing Hooke's law, the thermal stress can be calculated using the following relation:

$$\sigma_T = -\frac{\alpha \Delta T E}{1 - 2\nu} \tag{11}$$

Here ε_T is the thermal strain, σ_T is the suppressive triaxial thermal stress, α is the thermal expansion coefficient and ΔT is the temperature difference from a reference temperature [33].

The material suffering from thermal stresses can be modeled as a rod connected to spring as shown in Figure 12. When the rod expands with temperatures, force will be exerted on it from the spring. If the maximum temperature is below T1, there will be no RS. If the maximum temperature is between T1 and T2, RS will be generated but it will be below the yield strength and no plastic deformation will occur. However, if the maximum temperature is higher than T2, RS will reach yield strength and plastic deformation will occur [36].

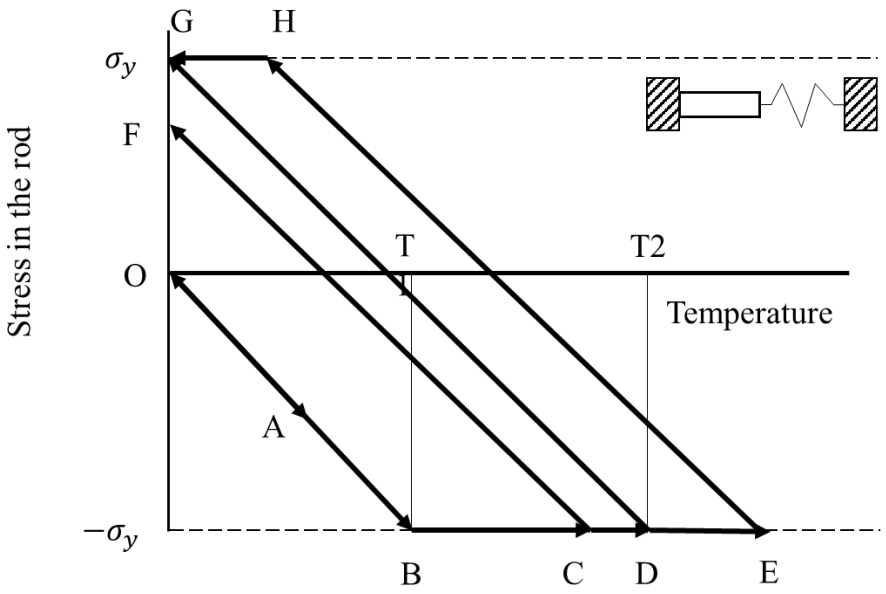

Figure 12. Rod-spring model illustrating the residual stress inside the material

Microstructural model

Mechanical properties are significantly influenced by the grain structure of the AM part. The microstructure is mostly dependent on temperature profile of the AM process. The thermal gradient and the solidification rate are the two factors affecting the size and shape of the grains [37]. The following equation defines the relation between the two factors [38]:

$$R = \frac{1}{G}\frac{\partial T}{\partial t} = \frac{1}{|\nabla T|}\frac{\partial T}{\partial t} = \frac{1}{\sqrt{\left(\frac{\partial T}{\partial \xi}\right)^2 + \left(\frac{\partial T}{\partial z}\right)^2 + \left(\frac{\partial T}{\partial y}\right)^2}}\frac{\partial T}{\partial t} \quad (12)$$

Where R is the solidification or growth rate, G is the thermal gradient, T is the temperature, t is the time, ξ is the coordinate where motion occurs.

$$\xi = z + v(\tau - t) \quad (13)$$

v is the welding speed, τ is the total time and t is the current time.

Although the microstructure depends on the thermal gradient and solidification velocity, the direction of the grain growth is along the maximum heat flux direction. The maximum heat flux is always perpendicular to the trailing edge of the molten pool towards the substrate. Thus, the columnar grains grow in the direction of the maximum heat flux perpendicular to the trailing edge of the pool [37]. This is shown in Figure 13.

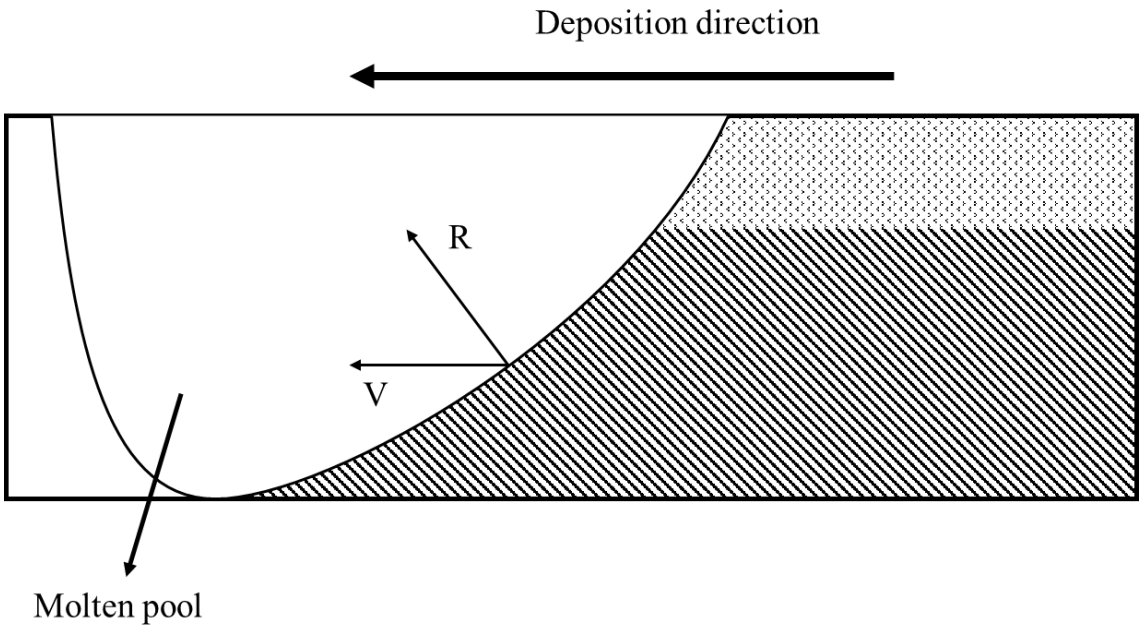

Figure 13. An illustration that shows the direction of the grain growth (R), solidification velocity (V)
(striped lines represent columnar grains and dots represent equiaxed grains)

Numerical model

The differential equations used to model the thermal and mechanical systems, described in Mechanics and mathematical model, are difficult or in this case even impossible to solve using analytical methods. Numerical methods must be used such as finite element method (FEM) to devise an approximate solution. This section will discuss the assumption, geometrical modeling, material properties, FE techniques, boundary conditions, and the meshing process.

Because of the decoupled nature of the thermal and mechanical fields, the numerical analysis of the thermal field can be done independently from the mechanical analysis. The results of the thermal analysis are used as input for the mechanical analysis. The simulation is done using ABAQUS software.

Thermal analysis

Geometrical modeling and meshing

Geometrical modeling is the first step of the FEM. The model comprises of two main parts. The substrate and the welding beads.

As for the substrate, it is modeled as shown in Figure 14, with 304.8 mm of length, 101.6 mm of width and 6.35 mm thickness.

For the weld bead in Figure 15, the length is 203.2 mm, the width is 5 mm and the thickness is 1.5 mm. The bead is assumed to be rectangular. This approximation in the geometry had to be assumed to reduce complexity of the model, simulation time, the number of simulation errors, and avoid improper element shapes.

Finally, the parts are assembled to form the WAAM wall like in Figure 16. The base plate and weld bead are added to the assembly. Then, the bead is centered in the middle of the top surface of the plate. Lastly, the bead was patterned into 30 instances, which is the number of layers in the wall. The base plate and the 30 beads are constrained together using a tie constraint. A tie constraint ties two separate surfaces together so that there is no relative motion between them. This type of constraint allows the fusion of two regions even though the meshes created on the surfaces of these regions may be dissimilar [39]. The part was allowed to cool for 2000s after it was finished.

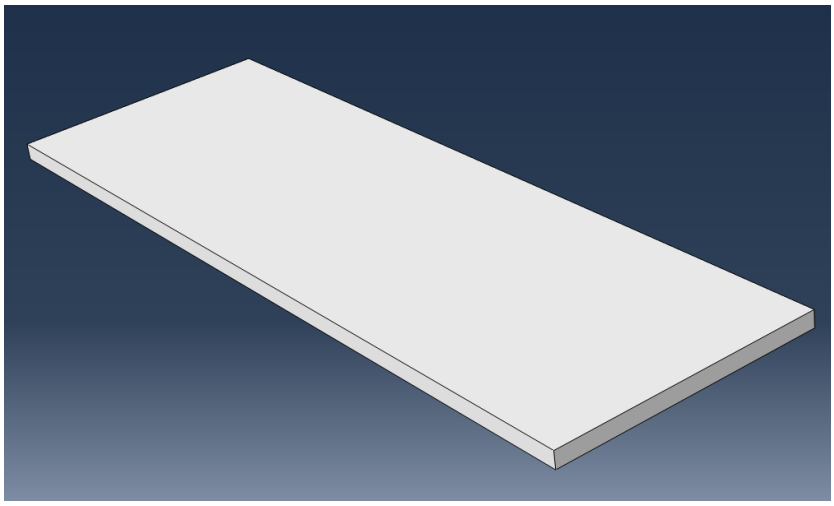

Figure 14. Substrate of the WAAM wall

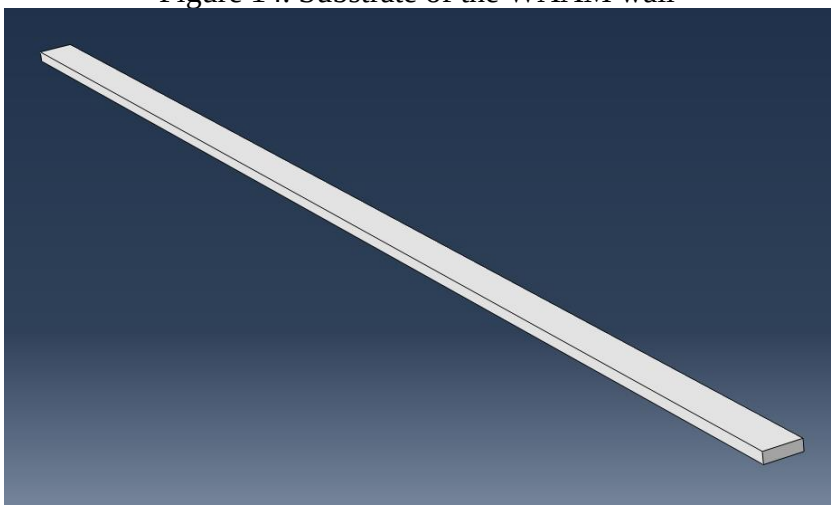

Figure 15. Weld bead of WAAM wall

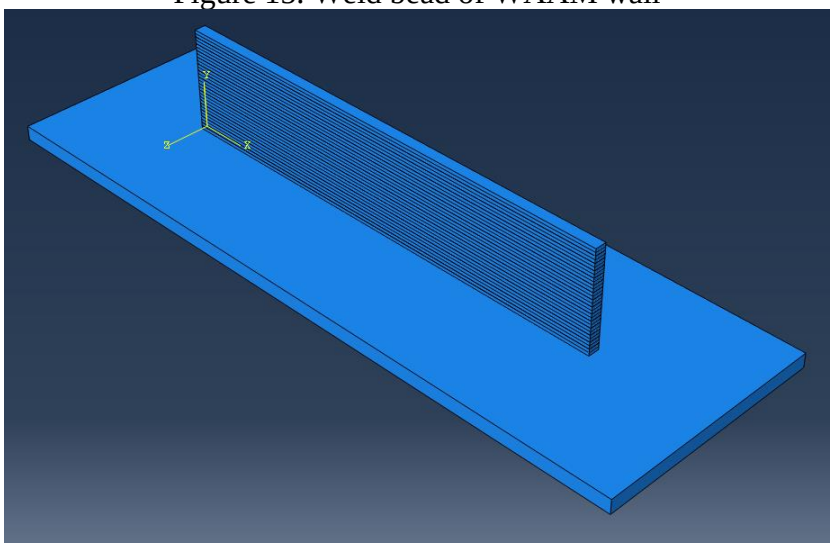

Figure 16. WAAM wall geometric model

The meshing process was done using local and global seeding of the different geometrical parts of the model. The welding bead that constitutes the WAAM wall was meshed with 1.5 mm long brick elements. Each bead had one layer of elements. In most welding literature, element sizes at the welding zone is about 0.5 mm. However, this standard is used for single pass welds, multipass welds with less than 5 passes or with small AM parts. In this case, the AM part is significantly larger and using smaller element size will require at least 27 times the computational power and CPU time to finish the simulation, which is unattainable in this work.

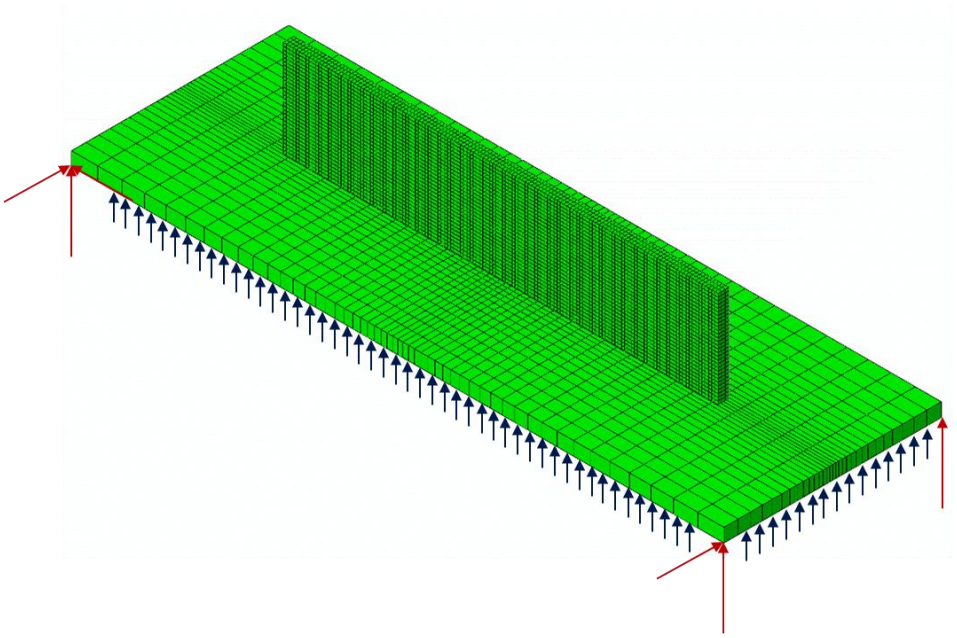

Figure 17. WAAM wall mesh model with mechanical boundary conditions

For the substrate, local meshing was introduced for a more efficient element distribution. Mesh should be finer and denser in areas closer to the welding torch to provide the maximum accuracy with the least number of elements utilized. The base plate has 50 elements in the x direction and 30 elements in the z direction. Both directions have a double bias value of 5 towards the middle. The bias value specifies the nonuniform distribution of elements along an edge and it is the ratio of the largest element to the smallest element [39]. In the y direction, one layer of elements is

considered enough to mesh the part. Figure 17 shows the meshed model geometry. The number of elements in the weld bead is 405. The number of elements in the substrate is 1500. The total number of elements in the model is 13650. The element type used is the DC3D8 heat transfer linear brick element.

Material properties

As mentioned before, the WAAM wall was built on A36 steel and was made from Inconel 718. Using accurate material properties is essential for accurate results. Figures 18, 19 and Table 2 show the thermal and mechanical properties of Inconel 718. Figures 20, 21 and Table 3 show the thermal and mechanical properties of A36 steel.

Table 2. Thermo-physical properties of Inconel 718 [11],[40]

Properties	Values
Liquidus temperature (K)	1609
Solidus temperature (K)	1533
Latent heat of fusion (J/kg)	210000
Density (kg/m^3)	8100

Table 3. Thermo-physical properties of A36 [41]

Properties	Values
Liquidus temperature (K)	1727
Solidus temperature (K)	1627
Latent heat of fusion (J/kg)	245000
Density (kg/m^3)	7500

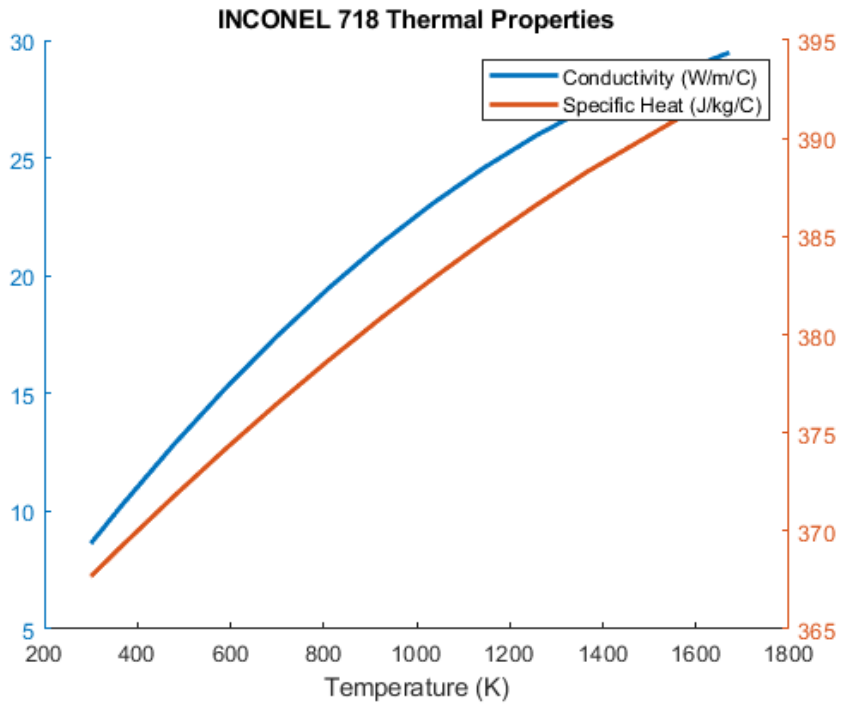

Figure 18. Thermo-physical properties of Inconel 718 [11],[40]

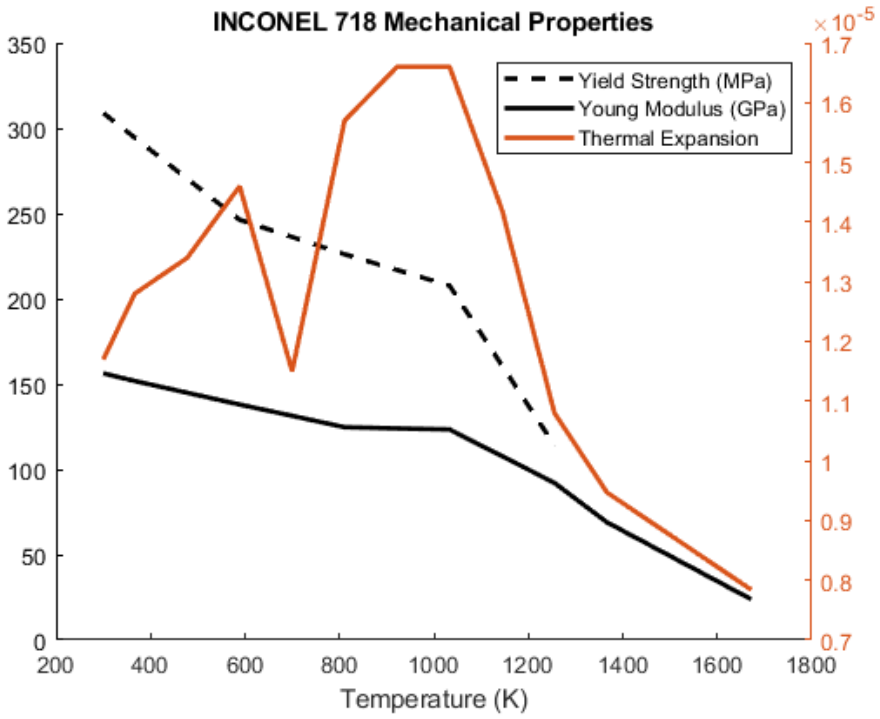

Figure 19. Temperature dependent properties of Inconel 718 [11]

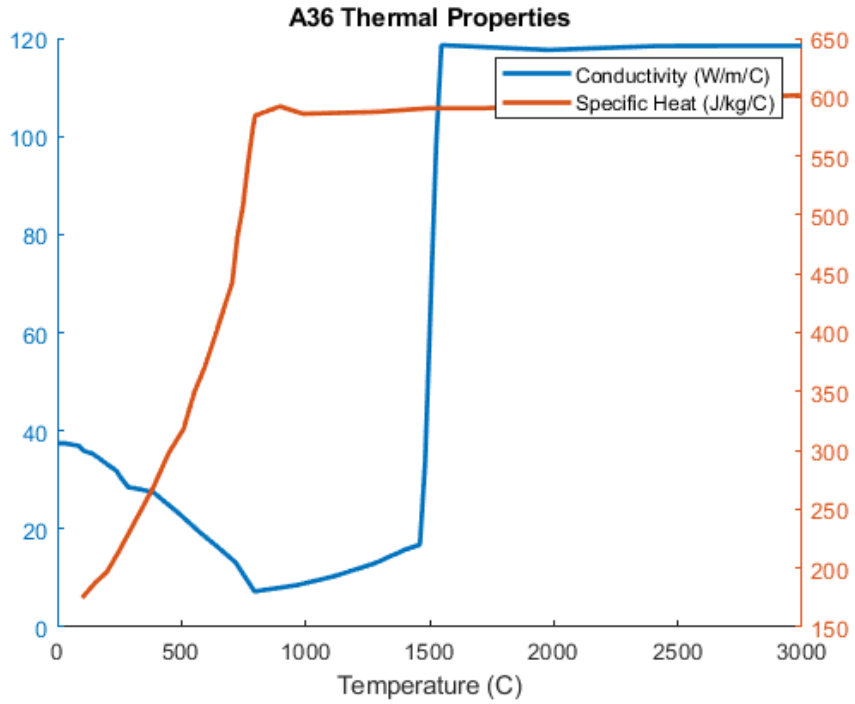

Figure 20. Thermo-physical properties of A36 [42]

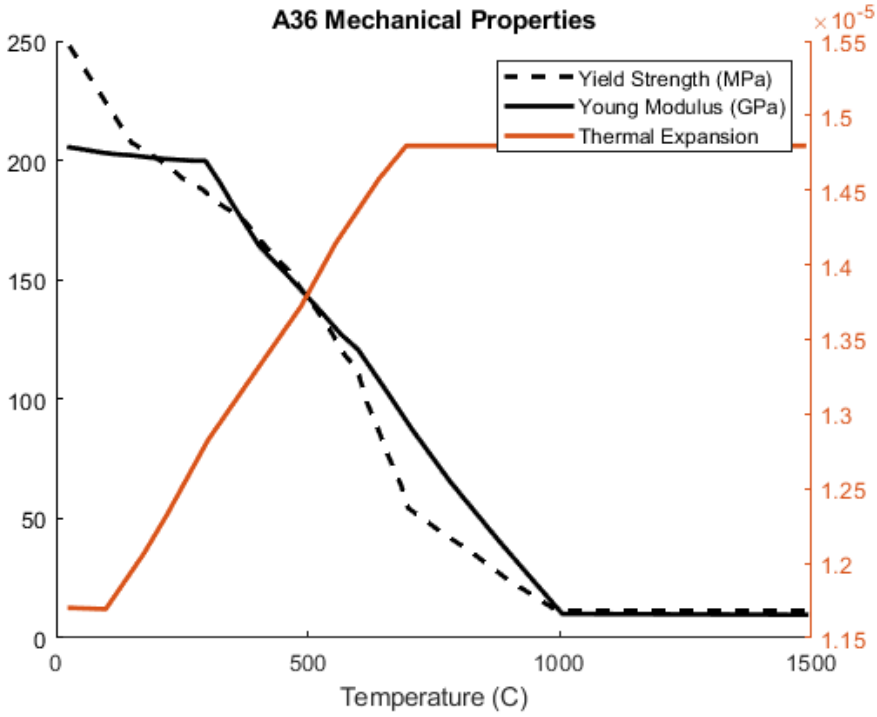

Figure 21. Temperature dependent properties of A36 [42]

The properties are assigned to their corresponding parts, Inconel 718 for the wall and A36 for the substrate.

Element activation

To simulate the AM process some technique must be utilized to add material to during the deposition process. There are multiple techniques used for the material addition process [43], including:

- Quiet element method: In the quiet element method, inactive elements exist in the model by they are given a dormant state. In this dormant state, the elements have fictious properties that make the effect of those elements insignificant to the analysis. When the element is activated, the proper properties are given to the elements which make them effective in the analysis. For thermal analysis, the conductivity and specific heat are reduced to make the element dormant. The conductivity and specific heat are reduced ideally by six and two orders of magnitude, respectively.

  This method has the following advantages:

  - Can be easily implemented using commercial software and subroutines
  - The number of equations in the model are constant because the number of elements does not change, which reduces analysis time since there is no need to renumber the equations when new elements are added

  However, this method has multiple disadvantages, such as:

  - If the fictious properties are not small enough, the elements will not fully dormant which will result in errors in the analysis
  - If the properties are too small however, the Jacobian in the analysis will be ill conditioned and will result in convergence errors

- When this method is used in an analysis where most of the elements are dormant, longer computational time will be required when compared with the inactive element method.

- Inactive element method: In the inactive element method, inactive elements representing the deposited material are removed from the model. When the material is deposited, the material's elements are born in the model.

  The advantages of this method are:

  - No errors related to ill-conditioned Jacobians can occur
  - Analysis is performed for active elements only, which makes the algebraic systems representing the elements smaller

  The disadvantages of this method are:

  - This method can be utilized using commercial software subroutines and can only be done using custom code
  - The equation numbering must be done each time a new element is born in the model, which can negate the computational advantage of analysis of lower number of active elements
  - Born elements might not have the initial temperature of the model which results in undesired energy addition to the model, which might cause errors

- Hybrid method: The hybrid method combines the inactive and quiet element methods to get the advantages of both. In hybrid method, the elements of every layer of AM are born at the same time but in dormant state. Those elements become active when the material is deposited. In Figure 22, the hybrid method is utilized for material addition. As seen from the figure, the eighth layer is being deposited. All later layers are inactive elements that

will be born when they start being deposited. In the same eighth layer, added material elements are in the active state and they are being shown in blue, and the other elements that are yet to be added are in the dormant state represented in red. The hybrid method is implemented using a combination of model change interaction and USDFLD Abaqus subroutine which will be explained in the subroutine section. Model change interaction in Abaqus allows for removal and reactivation of elements during an analysis [39], and it was used to activate layers at their corresponding steps.

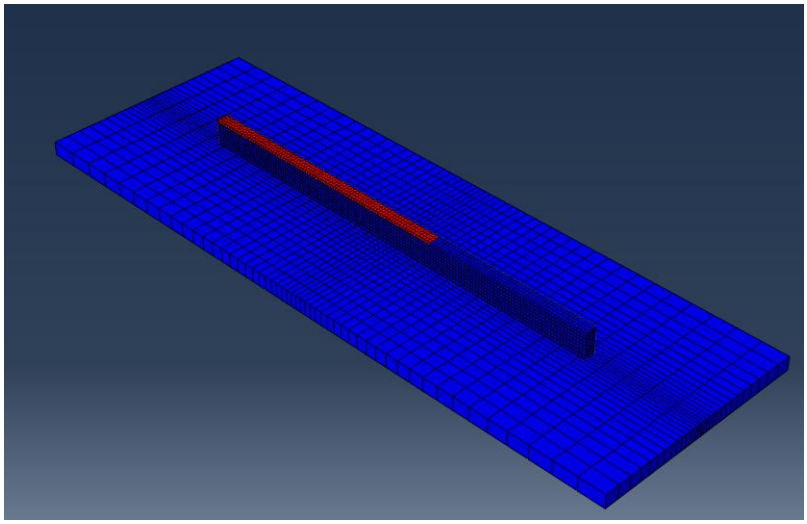

Figure 22. Hybrid element activation method used in the thermal model (8^{th} layer)
Red elements are dormant elements and blue elements are active ones

Assumptions and boundary conditions

There are multiple assumptions and boundary conditions imposed on the model in order to reduce its complexity and avoid convergence issues. Some of the assumptions and boundary conditions in the thermal model are:

- The system was modeled as a solid without accounting for the fluid flow in the weld pool.

- For each layer, the entire layer is activated with quiet properties and given lower conductivity and specific heat values. This improves the performance of the simulation and simplifies the modeling process.
- Radiation boundary heat transfer is neglected. Instead, a combined radiation and convection film coefficient is adapted to the model.
- The shielding gas causes forced convection near the welding area. The forced convection is modeled as a sphere of high convection coefficient moving with the heat source [44]. The sphere radius chosen for this model was 5 mm with a film coefficient of $150\ W/(m^2K)$ inside the sphere and $8\ W/(m^2K)$ outside of it, as illustrated in Figure 23.

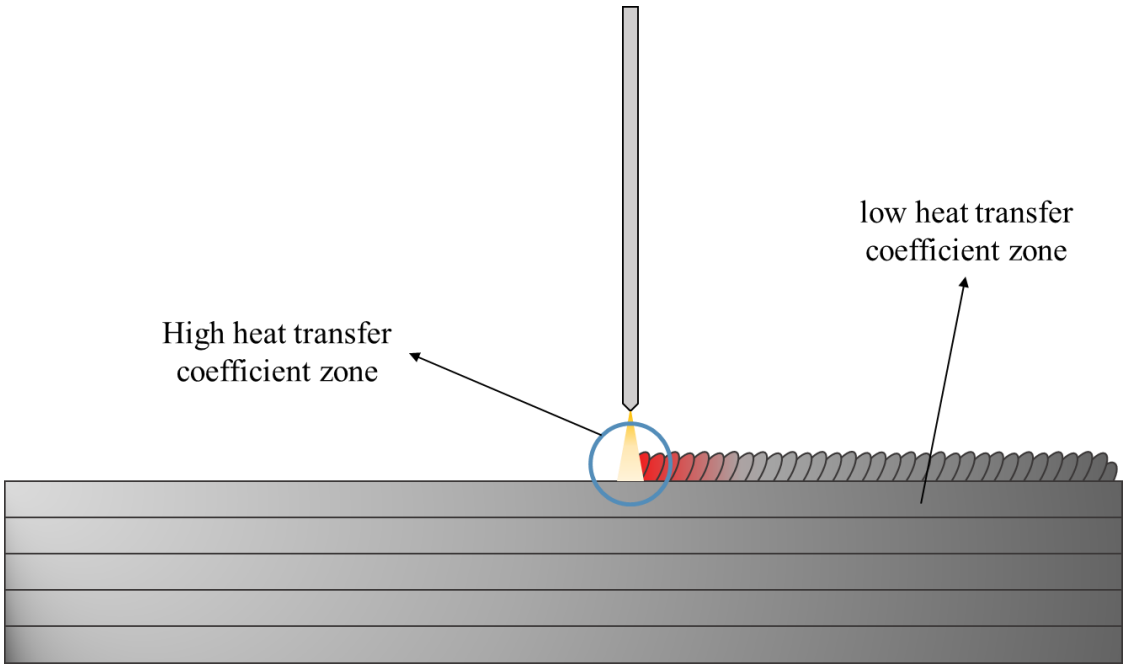

Figure 23. Illustration of thermal boundary conditions

- The conduction inside the weld pool is much higher than the conduction in the solid metal because convection due to the fluid motion in the molten pool. This effect is compensated by making the conductivity three times the value of what it is in the solid metal.

Heat source modeling

The heat source-weld pool interaction is a complex phenomenon and it is difficult to model, because of the fluid motion, viscosity, surface tension, etc. Thus, simulating the heat source and molten pool mechanics is undesirable and simulating only the heat source can achieve the needed results for the thermal analysis without the complication of simulating the weld pool dynamics. The heat source can be modeled in multiple ways as surface or volume models [45].

- Gaussian surface flux distribution

This model is a disc model with Gaussian distribution of heat on the surface. This method is effective for welding with small penetration depth. The heat source is modeled as:

$$q(r) = q(0)e^{-Cr^2} \qquad (14)$$

Where r is the radius away from the center, $q(0)$ is the maximum heat flux at the heat source, C is the concentration coefficient, and $q(r)$ is surface heat flux at a specific radius.

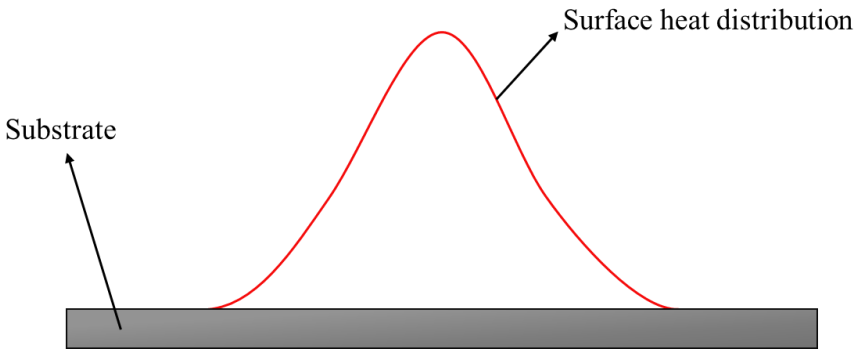

Figure 24. Gaussian surface heat distribution [45]

- Hemispherical power density distribution

This method is a volumetric heat source unlike the gaussian surface heat distribution. It is used to model laser or EB heat sources mainly. This model is formulated in the following equation:

$$q(x,y,\xi) = \frac{6\sqrt{3}Q}{c^3\pi\sqrt{\pi}} e^{-\frac{3x^2}{c^2}} e^{-\frac{3y^2}{c^2}} e^{-\frac{3\xi^2}{c^2}} \quad (15)$$

Where $q(x,y,\xi)$ is the power density, ξ is the coordinate where motion occurs and Q is the power input.

- Ellipsoidal power density distribution

This model is a more general form of the hemispherical model and it is formulated as:

$$q(x,y,\xi) = \frac{6\sqrt{3}Q}{abc\pi\sqrt{\pi}} e^{-\frac{3x^2}{a^2}} e^{-\frac{3y^2}{b^2}} e^{-\frac{3\xi^2}{c^2}} \quad (16)$$

Where $a, b\ and\ c$ are the elongation factors in x, y and z direction.

- Double ellipsoidal power density distribution (Goldak model)

This model describes a double ellipsoid shape where the front and back of the heat source have different densities, which can provide the trailing edge effect of the molten pool. It is formulated as the following:

$$q(x,y,\xi) = \frac{6\sqrt{3}fQ}{abc\pi\sqrt{\pi}} e^{-\frac{3x^2}{a^2}} e^{-\frac{3y^2}{b^2}} e^{-\frac{3\xi^2}{c^2}} \quad (17)$$

f determines front or rear of the ellipsoid, where $f_f + f_r = 2$. It is found that the best values of $f_f\ and\ f_r$ are 0.6 and 1.4, respectively. For the $a\ and\ b$ parameters, they are assumed to be half of the deposition width and penetration depth, respectively. c depends on the elongation of the heat source. Figure 25 shows the Goldak power distribution.

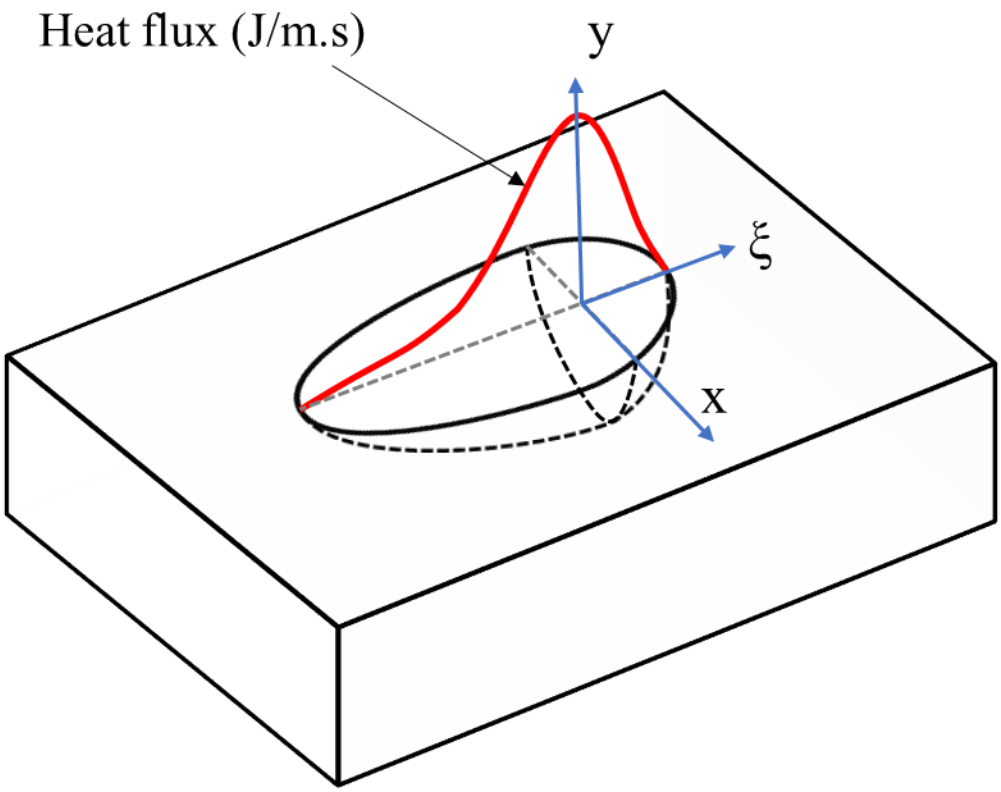

Figure 25. Goldak heat source power distribution[45]

The model in this work utilized the Goldak heat source with the following parameters:

Table 4. Heat source parameters

Parameter	Value
$\boldsymbol{Q}\ (\boldsymbol{W})$	$1800\ for\ the\ first\ 10\ layers\ and\ 1000\ for\ the\ remaining$
$\boldsymbol{Welding\ speed}\ (\boldsymbol{mm/s})$	9
$\boldsymbol{Width}\ (\boldsymbol{mm})$	5
$\boldsymbol{Depth}\ (\boldsymbol{mm})$	2
$\boldsymbol{f_f}$	0.4
$\boldsymbol{f_r}$	1.6
$\boldsymbol{a_f}\ (\boldsymbol{mm})$	$width/2 = 2.5$
$\boldsymbol{a_r}\ (\boldsymbol{mm})$	$2 * width = 10$
$\boldsymbol{b}\ (\boldsymbol{mm})$	$depth = 2$
$\boldsymbol{c}\ (\boldsymbol{mm})$	$width = 5$

DFLUX Abaqus subroutine was used to input the Goldak heat source to the model. DFLUX is used to define a nonuniform distributed flux as a function of position, time, temperature, element number, integration point number, etc. in a heat transfer or mass diffusion analysis [39]. The subroutine code is provided in the appendix.

Subroutines used

- DEFLUX: This subroutine is used to define nonuniform volumetric, surface, or mass diffusion heat fluxes as functions of time, position, element number and node number [39], such as the Goldak model mentioned earlier.
- FILM: This subroutine is used to define nonuniform film coefficients and skin temperatures as function of time, position, temperature, node numbers and element numbers [39]. This subroutine was used to specify the convection coefficients near and outside of the welding area.
- USDFLD: The USDFLD subroutine is used to define solution dependent field variables as functions of time, position, element, and node numbers [39]. Elements with different variables can have different material properties which is utilized in this model to make quiet elements during the thermal analysis.

Microstructural analysis

Geometrical modeling and meshing

The microstructural analysis is done during thermal model simulation. The results obtained during the thermal analysis are used to characterize the grain structure of each layer of the AM part. The same geometric and meshing models are used for both the thermal and microstructural analyses.

Microstructural modeling

This model was paired to the thermal analysis by adding an additional piece of code to the Fortran subroutine. The code is meant to calculate the G and R values. Using equation (*12*), we can calculate the solidification rate in the model. The G value can be derived from the heat flux equation:

$$q_i = -k\nabla T \rightarrow \nabla T = -\frac{q_i}{k} \rightarrow |\nabla T| = -\frac{|q_i|}{k} = G \qquad (18)$$

However, since the physics of the weld pool is neglected for the sake of simplicity, only the G values were used to determine the microstructure of each layer of the model. This method only gives an estimate about the microstructure and it does not provide accurate representation.

Assumptions and boundary conditions

- The simulation was done in solid-state without any consideration of weld pool physics. This would affect the microstructure simulation results significantly.
- The R values were neglected completely since they were very high due to the previous assumption.
- Only the G value was used to determine microstructure of the model. This would only give a rough estimation of the microstructure to be used in mechanical analysis.

Subroutines used

- USDFLD: USDFLD is used in this model to specify which element have columnar grains and which ones have fine equiaxed grains.

Mechanical analysis

Geometrical modeling and meshing

In terms of dimensions, the mechanical model is the same as the thermal model. However, the mechanical properties of the material were used instead of the thermal properties shown in figures 19 and 21. Additionally, the model was physically constrained to simulate the clamping of the substrate. An additional step for unclamping the part after it was cooled was added to the model. Furthermore, C3D8R 8-node linear brick elements were used instead of the DC3D8 heat transfer elements. The mesh size and configuration are still the same from the thermal model. The results from the thermal analysis was used as an input to this model since the load on the WAAM wall is only a thermal load. The effect of the microstructure is introduced to the model by giving the top 10 layers higher yield strength, since these layers have finer equiaxed grains. The yield strength of fine grains is assumed to be 450 MPa.

Assumptions and boundary conditions

- The model was rigid body constrained by fixing one corner of the substrate in X, Y, and Z translation directions, fixing another corner in the Y and Z translation directions, and finally fix another corner in the Y direction. The bottom surface was constrained in the Y direction in order to prevent bending the substrate. This configuration avoids redundant constrains and makes the model more simplistic.
- When the model is unclamped, the bottom surface of the substrate is freed from its constraint. The plate is still fixed by the corners to prevent rigid body motion. This is illustrated in Figure 17
- The top layers are given a higher yield strength to simulate the effect of fine equiaxed microstructure.

Subroutines used

- USDFLD: This subroutine is utilized to give varying mechanical properties to different elements in the model. Lower Young modulus and yield strength is given to quiet elements when the material is deposited, and higher yield strengths are given to layers with fine equiaxed grains.

IV. RESULTS AND DISCUSSION

Experimental results and model validation

The numerical model is an efficient tool to understand the effects of process parameters on residual stress in WAAM process without carrying out too many experimental trails, which can save a significant amount of time and cost. However, it is critical to validate the numerical model prior utilizing it for further investigation. In this chapter, experimental results are demonstrated first, then they will be compared with those obtained from the numerical model. Validity of the model will be discussed in detail. Finally, the effect of the most important process parameters will be investigated individually.

Thermal analysis

The Goldak heat model [45] is well-tested to re-produce temperature distribution compared to other heat models. Other models such as semi-spherical and ellipsoidal models produce lower temperatures at the thermocouple locations in the simulation. The effect of using different heat distribution models is shown in Figure 26. Figure 27 shows the thermal distribution at different times during the AM process.

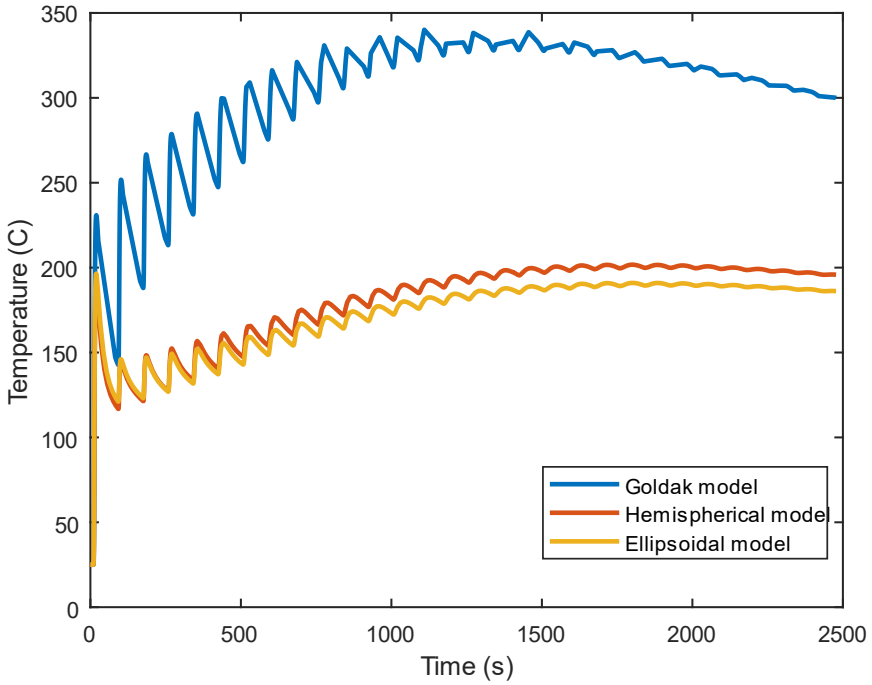

Figure 26. Thermal histories of different heat distribution models (Goldak, Hemispherical, Ellipsoidal)

Thermocouples were used to record temperature histories at five locations on the surface of substrate. The precise locations of thermocouples are shown in Figure 4. The results of temperature histories are plotted in Figures 28-32. As shown, temperature in all five locations increase until the end of deposition of the tenth layer. Then, temperatures decrease until they reach an equilibrium point at around 150 ^{o}C as shown in Figures 28-32. The predicted temperature histories matched well with measured temperature at thermocouple 3 because it is located in the middle of the substrate temperature and faces less edge effect. Normally, edge effects occur on the plate corners where surface area in contact with air increases, which creates more uncertainties for convection and radiation calculation. The larges variation happened at thermocouples 1 and 4, with maximum error percentages of 36.2% and 33.8%, respectively. The least error was at thermocouple 3 with a maximum error of 9.2%.

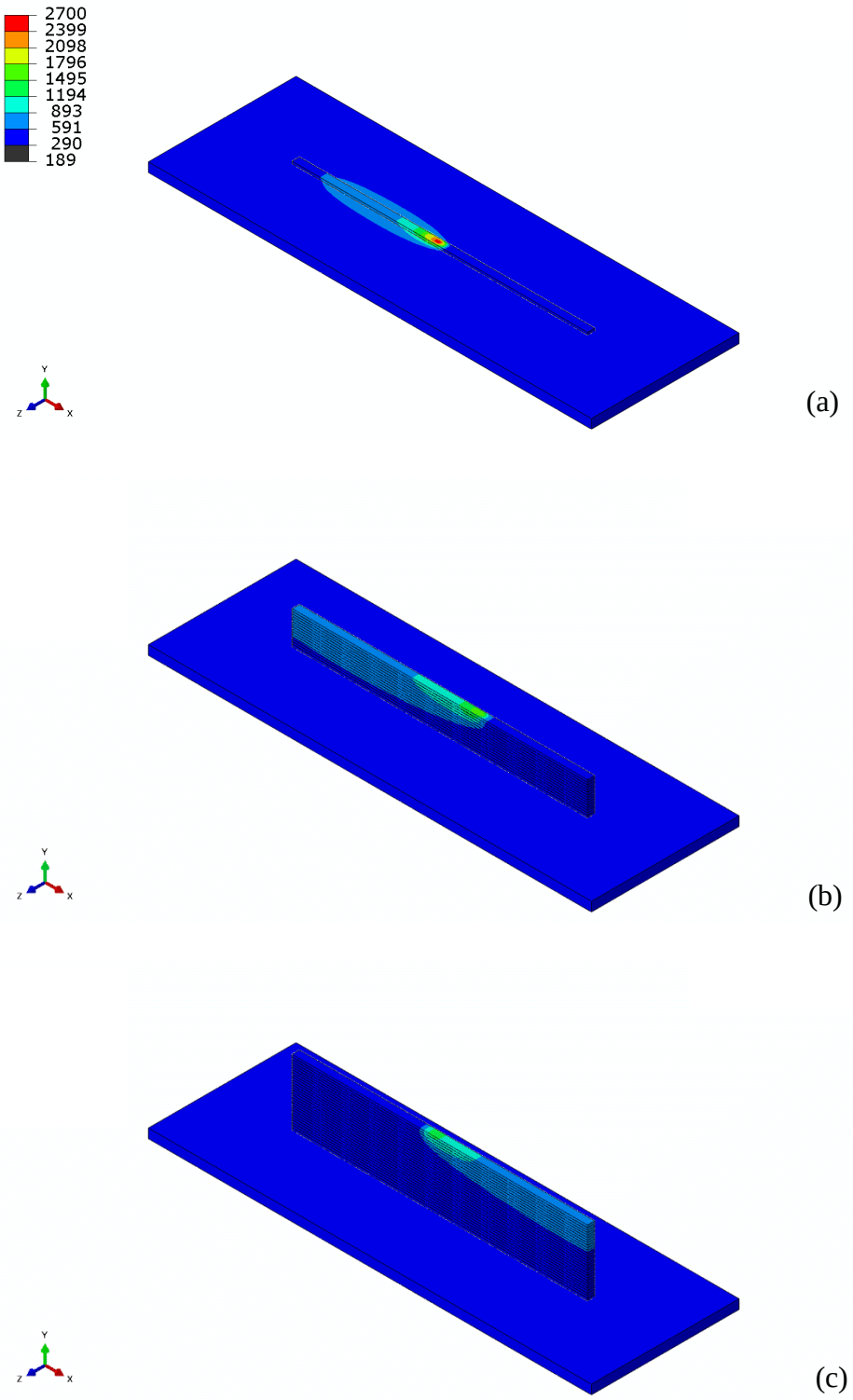

Figure 27. Temperature distributions during the WAAM process
a) Layer 1 b) Layer 15 c) Layer 30

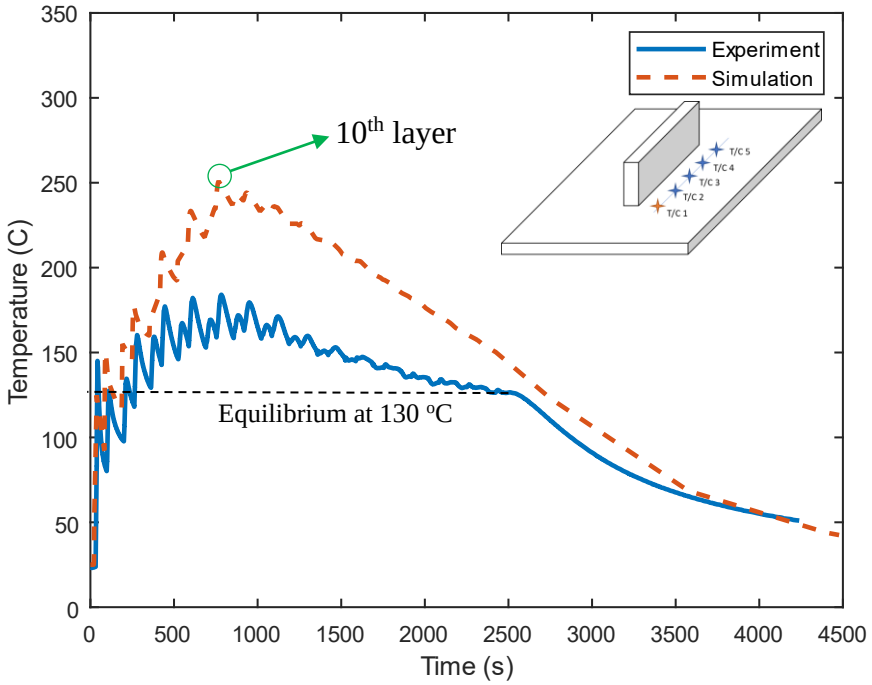

Figure 28. Thermocouple results from experiment and simulation (TC1)

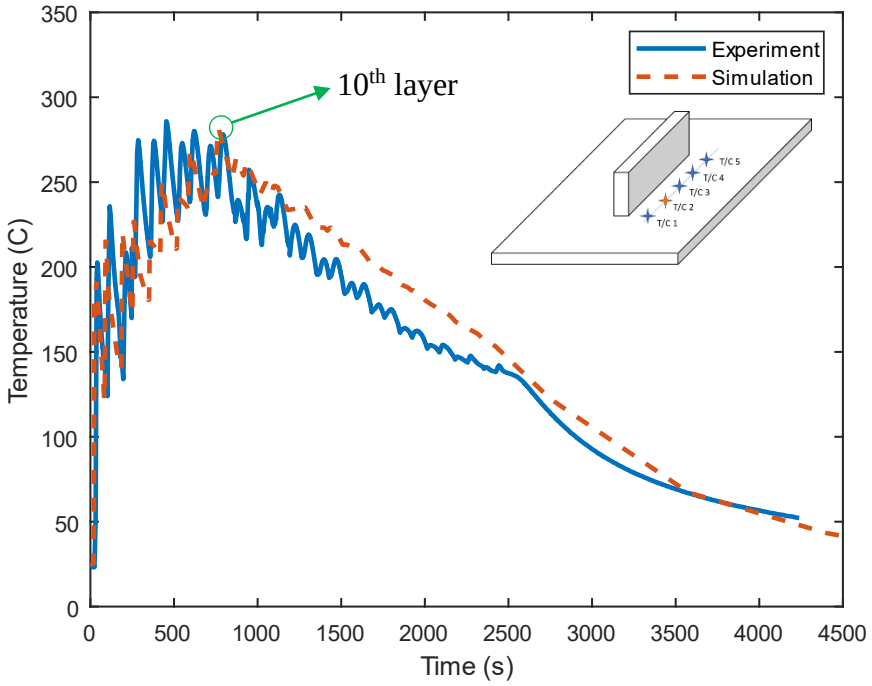

Figure 29. Thermocouple results from experiment and simulation (TC2)

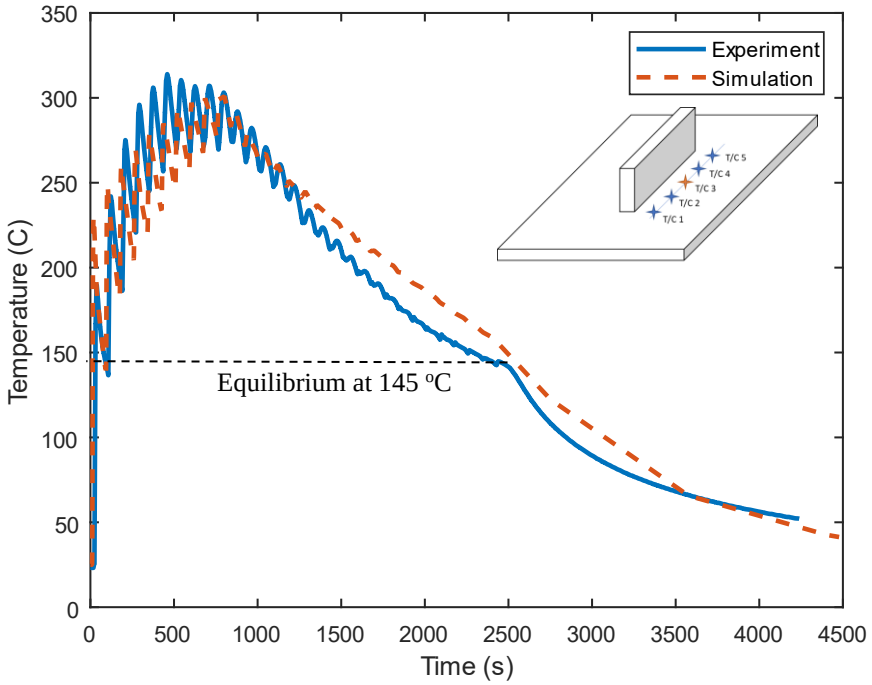

Figure 30. Thermocouple results from experiment and simulation (TC3)

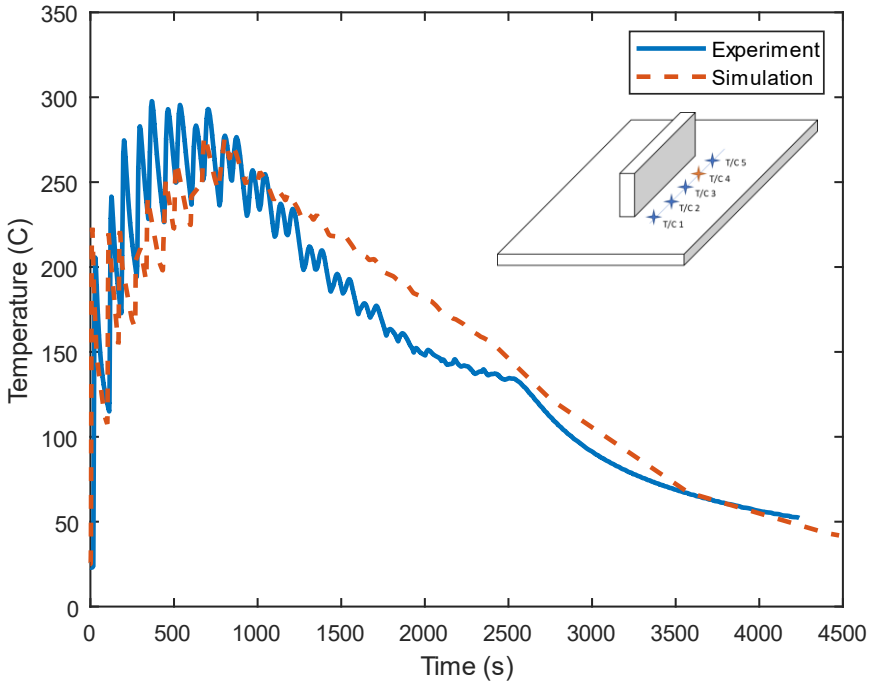

Figure 31. Thermocouple results from experiment and simulation (TC4)

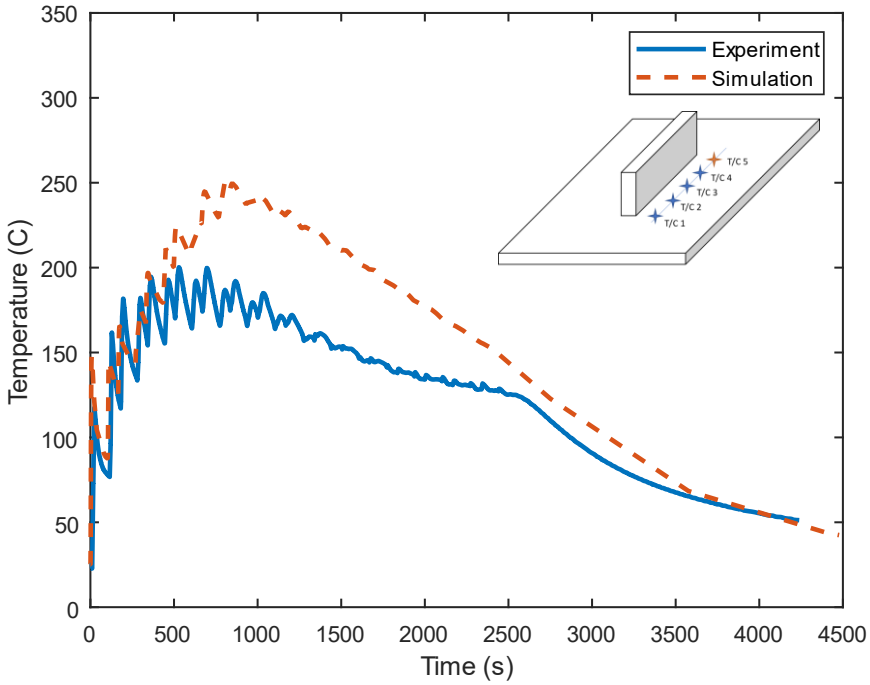

Figure 32. Thermocouple results from experiment and simulation (TC5)

Microstructure analysis

The solidification morphologies of the Inconel 718 WAAM specimen at the cross section of several layers are shown in Figures 34-37. Figure 34a shows that the top portion of a previously built layer is melted during the deposition of the subsequent layer. Therefore, remelted and inner-layer regions were identified. The dotted lines are sketched to specify the boundary between these two regions.

The austenitic columnar dendrite is a common morphology in the Inconel 718 WAAM parts. During the deposition of layers in the WAAM process, the heat flows in the build direction. As a result, the columnar dendrites grow in the vertical direction starting from the bottom of the layer till the top. The remelting of the previous layer during the WAAM process results in a continuation of growth for those columnar dendrites into the new layer after solidification. As shown in Figure

34a, the remelted region possesses a finer solidification morphology becoming coarser in the inner-layer zone. Microstructure can influence the mechanical properties of the part. As such, hardness measurement was performed to evaluate the effects of the microstructure on the mechanical properties. Figure 33 shows the hardness profile of the WAAM specimen from the layer 1 (first layer on the substrate) to layer 30 (last layer). As shown in Figure 33, there is a slight hardness increase in layers 18-30 due to formation of smaller grain the upper portion of the specimen.

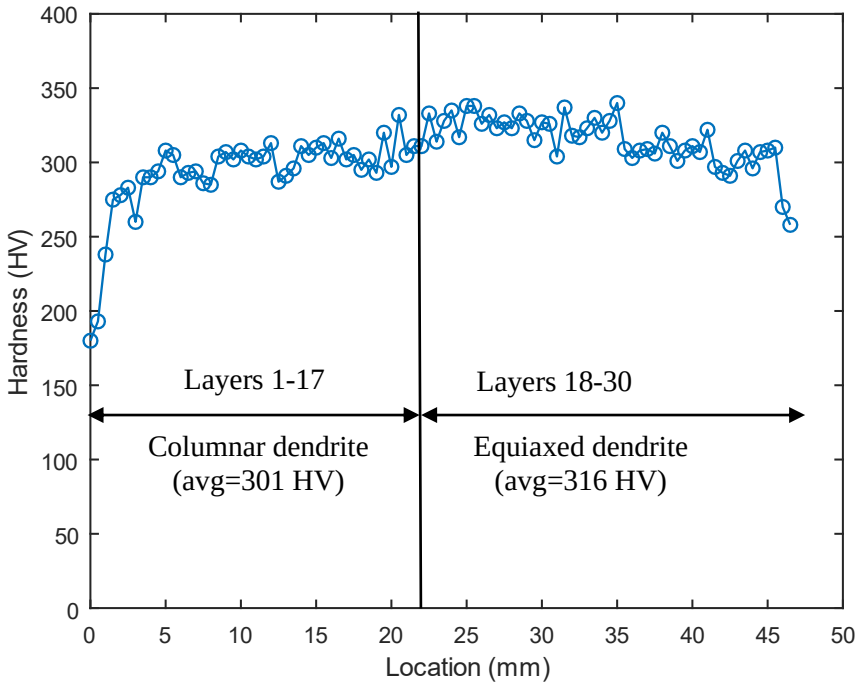

Figure 33. Hardness profile of the WAAM wall
(Results obtained from Clarkson University)

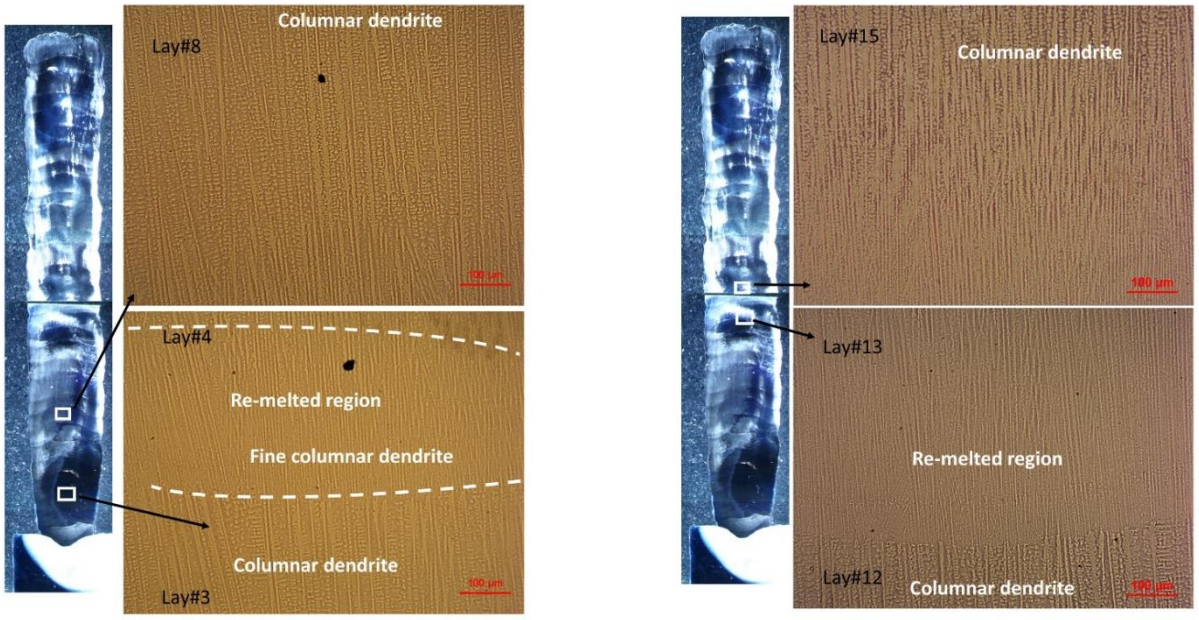

Figure 34. Microstructure of WAAM part a) Layers 3,4 and 8 b)12,13 and 15
(Done at Clarkson University)

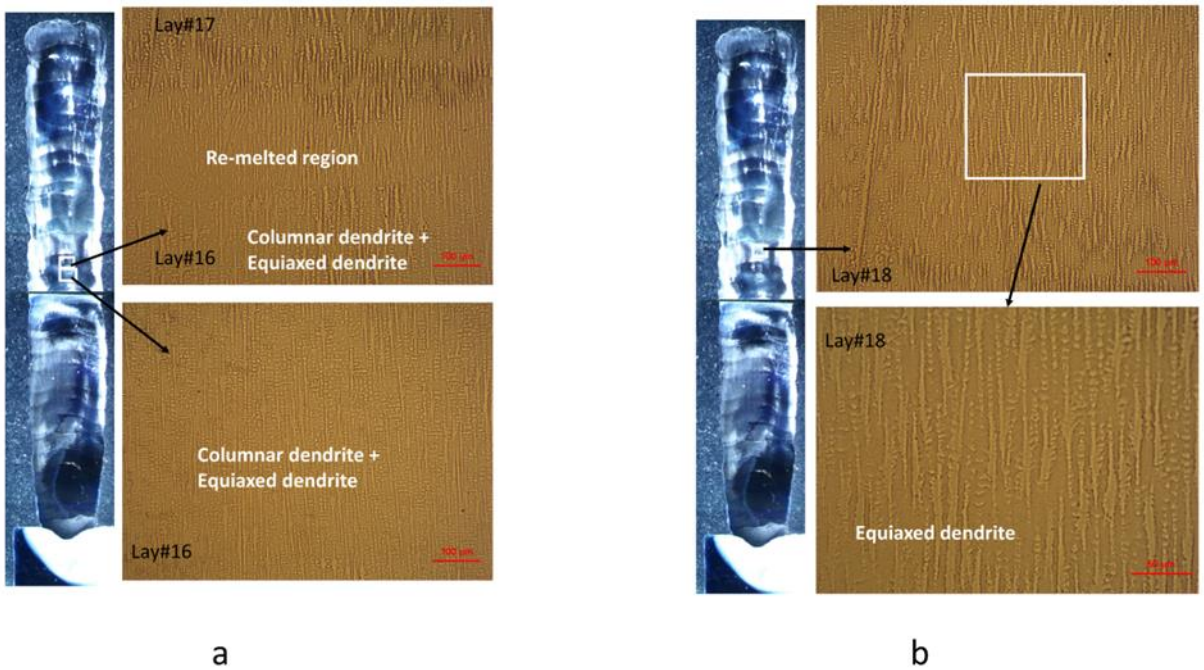

Figure 35. Microstructure of WAAM part a)16 and 17 b)18
(Done at Clarkson University)

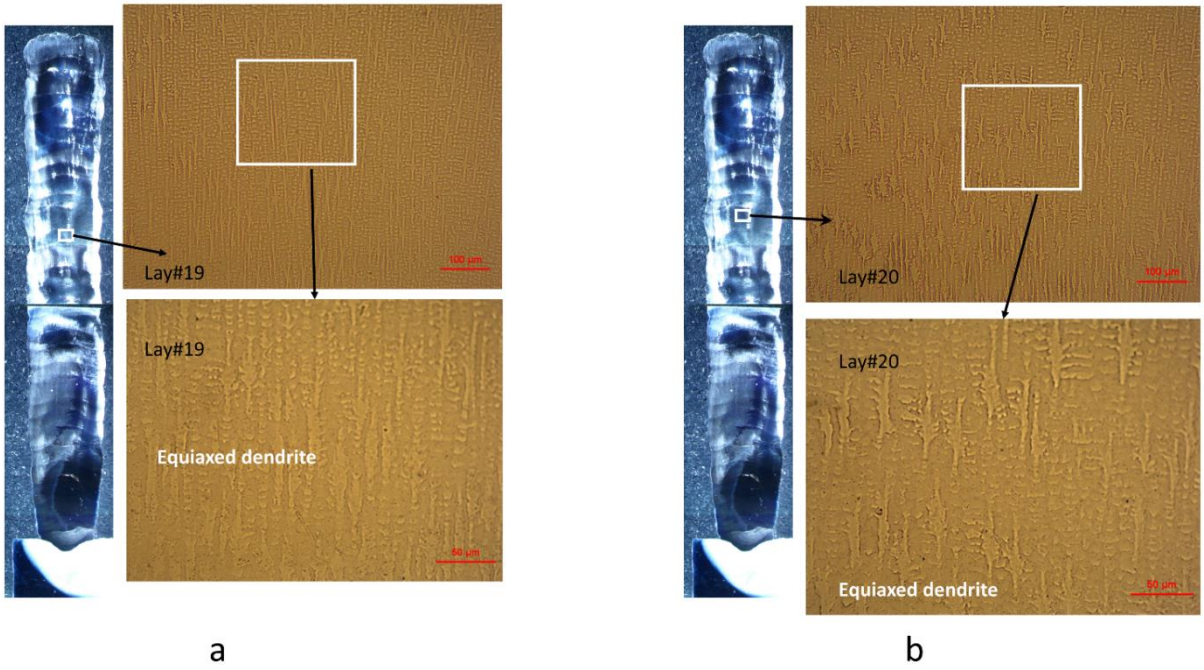

Figure 36. Microstructure of WAAM part a)19 b)20
(Done at Clarkson University)

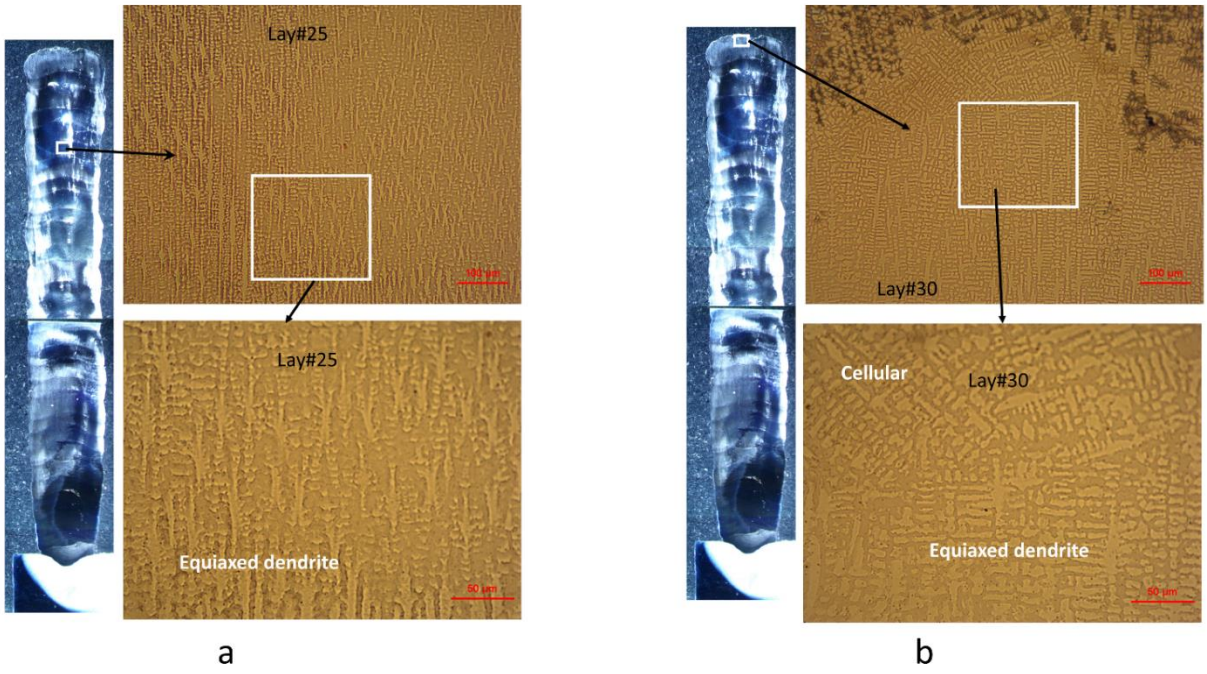

Figure 37. Microstructure of WAAM part a)25 b)30
(Done at Clarkson University)

Mechanical analysis

Figures 38 and 39 display stress distribution during WAAM process. The materials point ahead of heat source experience severe compressive load because of the thermal expansion of the new layer. On the other hand, the area trailing the welding torch has a tensile stress because of the contraction of the material due to cooling as shown in Figure 38. Generally, longitudinal stress distribution (along heat source path) in newly deposited layer is in tensile mode because of large uneven cooling and shrinkage. As such, compressive stress is induced to the previous layer to balance the total stress. This longitudinal stress will gradually keep climbing till the end of the build process where it reaches its yield point or a stress less than the yield stress.

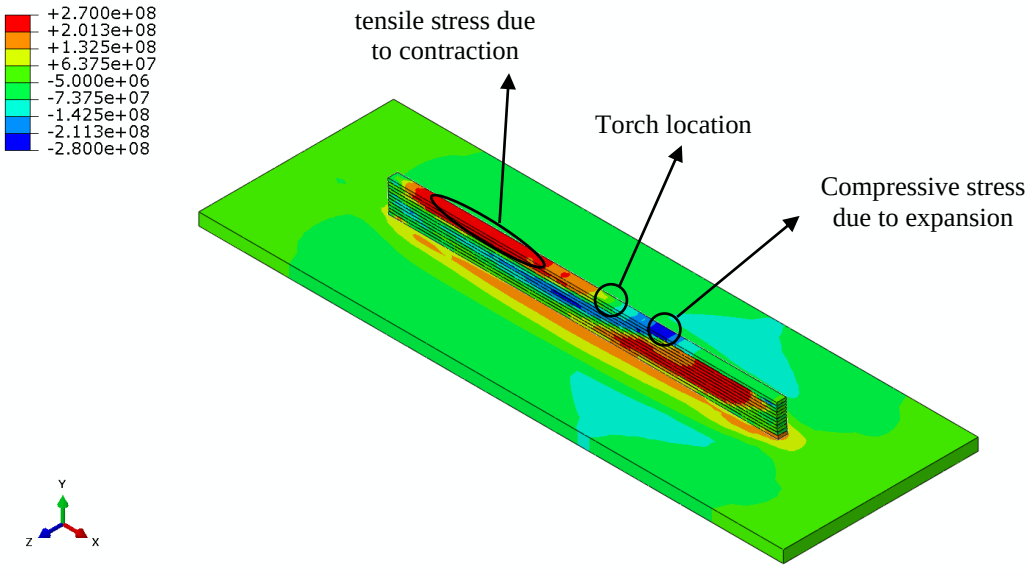

Figure 38. Longitudinal stress during the deposition process (layer 11)

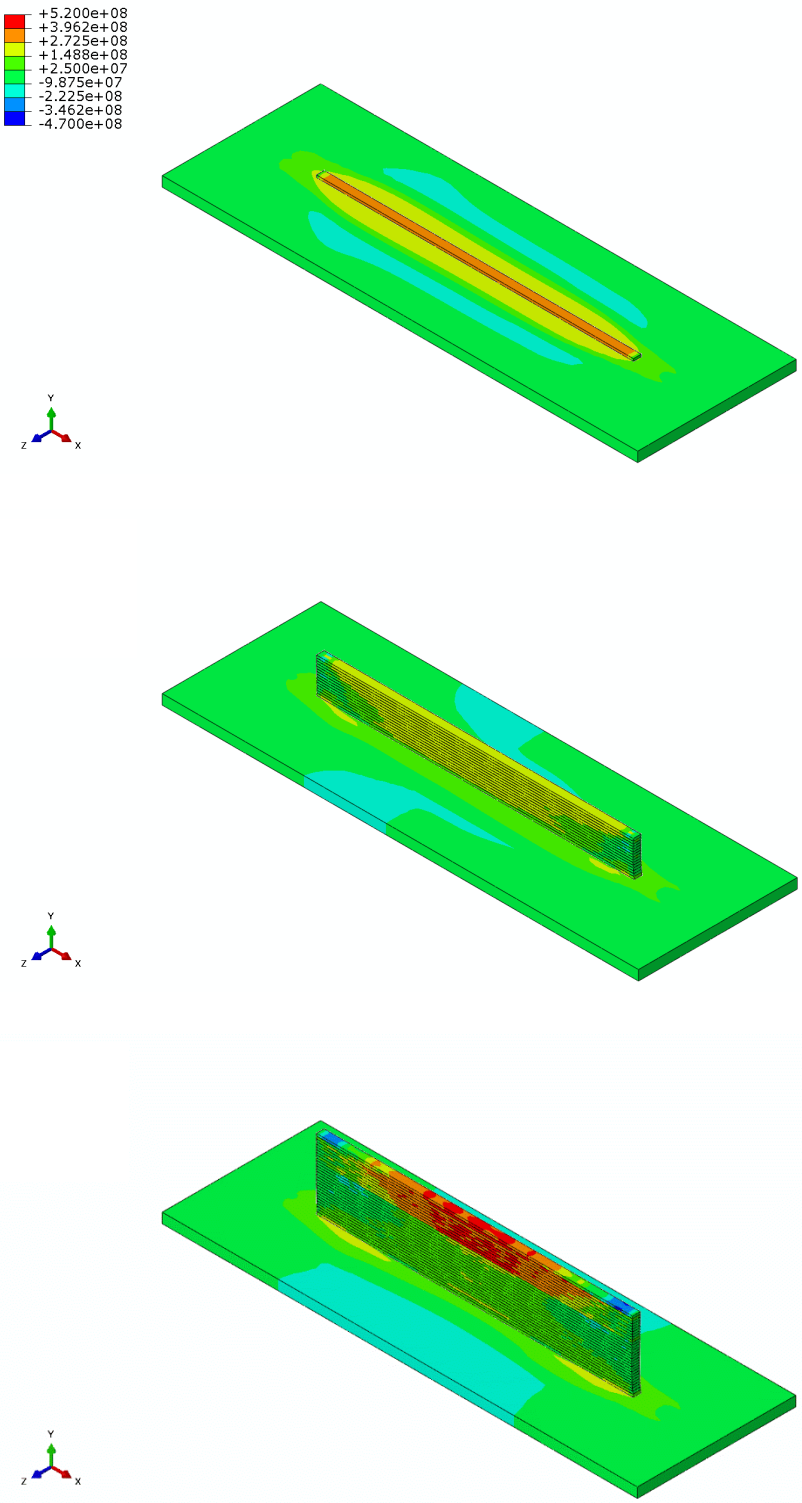

Figure 39. Longitudinal stress distributions during the WAAM process
a) Layer 1 b) Layer 15 c) Layer 30

The numerical analysis results are validated by comparing them with the experimental results obtained from neutron diffraction (ND) measurements. Figures 40-41 compares micro strain of the two numerical models (model with and without the strength of the fine microstructure (MS)) with the experimental results in longitudinal direction or weld direction. The model with MS effect shows slightly larger strain value compared with the other model. However, tensile strain at the bottom and at the top of the wall are more pronounced which is more accurate when compared with measurement data. Both models show similar tensile strain magnitudes of 2200 micro strain. The minimum value of strain is -2000 micro strain in the MS model and -500 in the model without the MS effect. The strain distribution is not symmetric in the experimental data. This can be due to uneven clamping load to retain the specimen from movement.

Figure 41 shows strain distribution in build direction. The model with MS effect appears more accurate since it has mostly compressive strains similar to the experiment, unlike the other model which has some tensile strain spots at the left and right edges of the wall. Both models do not have high tensile areas at the top regions of the part.

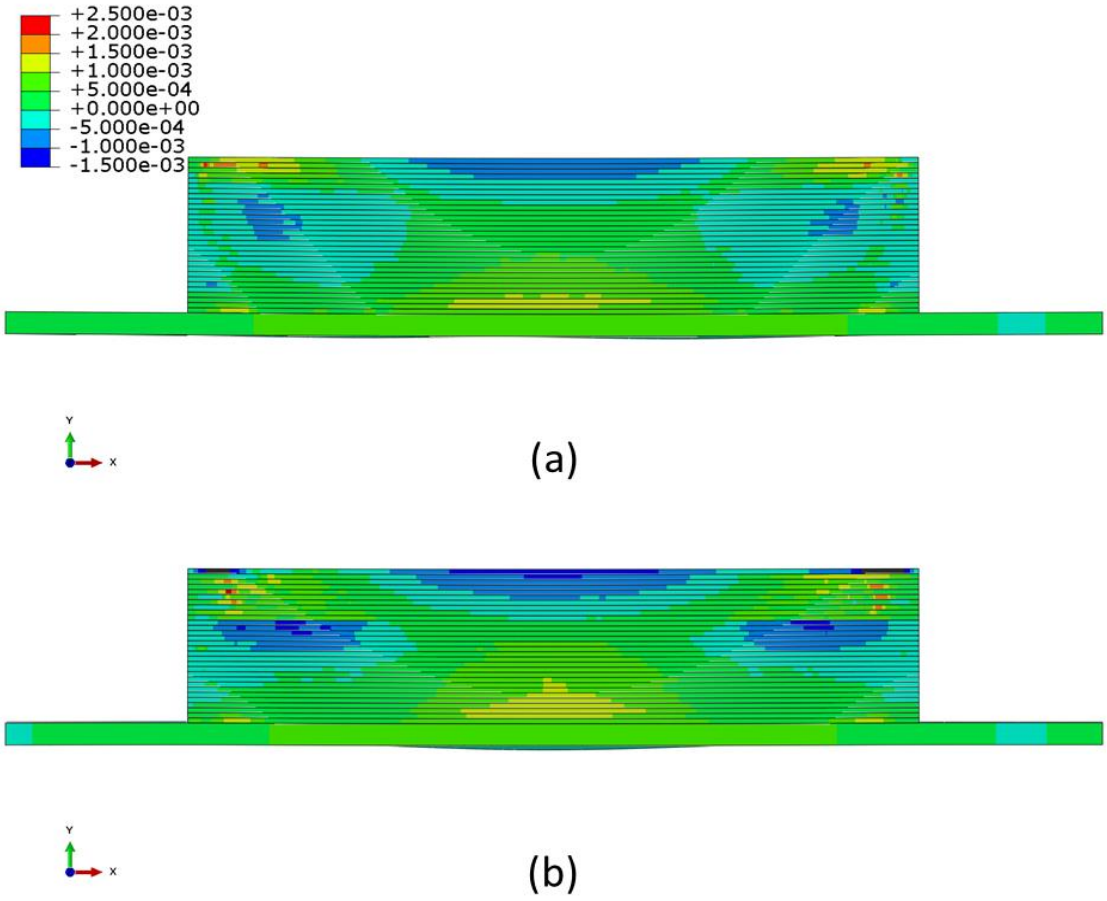

Figure 40. Longitudinal strain: (a) Model without the effect of MS (b) Model with the effect of MS (c) Experimental results (Done at Oak Ridge Lab)

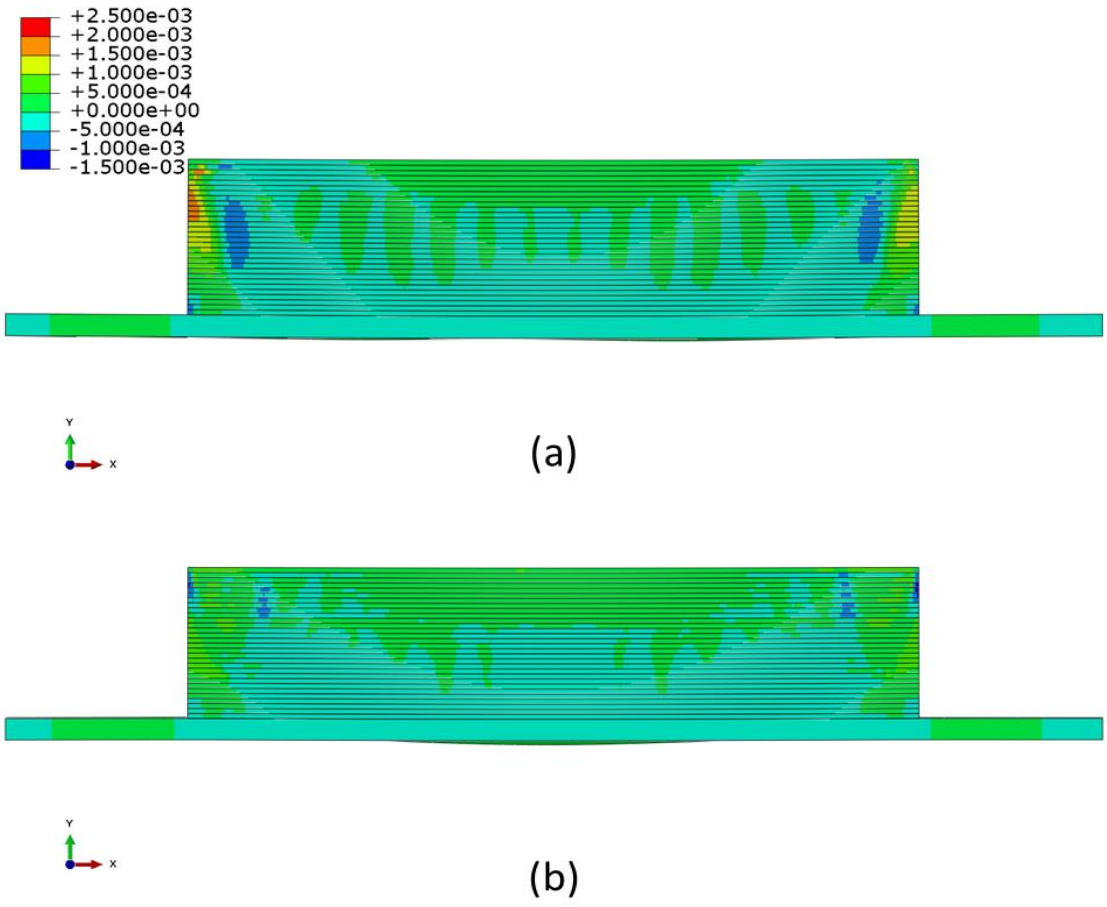

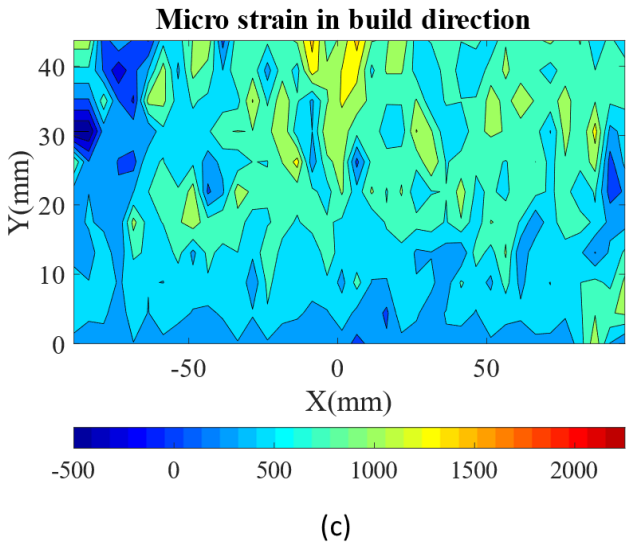

(c)

Figure 41. Build direction strain: (a) Model without the effect of MS (b) Model with the effect of MS (c) Experimental results (Done at Oak Ridge Lab)

When examining the longitudinal stress in the WAAM model at the midline shown in Figure 42 after cooling, it is noticed the stress increases layer by layer until it reaches to a maximum stress value at the top 10 layers which is about 400 MPa of tensile stress, see Figure 43. This is because the top layers which are in tension, impose compressive stresses to the lower layers, canceling their tensile stress partially. Since the last few layers are reheated during deposition, it allows them to contract in a similar manner and produce the same longitudinal residual stress. This behavior can be observed clearly when we look at the stress values in the middle section of the wall during depositing of layer 15 and layer 30, see Figure 44. For instance, the longitudinal stress in the top 5 layers, 15mm-20mm away from the substrate, flattens out after depositing 15 layers. Previous layers demonstrated significantly lower stress compared with top 5 layers.

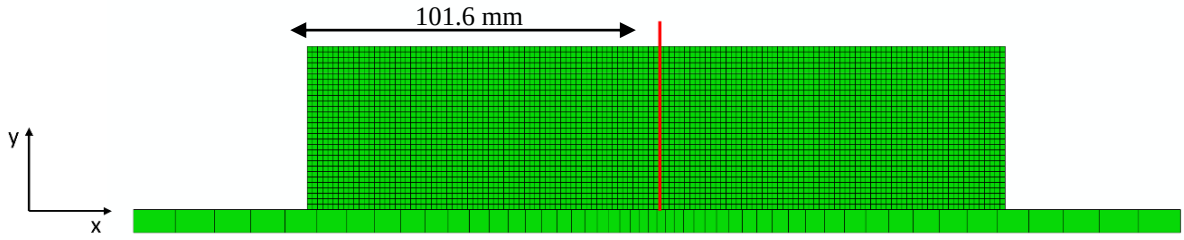

Figure 42. Stress analysis location in the model

Unclamping the part resulted stress redistribution in the WAAM part, see Figure 43. Unclamping switched the tension longitudinal stress to compressive longitudinal in the top layers. However, the lower layers still have tensile stresses but lower in magnitude.

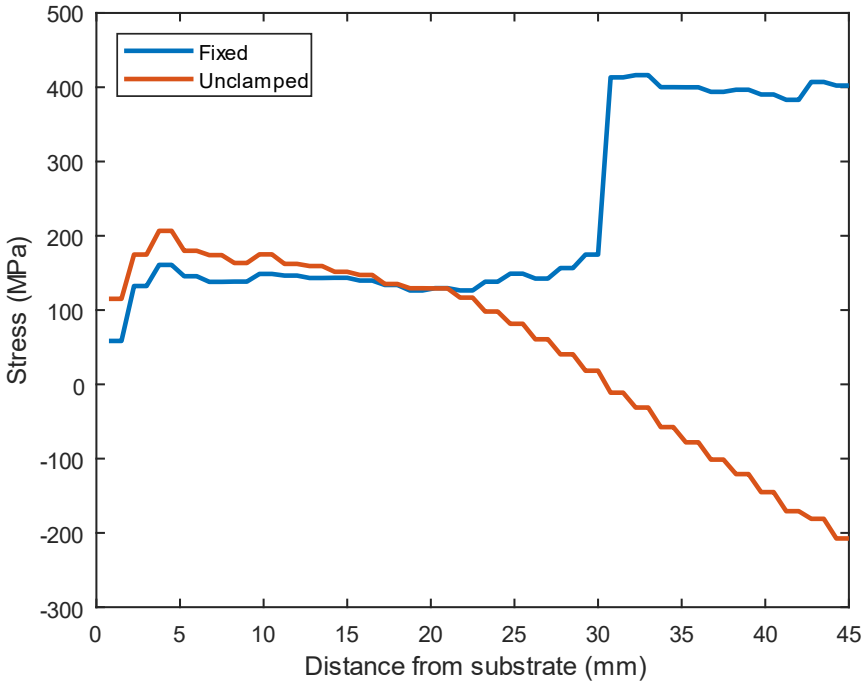

Figure 43. Longitudinal stress on the mid line of the WAAM wall

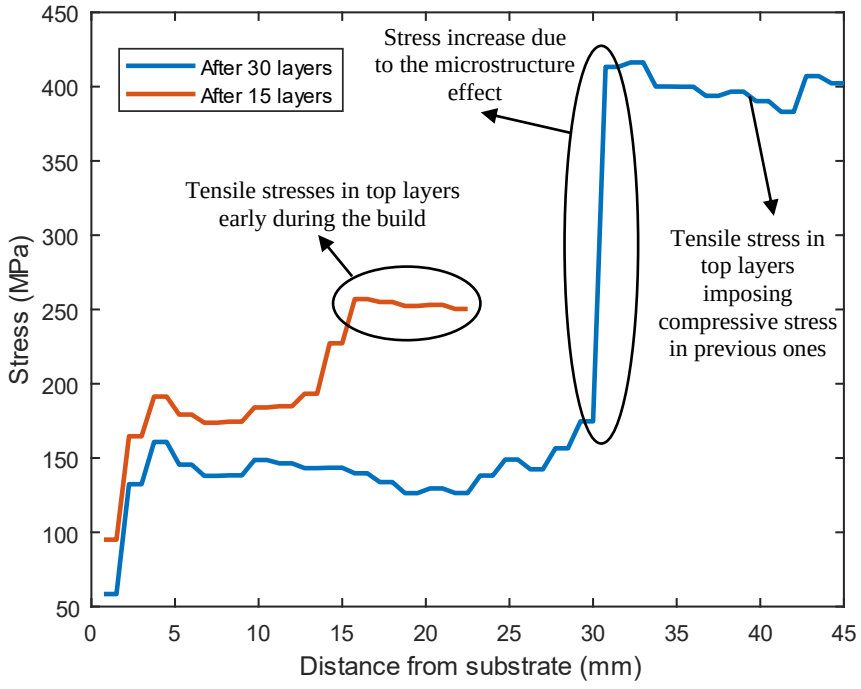

Figure 44. Longitudinal stress distribution along the midline of the WAAM wall after 15th and 30th layers

Parametric study

The validated model now is used to understand the effects of the WAAM process parameters on temperature and residual stress distributions. The parameters that have been studied are: heat source travel speed, heat source power, and the dwell time.

Travel speed

Travel speed or weld torch speed is an essential parameter in the WAAM process. This parameter affects the width of the welding bead, the metal deposition behavior, and the thermal and mechanical profiles of the part. Changing the torch speed while maintaining the same input power (1850-1000 Watts) changes the heat input per unit length. Using equation (*19*), the heat input is calculated, and it is shown in Table 5.

$$Heat\ input(J/mm) = \frac{Input\ power\ (kW)}{torch\ speed\ (mm/s)} \qquad (19)$$

Table 5. Heat input at different travel speeds using 1850 and 1000 Watts of power

Travel speed (mm/s)	Heat input (J/mm)
8	0.23-0.13
9	0.21-0.11
10.8	0.17-0.9

However, in this section, only the thermal and mechanical effects are discussed. In one model, the welding speed was set to 10.8 mm/s, increased by 20% of the original 9 mm/s. In the other model, the speed was decreased to 8 mm/s. Lowering the speed by 20% (7.2 mm/s) was not possible due to simulation convergence issues resulted from heat accumulation. Figure 45 shows the

temperature histories of three models (the original, with increased speed and with reduced speed) at the location of thermocouple number 3.

Increasing the speed reduced the overall temperature of the part since less heat is added during the WAAM process. This increase allowed the maximum temperature to decrease by 15.1%. On the other hand, reducing the speed increased the maximum temperature of the part by only 6.8%.

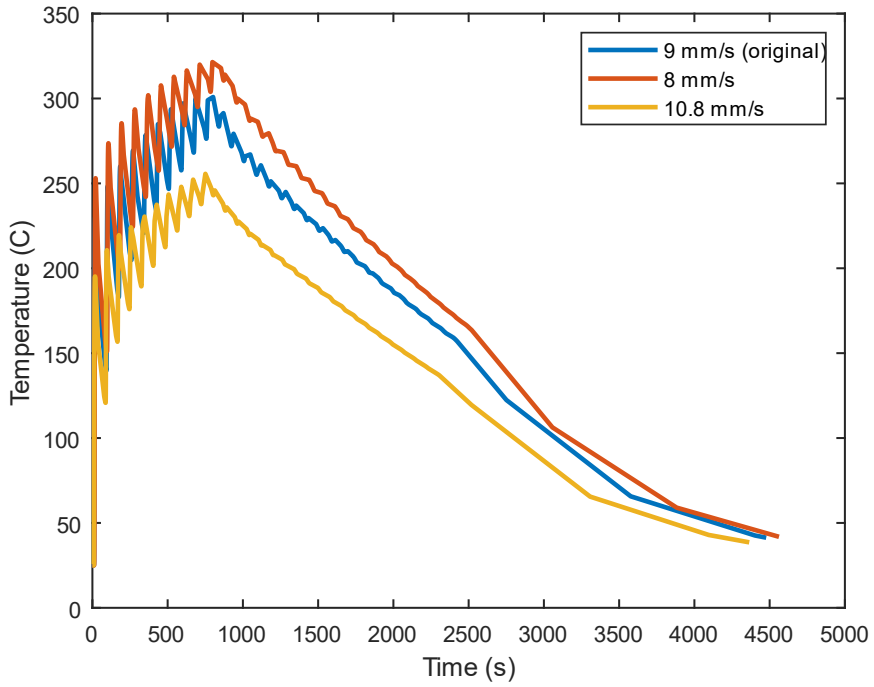

Figure 45: Temperatures at thermocouple 3 location using different travel speeds

Comparing the results from the stress analysis of various travel speeds, the travel speed is directly proportional to the longitudinal stress in the part when fixed, as shown in Figure 46. This is due to the reduced heat input when increasing the speed, causing uneven contraction and thus higher stresses. Nonetheless, as seen in Figure 47, the model with the lower travel speed has higher compressive stress while the high-speed model has relatively lower stress. Build direction stress increases when increasing the travel speed when fixed and after unclamping, as illustrated in figures 48 and 49.

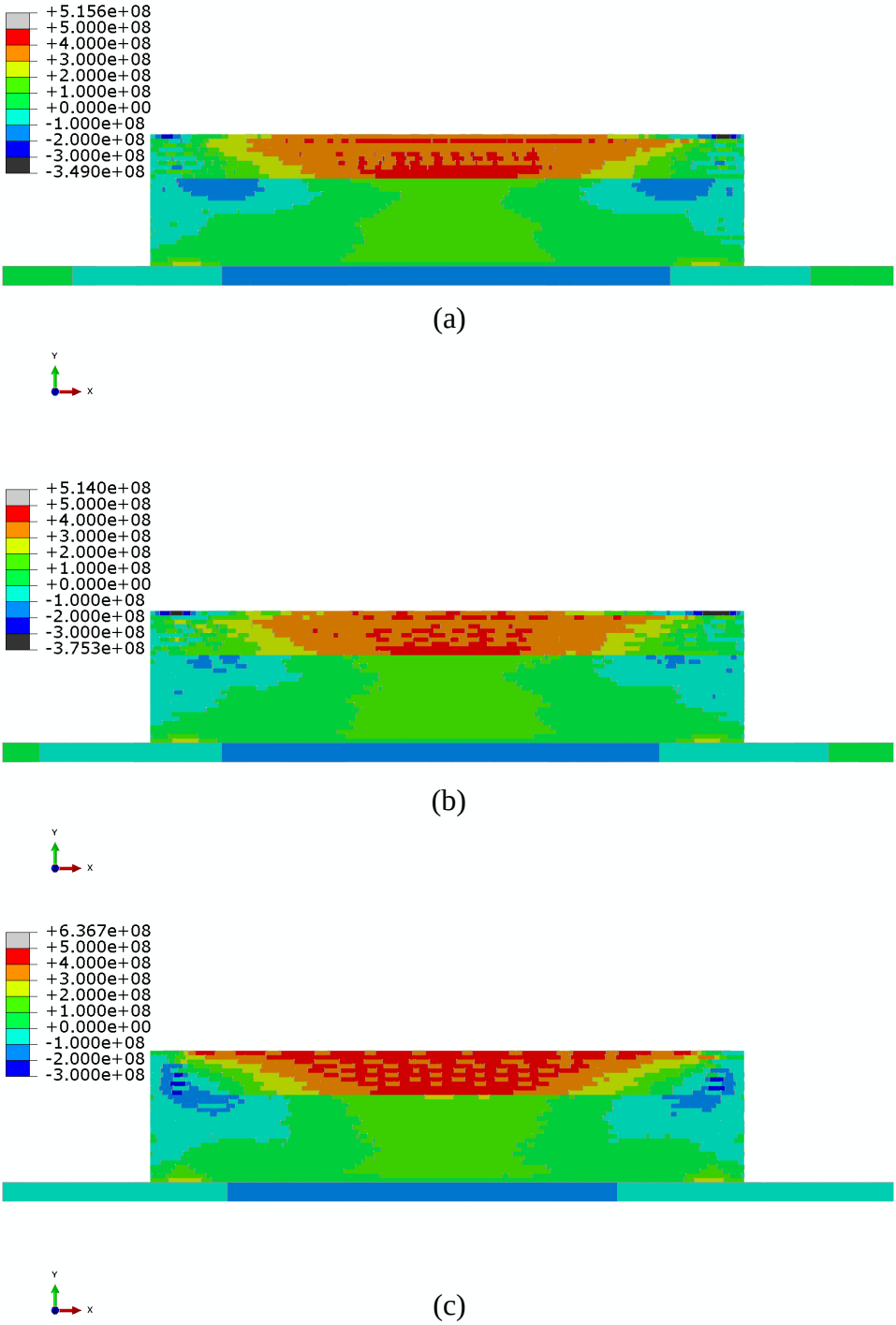

Figure 46. Longitudinal stress distribution before unclamping
(a) 8 mm/s (b) 9 mm/s (Original) (c) 10.8 mm/s

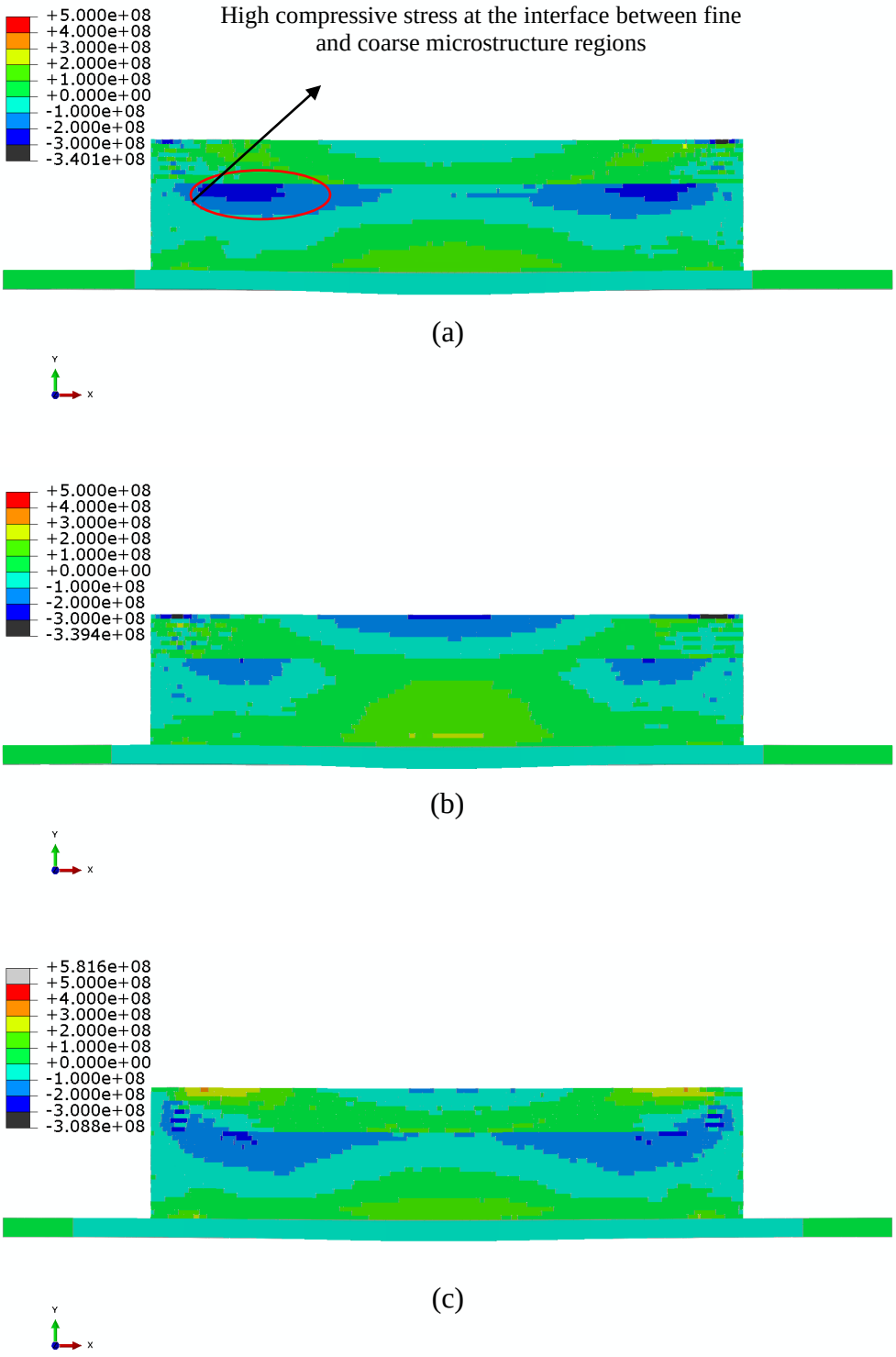

Figure 47. Longitudinal stress distribution after unclamping
a) 8 mm/s (b) 9 mm/s (Original) (c) 10.8 mm/s

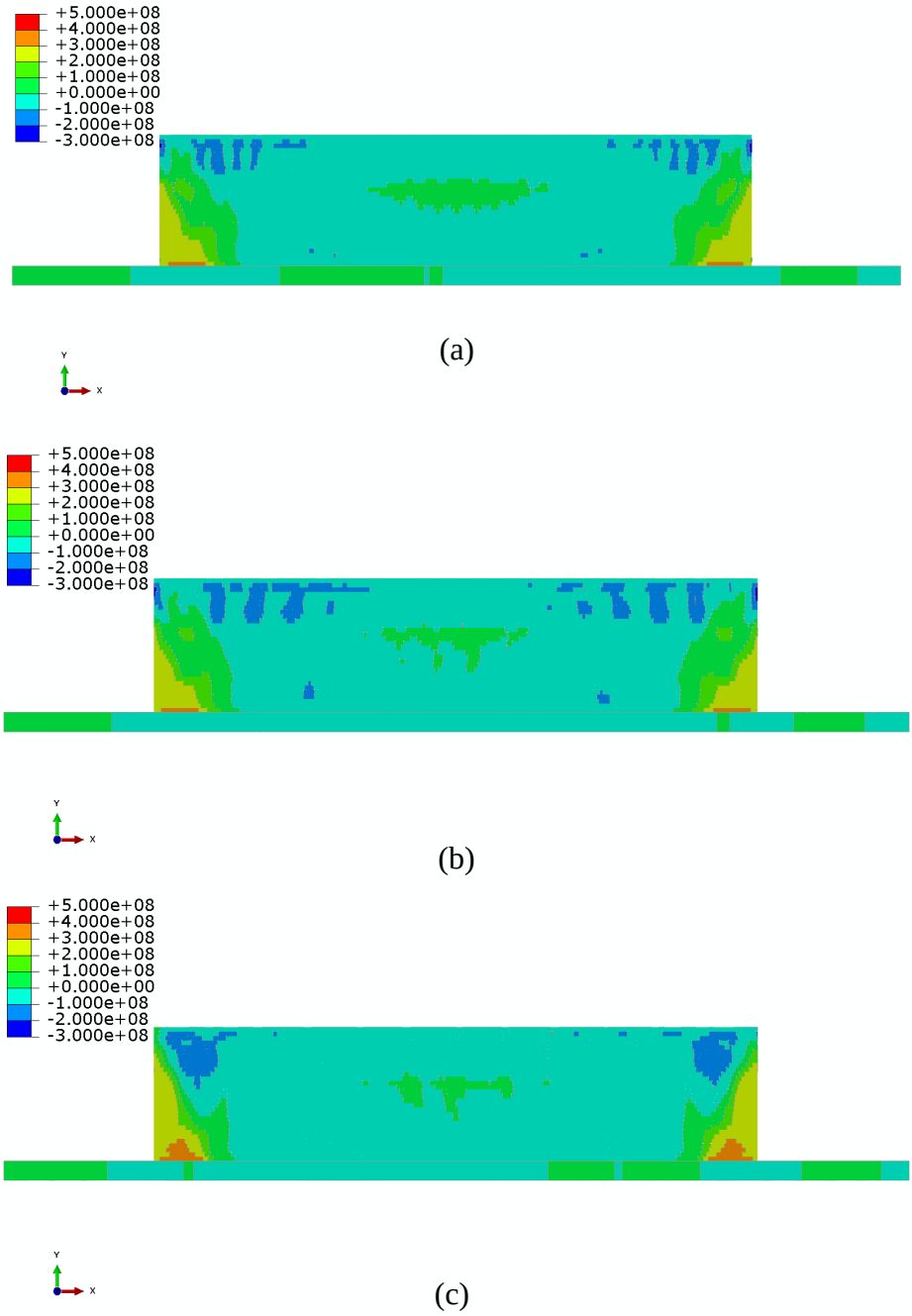

Figure 48. Build direction stress distribution before unclamping
a) 8 mm/s (b) 9 mm/s (Original) (c) 10.8 mm/s

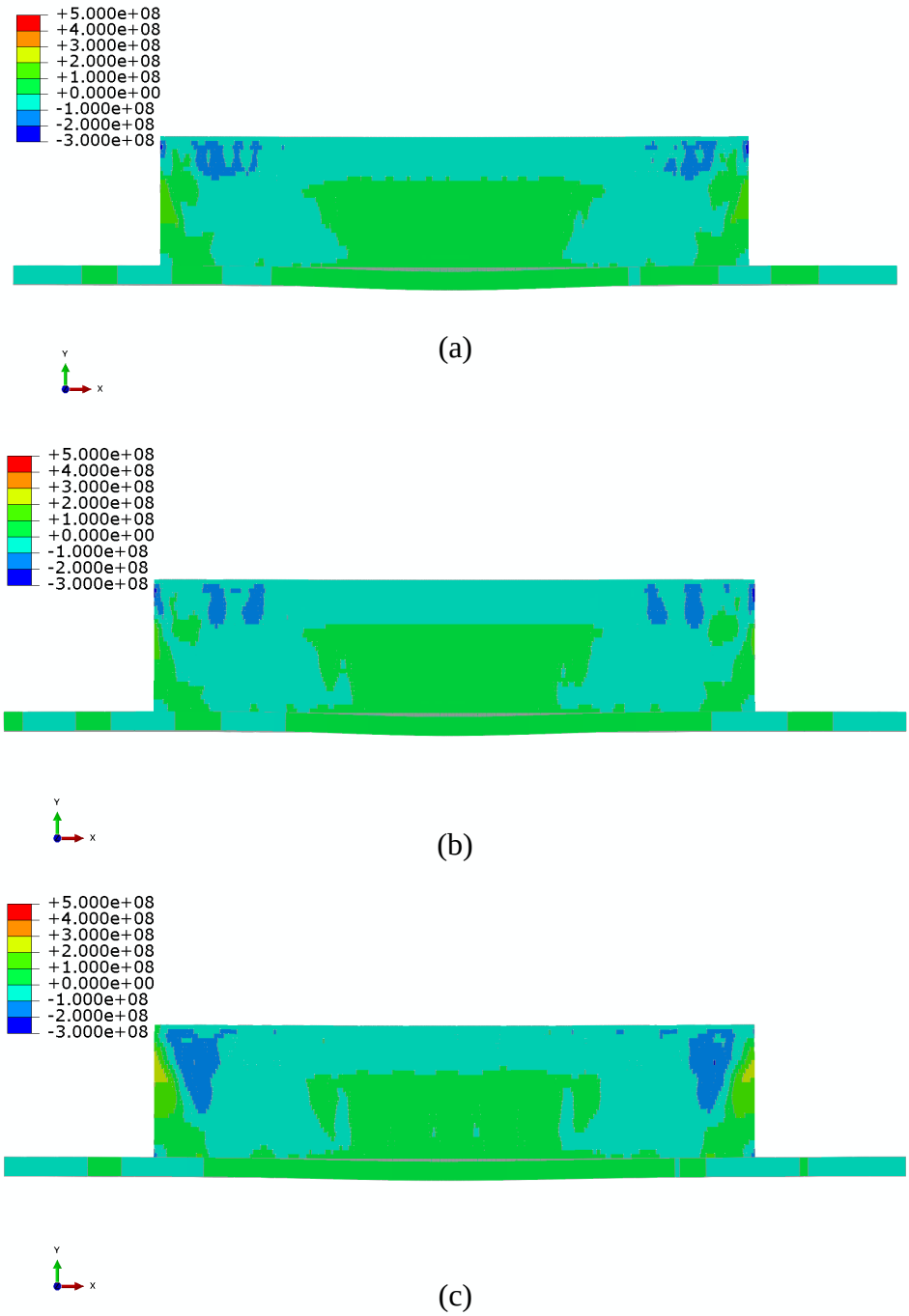

Figure 49. Build direction stress distribution after unclamping
a) 8 mm/s (b) 9 mm/s (Original) (c) 10.8 mm/s

The deflection in the y direction is disproportional to the travel speed as shown in Figure 50. Increased heat during the build process causes more warpage in the part. The 10.8 mm/s model shows 5.9% less deflection compared to the original model with a maximum displacement of 1.649 mm and 1.752 mm for the 10.8 mm/s model and original model, respectively. The 8 mm/s model shows significant warpage up to 2.198 mm with 25.4% percentage difference, thus concluding that increasing the travel speed from 8 to 9 mm/s can reduce the warpage in the part considerably.

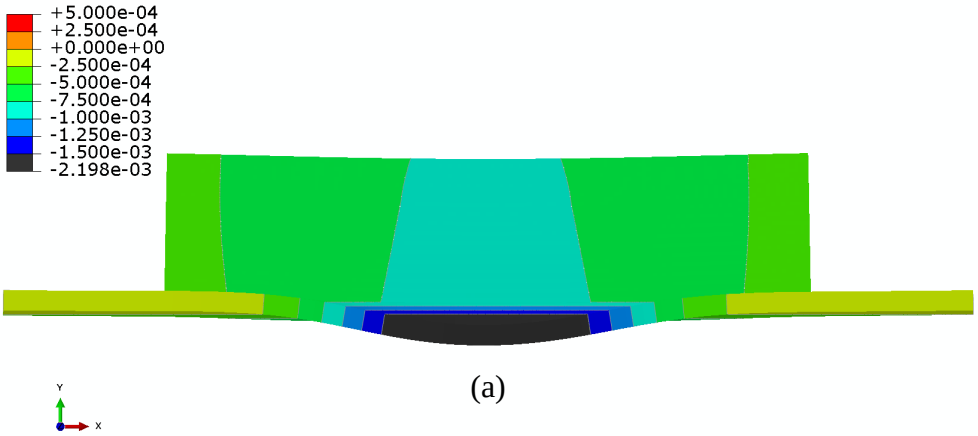

(a)

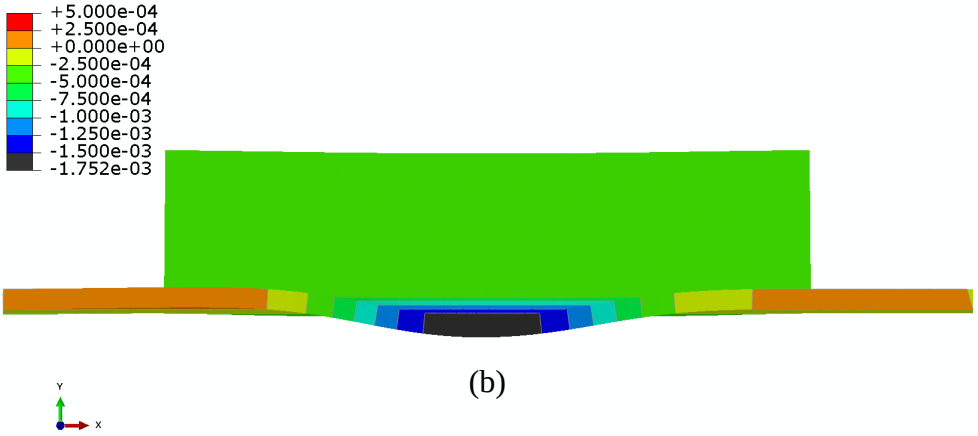

(b)

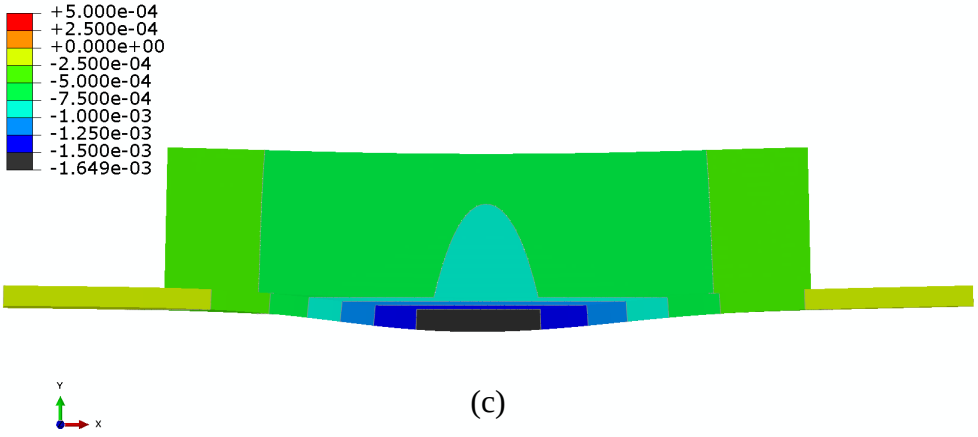

(c)

Figure 50. Displacement in y direction (in mm) after unclamping
a) 8 mm/s (b) 9 mm/s (Original) (c) 10.8 mm/s

Input power

Changing the welding power of the WAAM process affects the splatter behavior of the bead, its shape (height and width), and weld pool temperature as well as the residual stresses and temperature distribution in the part. Using equation (*12*), the heat input per unit length is calculated and the results are shown in Table 6.

Table 6. Heat input per unit length using different input powers and 9 mm/s travel speed

Input Power (kW)	Heat input (J/mm)
1.48-0.8	0.16-0.09
1.85-1	0.21-0.11
2.22-1.2	0.25-0.13

As expected, increasing the power increases the temperature of the part during the WAAM process and vice versa as illustrated in Figure 51.

The maximum temperature increases by 14.4% when the maximum power is increased by 20% from the original value conducted in the experiment. However, decreasing the input power by 20% resulted in a 24.1% decrease in the peak temperature when compared to the original. This is due to the increased heat transfer at higher temperatures in the weld pool through convection and radiation.

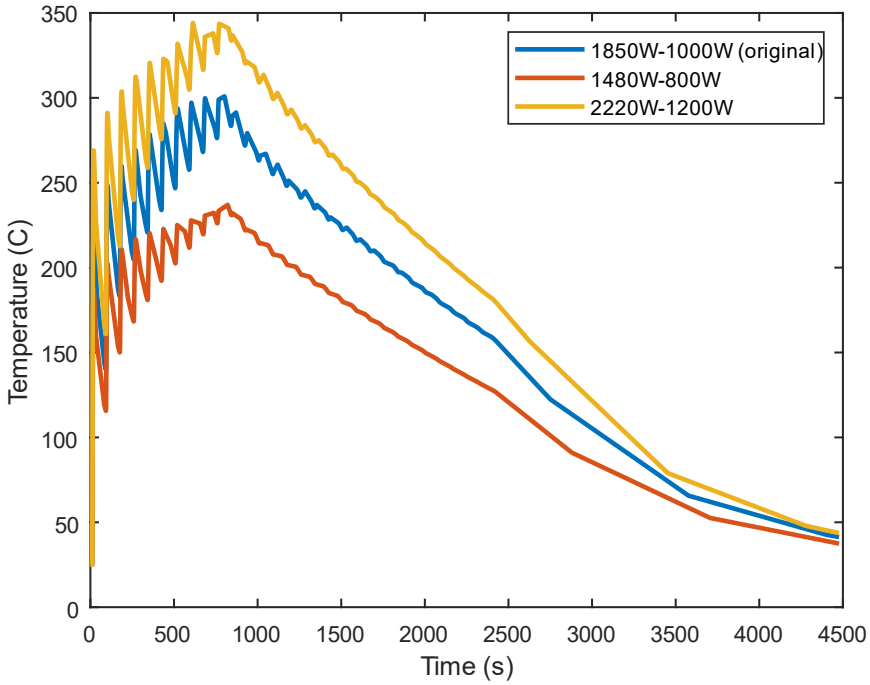

Figure 51. Temperatures at thermocouple 3 location using different deposition power

Figures 52-55 show the longitudinal and build direction stresses in models with different input powers. Stress has a direct relationship with the input power. This is probably because of the increased contraction rates when using higher input powers. However, the change in stress is minimal when increasing the maximum power from 1850W to 2220W and this applied to both longitudinal and build direction stresses. The change in stress when decreasing the power to 1480W is more noticeable especially in the top part of the wall.

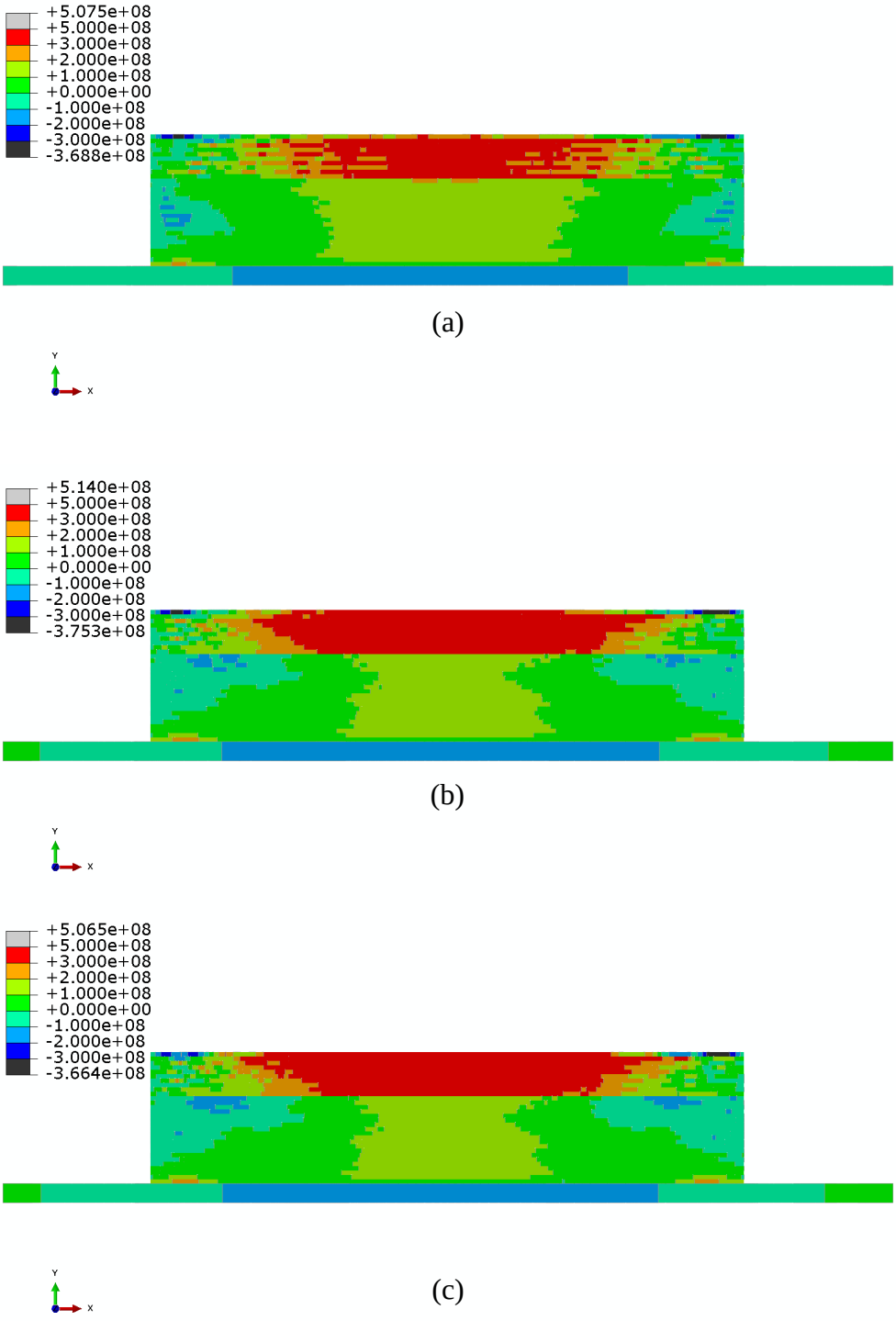

Figure 52. Longitudinal stress distribution before unclamping
(a) 1480W (b) 1850W (Original) (c) 2220W

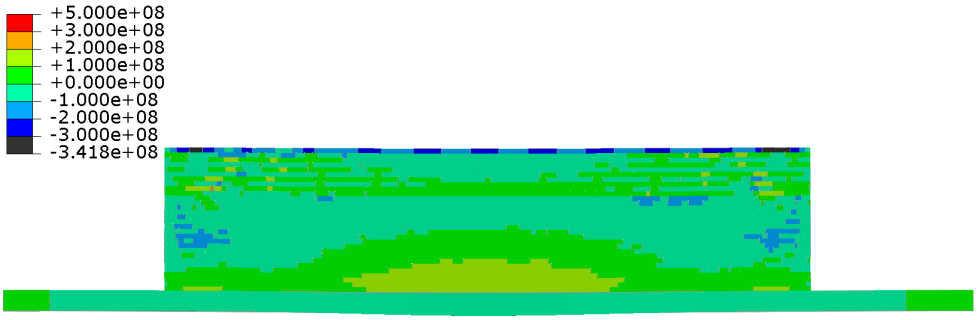

(a)

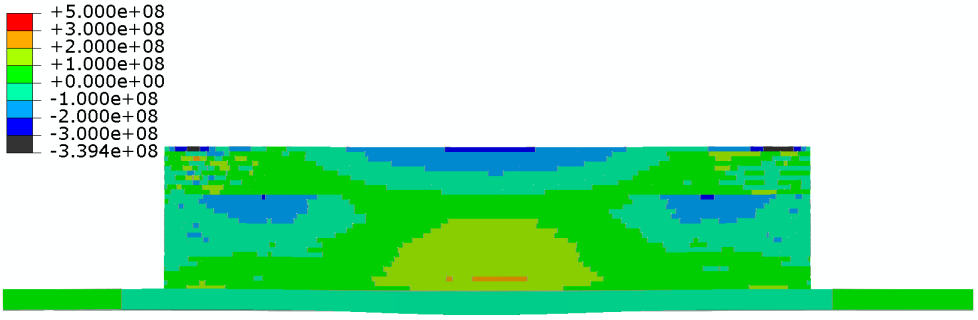

(b)

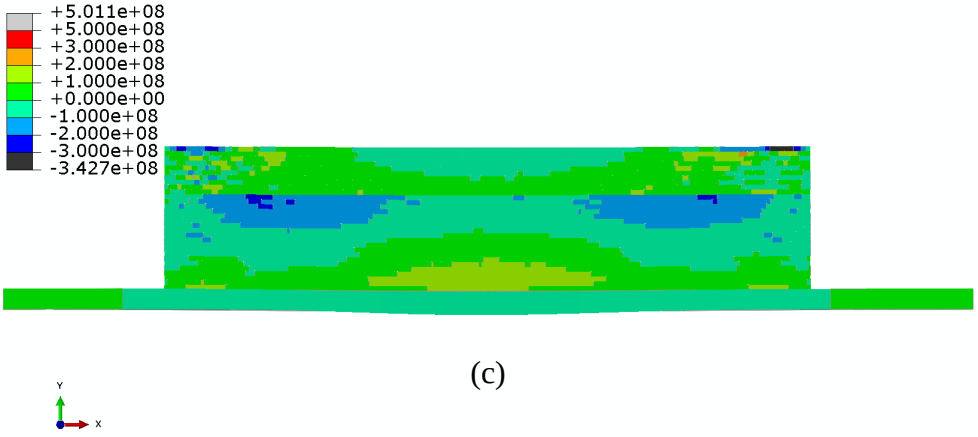

(c)

Figure 53. Longitudinal stress distribution after unclamping
(a) 1480W (b) 1850W (Original) (c) 2220W

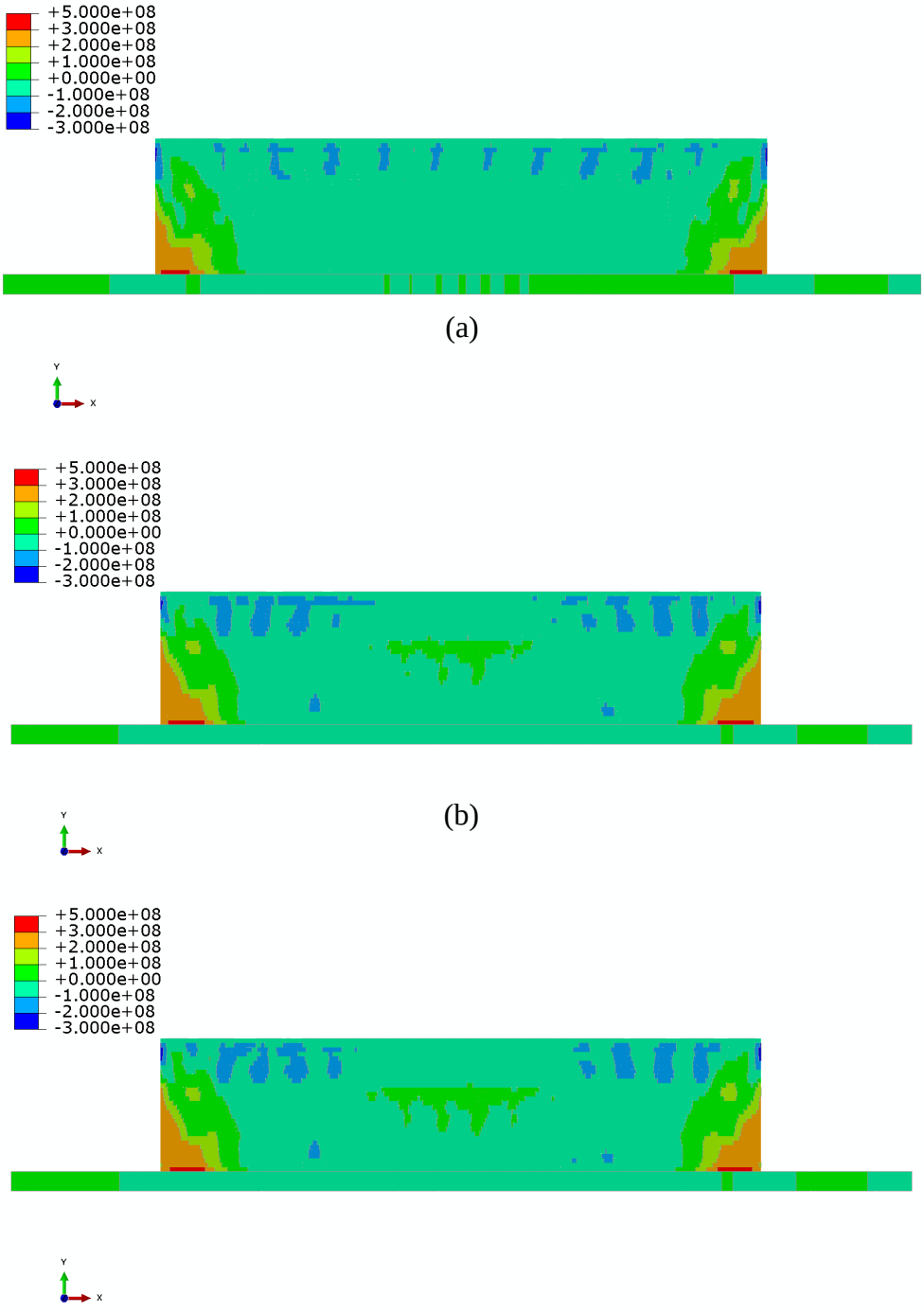

Figure 54. Build direction stress distribution before unclamping
(a) 1480W (b) 1850W (Original) (c) 2220W

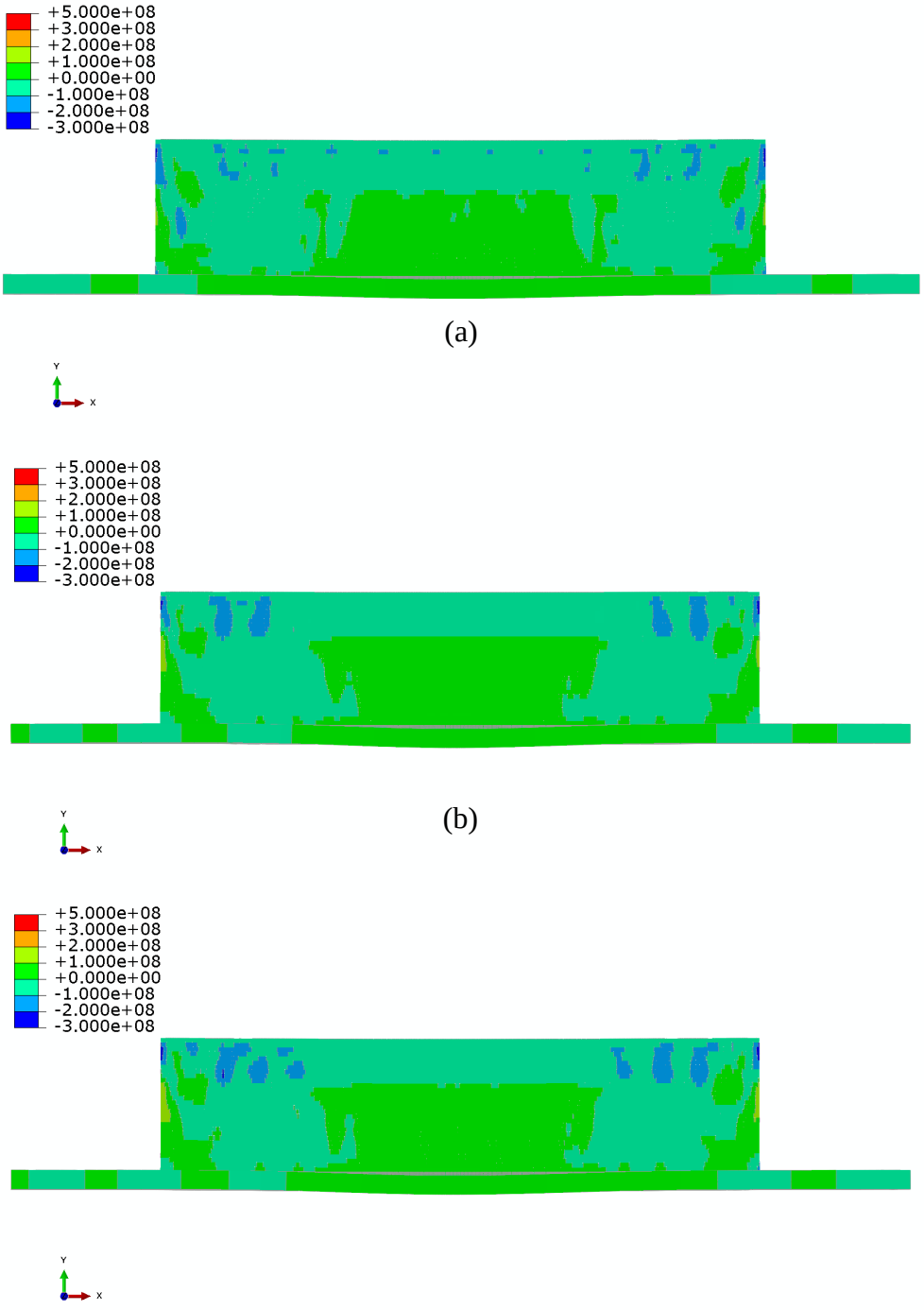

Figure 55. Build direction stress distribution after unclamping
(a) 1480W (b) 1850W (Original) (c) 2220W

Increasing the heat source power increases the displacement happening in the AM part, because of the increased heat input. Increasing the power to 2220W caused an increase in the displacement by 11.6% with a maximum displacement of 1.956 mm in the vertical axis, while decreasing the power to 1480W decreased the displacement by 3.3% with a maximum deformation of 1.694 mm in the y axis. Figure 56 shows the vertical displacement distribution when changing the input power parameter. Nevertheless, the overall distortion in both the higher and lower power models is larger than original. This reveals that using 1850W for making this part is optimal in terms of minimizing distortion.

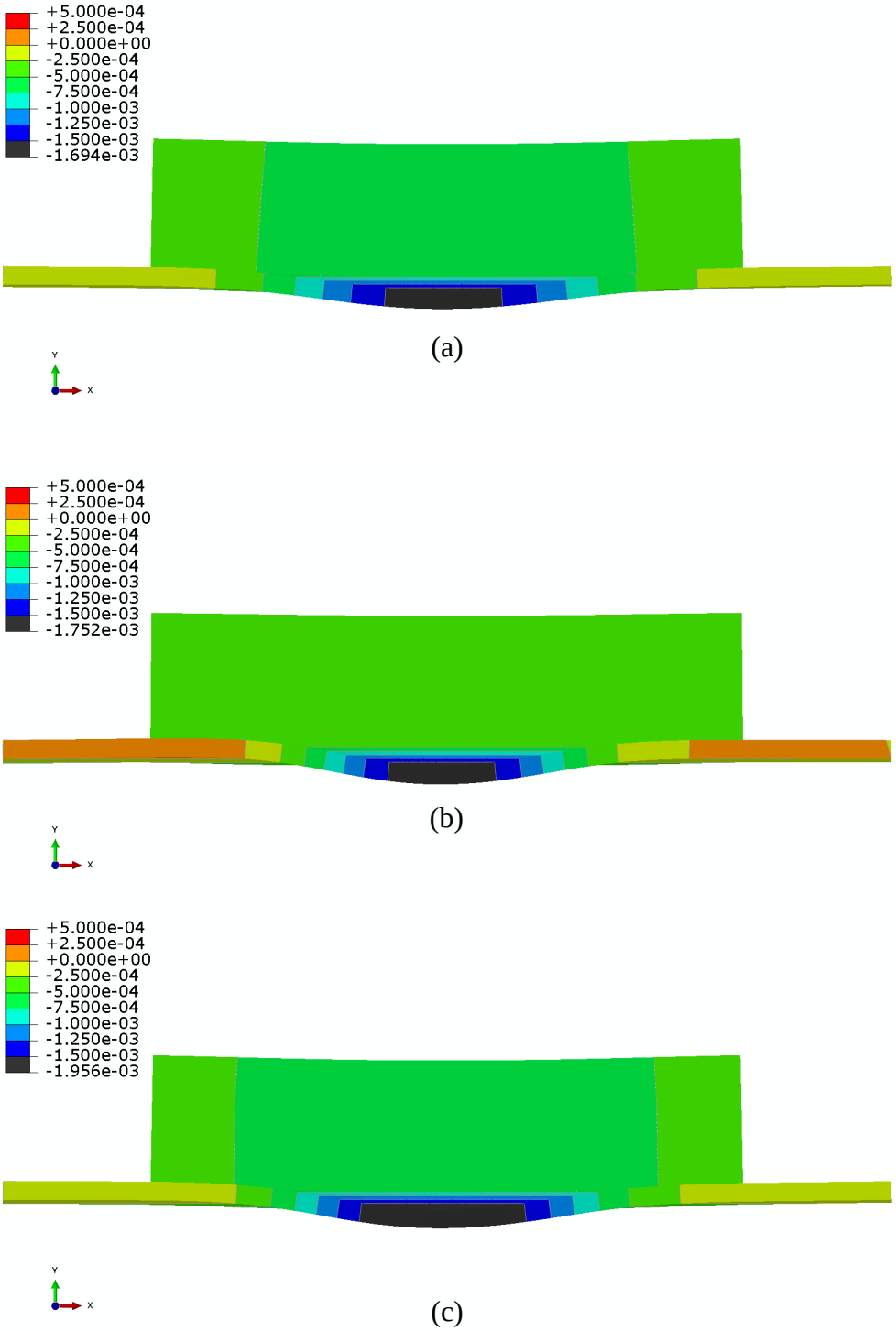

Figure 56. Displacement in y direction (in mm) after unclamping
(a) 1480W (b) 1850W (Original) (c) 2220W

Interlayer dwell time

The dwell time between the deposition allows some heat dissipation from the part during the building process and prevents heat accumulation. This improves the quality of the weld and the part since decreasing the dwell time causes instable arc due to high temperatures in the part as well as warpage in the part. Increasing the dwell time excessively would increase the building time significantly and will cause higher thermal gradients thus generating columnar grains in the material. Figure 57 shows the temperature effects of increasing and reducing the dwell time of the WAAM process. Utilizing a dwell time less than 50s was not possible due to convergence issues resulting from excessive heat accumulation.

Decreasing the dwell time to 50s (16.7% decrease) increases the maximum temperature in the model by 4.5%. Both models with 60 and 50 seconds of dwell time experience the maximum temperature during the 10^{th} layer. On the other hand, increasing the dwell time to 2 min (100% increase) decreased the maximum temperature by about 24.1%. In this case, the maximum temperature point occurred during the deposition of the first layer unlike the other two models.

Figure 58 shows the longitudinal stress when changing the dwell times before unclamping. Increasing the interlayer interval results in decreasing the stresses in the part. Using shorter dwell time results in a smaller difference between current and previous layers, see Figure 59, making the temperature distribution more uniform producing larger high stress areas. However, the decrease in stress is marginal. After unclamping, as seen in Figure 60, the decrease in stress is more prominent when increasing the dwell times. Figure 60a shows higher compressive stresses at the fine-coarse microstructure interface, while Figure 60b demonstrates more compressive stresses at the top of the part. The overall longitudinal stress is lower when longer dwell intervals are used.

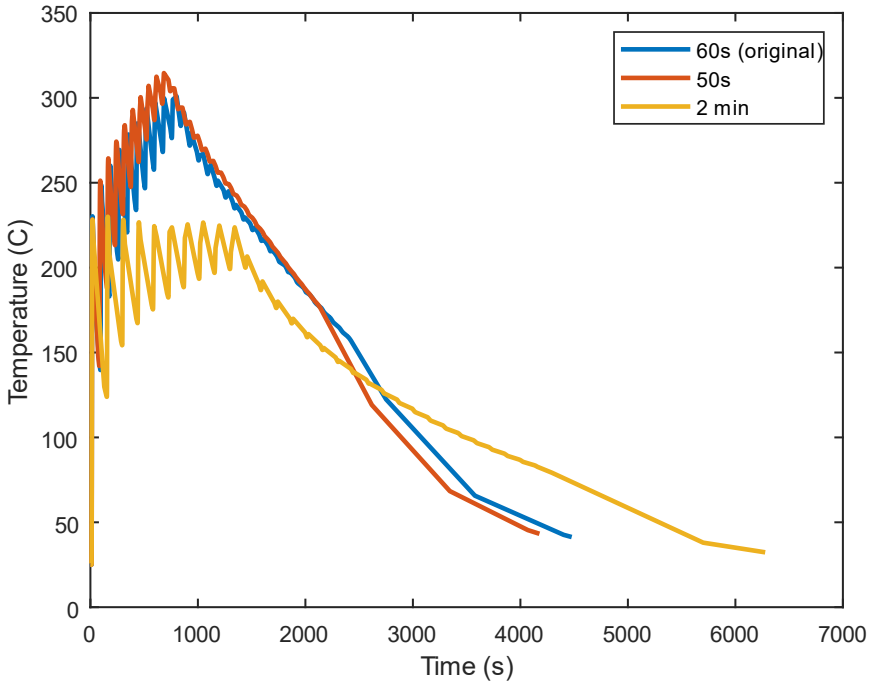

Figure 57. Temperatures at thermocouple 3 location using different dwell times

Similar behavior is observed build direction stress after unclamping, see Figure 62. However, the fixed 2-minute dwell interval model suffers from high tensile stress regions at the bottom of the wall, as illustrated in Figure 61. This is the results of the higher temperature differential between the deposited layer and previous layers which causes more localized high stress areas when using a longer dwell time, see Figure 59.

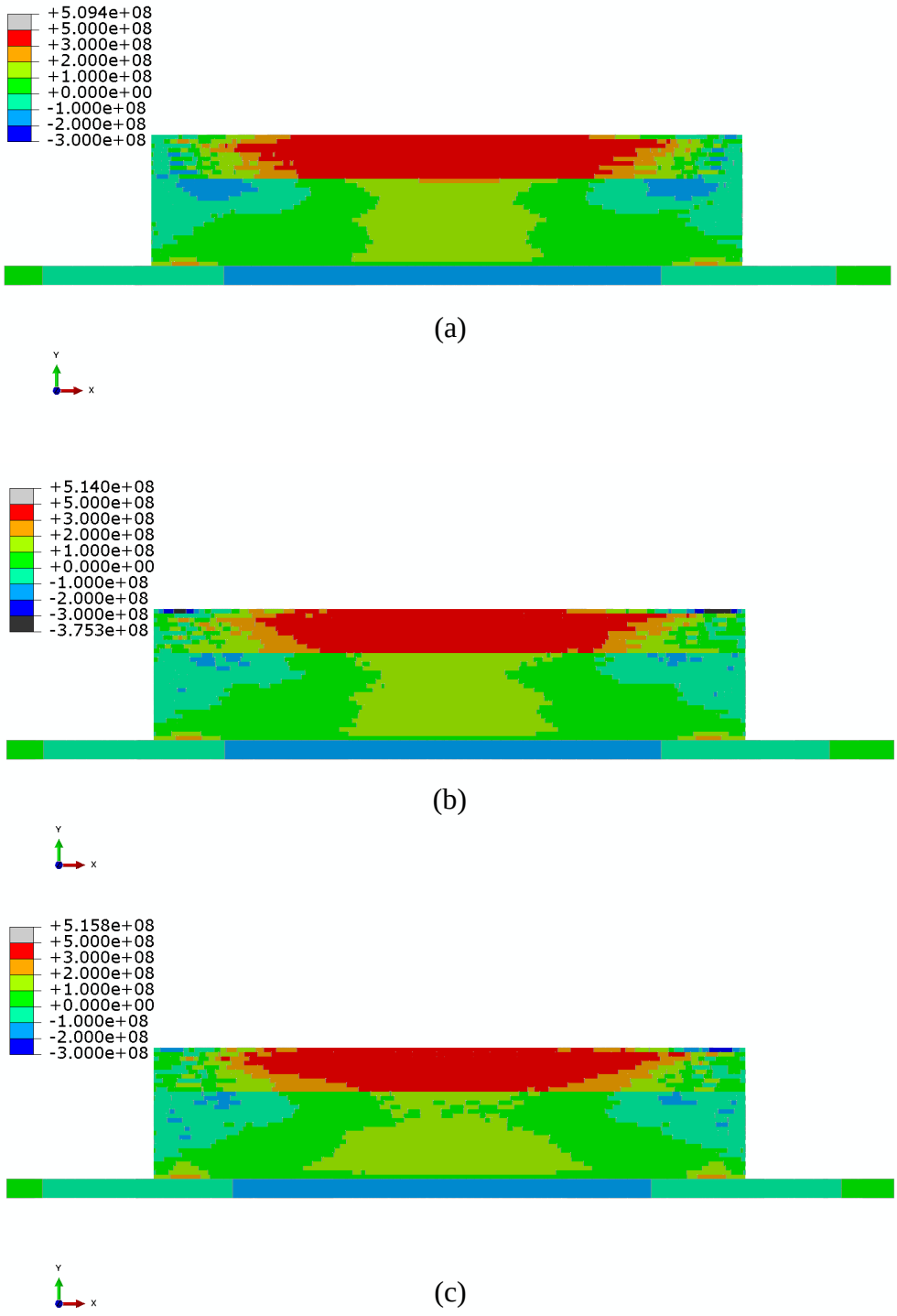

Figure 58. Longitudinal stress distribution before unclamping
(a) 50 seconds (b) 1 minute (Original) (c) 2 minutes

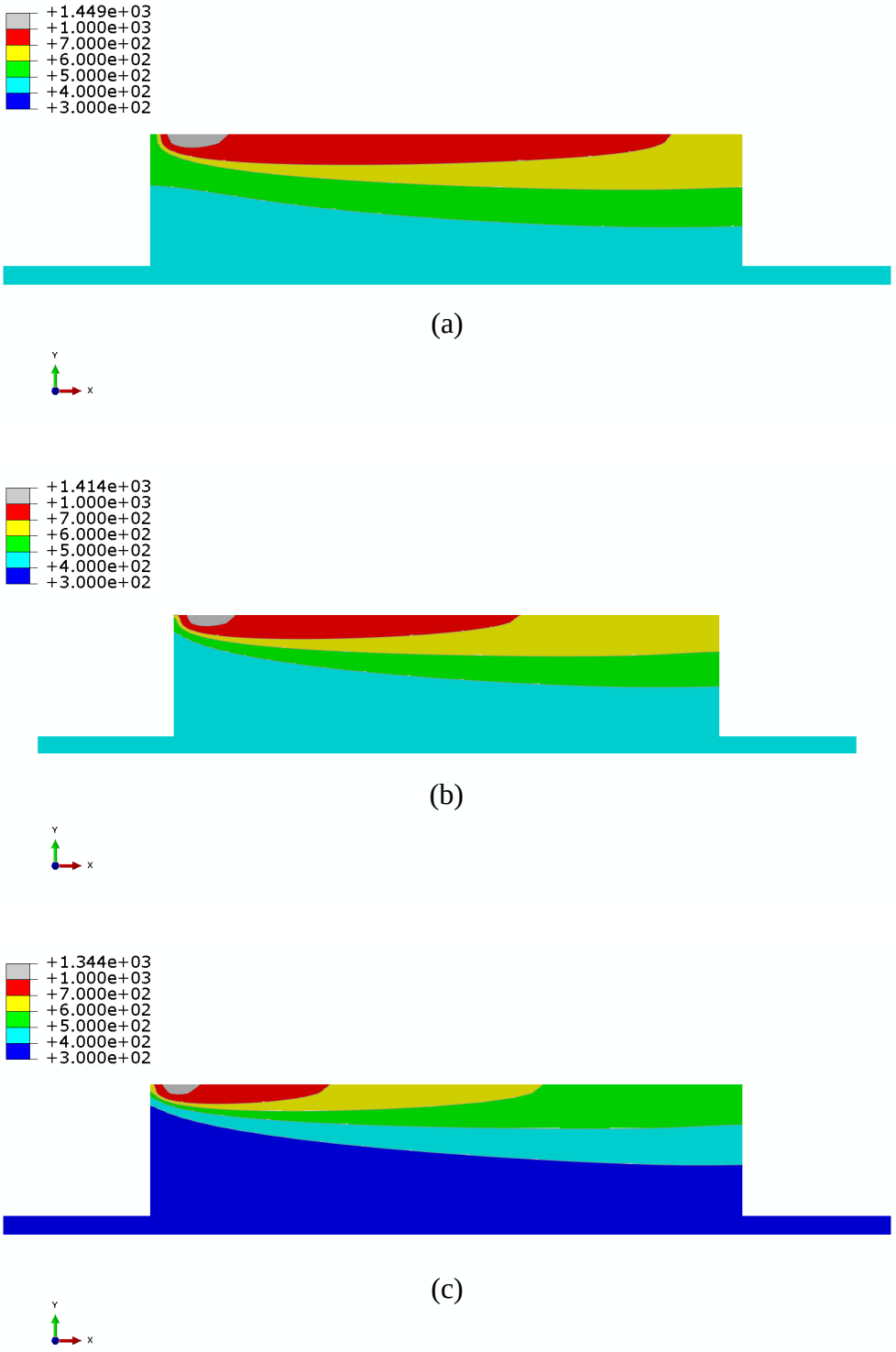

Figure 59. Temperature distribution at the end of the deposition of the 30th layer (a) 50 seconds (b) 1 minute (Original) (c) 2 minutes

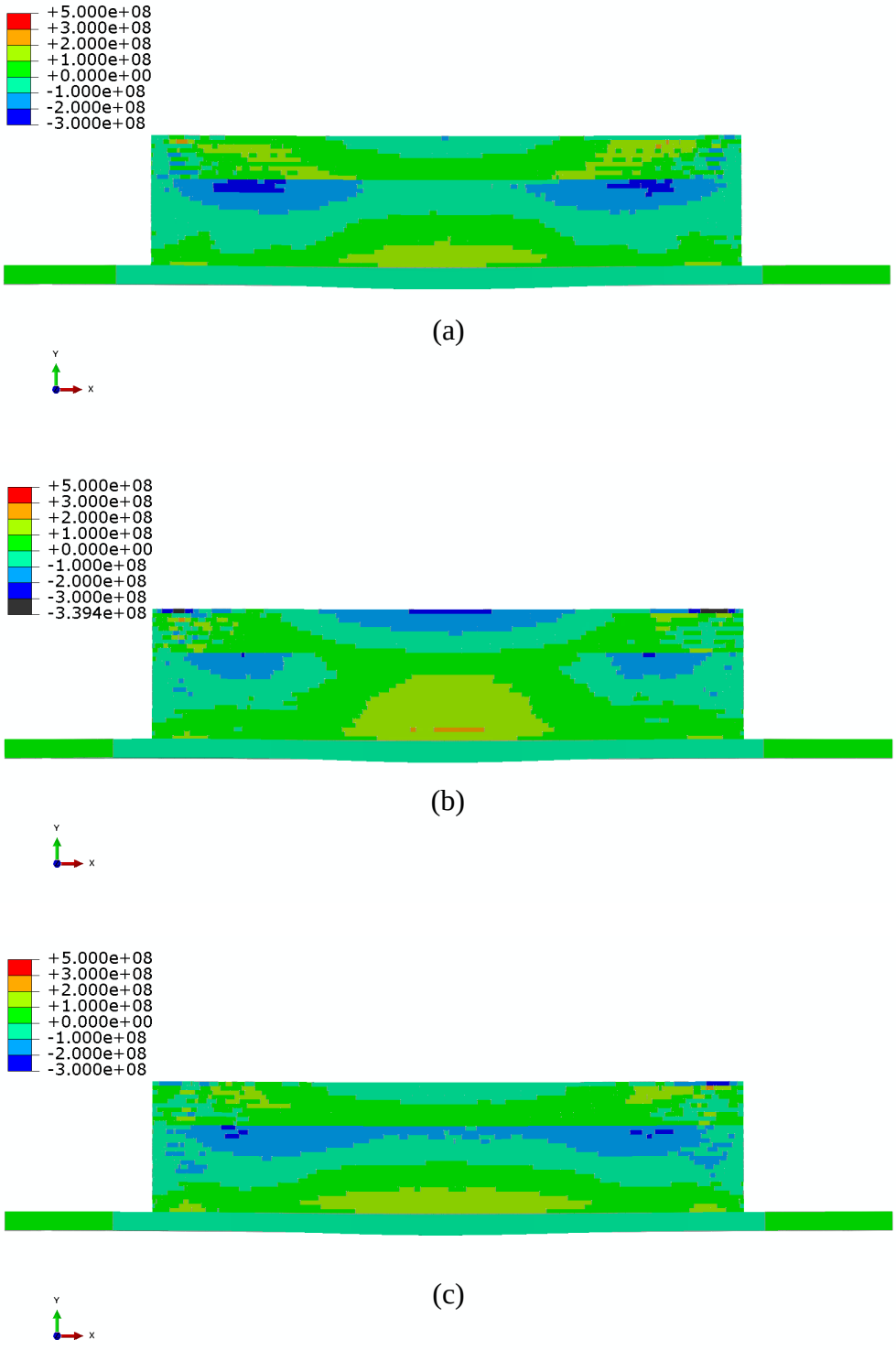

Figure 60. Longitudinal stress distribution after unclamping
(a) 50 seconds (b) 1 minute (Original) (c) 2 minutes

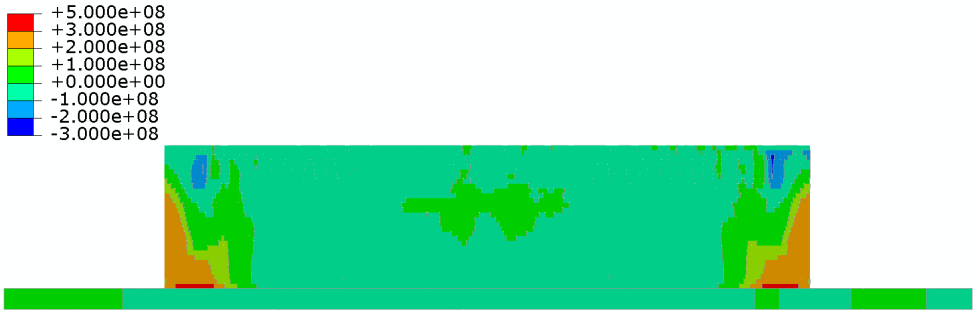

(a)

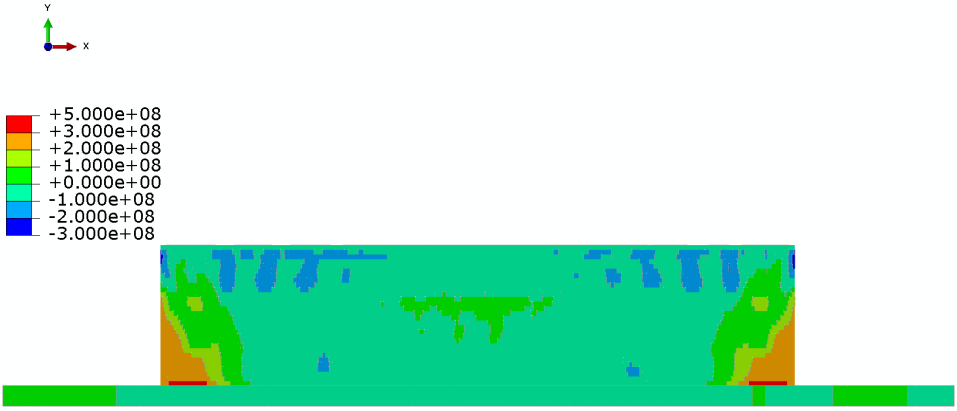

(b)

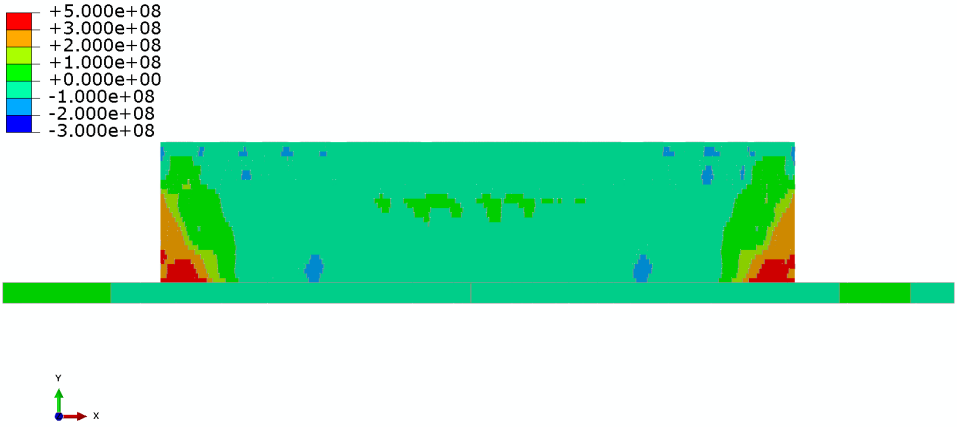

(c)

Figure 61. Build direction stress distribution before unclamping
(a) 50 seconds (b) 1 minute (Original) (c) 2 minutes

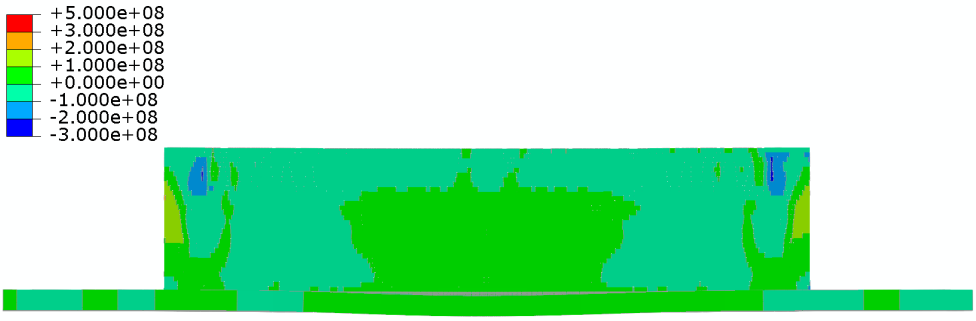

(a)

(b)

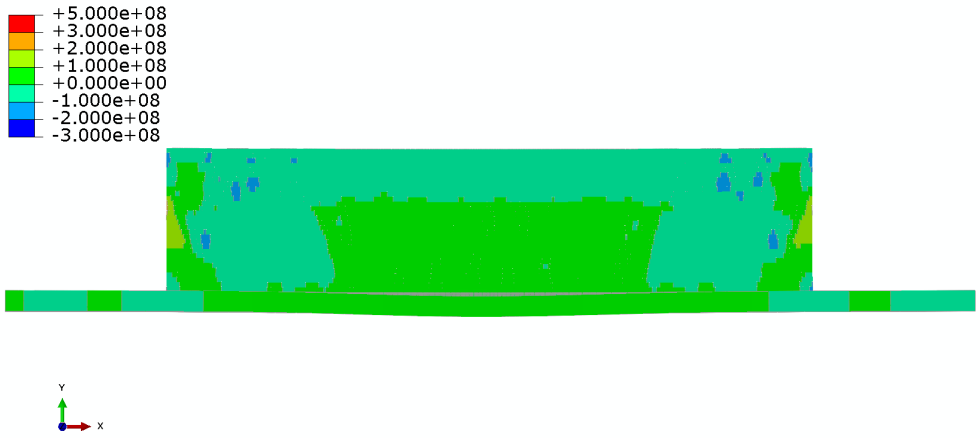

(c)

Figure 62. Build direction stress distribution after unclamping
(a) 50 seconds (b) 1 minute (Original) (c) 2 minutes

As illustrated in Figure 63, decreasing the dwell time to 50 seconds increased the vertical displacement by 14.1% with a maximum deflection of about 2 mm. Furthermore, increasing the dwell time to 2 minutes increased the deflection by 6.3% with a maximum vertical deflection of 1.863 mm. Using 1 minute of dwell time minimizes distortion and maximum deflection in the part.

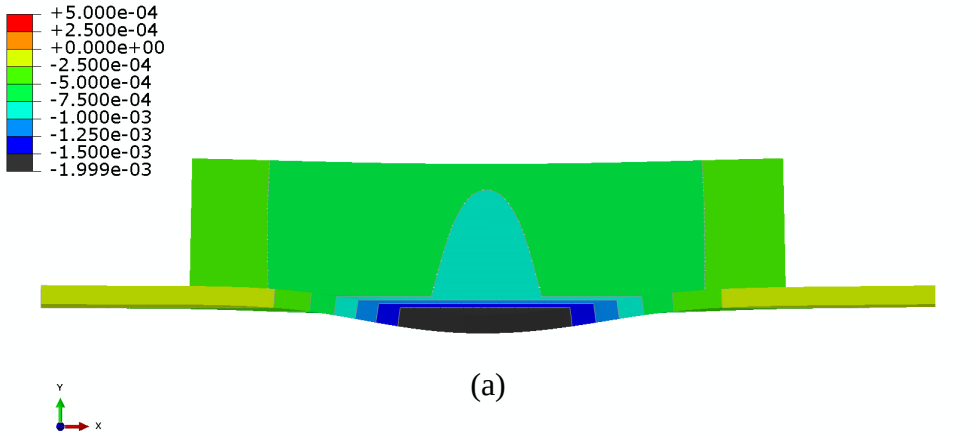

(a)

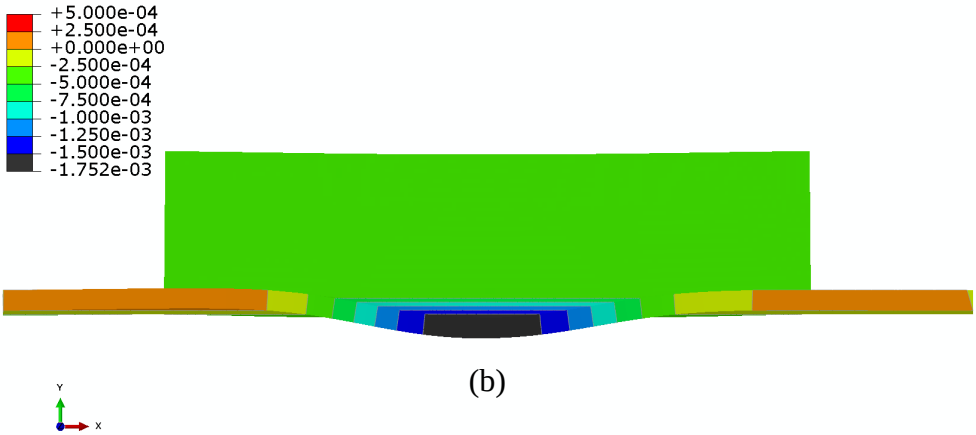

(b)

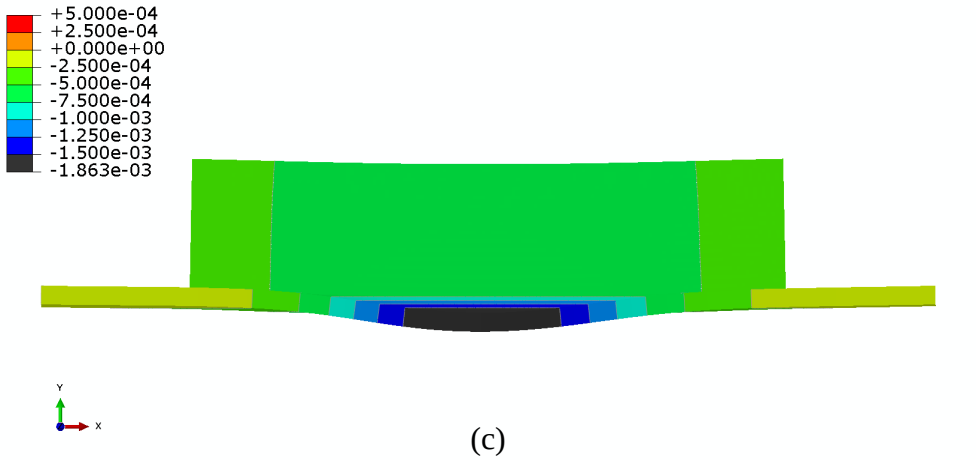

(c)

Figure 63. Displacement in y direction (in mm) after unclamping
(a) 50 seconds (b) 1 minute (Original) (c) 2 minutes

V. CONCLUSION AND FUTURE WORK

In conclusion, the thermal and mechanical simulations have shown accurate results as they are verified by the experimental data. Fluid flow in the weld pool is essential for the microstructure simulation and it is beyond the capabilities of ABAQUS software. The tensile longitudinal stress flattens out at the top 10 layers before unclamping. The tensile stress imposes compressive stress in the lower layers. After unclamping, residual stress is redistributed, leaving compressive stresses at the top layers. A parametric study has been conducted in research to understand the effect of various process parameters on temperature, stress and distortions in WAAM part, which include: the heat source travel speed, the input power, and the interlayer dwell time. The main outcomes are listed as follows:

- Process parameters, travel speed, the input power, and the interlayer dwell time, influence the thermal and stress profiles in various degrees
- The travel speed has a direct relation with stress in both the longitudinal and build directions due to uneven contraction of the material. Its effect on strength is significant.
- The distortion is directly disproportional with deposition speed before and after unclamping
- Using higher deposition speeds reduces warpage considerably
- Weld torch power has a direct relation with the longitudinal and build direction stresses as well as deformation of the part after unclamping
- The stress decreases with increasing dwell times, which is the results of a more uniform temperature distribution inducing larger high stress regions. Nevertheless, the higher 2-minute shows high tension zones at the bottom of the part in the build direction when fixed since the temperature differential is higher causes more localized stress

Future work includes formulating a fluid flow model to more accurately predict the thermal and microstructural profile. The effects of process parameters on RS can be further investigated including wider range and more granular incrementation of the parameter values. Also, the effect of the microstructure implementation should be adapted to the actual microstructure using different parameters. Additionally, this verified numerical model can be used to test techniques meant to reduce RS and distortion such as the utilization of a localized preheating torch or high-pressure gas nozzle for aftercooling.

REFERENCES

[1] T. DebRoy, H.L. Wei, J.S. Zuback, T. Mukherjee, J.W. Elmer, J.O. Milewski, A.M. Beese, A. Wilson-Heid, A. De, W. Zhang, Additive manufacturing of metallic components – Process, structure and properties, Prog. Mater. Sci. 92 (2018) 112–224.

[2] V. Bhavar, P. Kattire, V. Patil, S. Khot, K. Gujar, R. Singh, A review on powder bed fusion technology of metal additive manufacturing, Addit. Manuf. Handb. Prod. Dev. Def. Ind. (2017) 251–261.

[3] M.K. Imran, S.H. Masood, M. Brandt, S. Bhattacharya, J. Mazumder, Direct metal deposition (DMD) of H13 tool steel on copper alloy substrate: Evaluation of mechanical properties, Mater. Sci. Eng. A. 528 (2011) 3342–3349.

[4] A. Hehr, C. Waters, M. Norfolk, Ultrasonic Additive Manufacturing State-of-the-Art, (2018) 262–264.

[5] J. Cao, M.A. Gharghouri, P. Nash, Finite-element analysis and experimental validation of thermal residual stress and distortion in electron beam additive manufactured Ti-6Al-4V build plates, J. Mater. Process. Technol. 237 (2016) 409–419.

[6] C.R. Cunningham, J.M. Flynn, A. Shokrani, V. Dhokia, S.T. Newman, Invited review article: Strategies and processes for high quality wire arc additive manufacturing, Addit. Manuf. 22 (2018) 672–686.

[7] R. Morgan, C.J. Sutcliffe, W. O'Neill, Density analysis of direct metal laser re-melted 316L stainless steel cubic primitives, J. Mater. Sci. 39 (2004) 1195–1205.

[8] W.E. King, H.D. Barth, V.M. Castillo, G.F. Gallegos, J.W. Gibbs, D.E. Hahn, C. Kamath,

A.M. Rubenchik, Observation of keyhole-mode laser melting in laser powder-bed fusion additive manufacturing, J. Mater. Process. Technol. 214 (2014) 2915–2925.

[9] K. Darvish, Z.W. Chen, T. Pasang, Reducing lack of fusion during selective laser melting of CoCrMo alloy: Effect of laser power on geometrical features of tracks, Mater. Des. 112 (2016) 357–366.

[10] L.N. Carter, M.M. Attallah, R.C. Reed, Laser powder bed fabrication of nickel-base superalloys: Influence of parameters; characterisation, quantification and mitigation of cracking, Proc. Int. Symp. Superalloys. (2012) 577–586.

[11] T. Mukherjee, W. Zhang, T. Debroy, An improved prediction of residual stresses and distortion in additive manufacturing, Comput. Mater. Sci. 126 (2017) 360–372. https://doi.org/10.1016/j.commatsci.2016.10.003.

[12] S.W. Williams, F. Martina, A.C. Addison, J. Ding, G. Pardal, P. Colegrove, Wire + Arc Additive Manufacturing, Mater. Sci. Technol. 32 (2016) 641–647.

[13] J. Hu, H.L. Tsai, Heat and mass transfer in gas metal arc welding. Part I: The arc, Int. J. Heat Mass Transf. 50 (2007) 833–846.

[14] K.S. Derekar, A review of wire arc additive manufacturing and advances in wire arc additive manufacturing of aluminium, Mater. Sci. Technol. (United Kingdom). 34 (2018) 895–916.

[15] R. Baker, Method of making decorative articles, US Pat. (1925) 1–3.

[16] A. Ujiie, US3558846A - Method of and apparatus for constructing substantially circular cross section vessel by welding, Google Patents. (1966).

[17] R. Acheson, Automatic welding apparatus for weld build-up and method of achieving weld

build-up, (1990).

[18] B. Wu, Z. Pan, D. Ding, D. Cuiuri, H. Li, J. Xu, J. Norrish, A review of the wire arc additive manufacturing of metals: properties, defects and quality improvement, J. Manuf. Process. 35 (2018) 127–139.

[19] B. Cong, J. Ding, S. Williams, Effect of arc mode in cold metal transfer process on porosity of additively manufactured Al-6.3%Cu alloy, Int. J. Adv. Manuf. Technol. 76 (2015) 1593–1606.

[20] C.G. Pickin, K. Young, Evaluation of cold metal transfer (CMT) process for welding aluminium alloy, Sci. Technol. Weld. Join. 11 (2006) 583–585.

[21] Y. Ali, S. Barnikol-Oettler, J. Reimann, J. Hildebrand, P. Henckell, J.P. Bergmann, Wire Arc Additive Manufacturing of Hot Work Tool Steel with CMT Process, J. Mater. Process. Technol. 269 (2019) 109–116.

[22] H. Geng, J. Li, J. Xiong, X. Lin, F. Zhang, Optimization of wire feed for GTAW based additive manufacturing, J. Mater. Process. Technol. 243 (2017) 40–47.

[23] F. Martina, J. Mehnen, S.W. Williams, P. Colegrove, F. Wang, Investigation of the benefits of plasma deposition for the additive layer manufacture of Ti-6Al-4V, J. Mater. Process. Technol. 212 (2012) 1377–1386.

[24] J.J. Lin, Y.H. Lv, Y.X. Liu, B.S. Xu, Z. Sun, Z.G. Li, Y.X. Wu, Microstructural evolution and mechanical properties of Ti-6Al-4V wall deposited by pulsed plasma arc additive manufacturing, Mater. Des. 102 (2016) 30–40.

[25] T.A. Rodrigues, V. Duarte, R.M. Miranda, T.G. Santos, J.P. Oliveira, Current Status and

Perspectives on Wire and Arc Additive Manufacturing (WAAM), Materials (Basel). 12 (2019) 1121. https://doi.org/10.3390/ma12071121.

[26] F. Wang, S. Ganguly, P.M. Sequeira Almeida, J. Mehnen, J. Ding, P. Colegrove, S. Williams, Thermo-mechanical analysis of Wire and Arc Additive Layer Manufacturing process on large multi-layer parts, Comput. Mater. Sci. 50 (2011) 3315–3322. https://doi.org/10.1016/j.commatsci.2011.06.023.

[27] L.D. Cozzolino, F. Martina, J. Fairman, H. Mamash, P.A. Colegrove, T. Kashoob, H.E. Coules, Microstructure and residual stress improvement in wire and arc additively manufactured parts through high-pressure rolling, J. Mater. Process. Technol. 213 (2013) 1782–1791.

[28] N. Hoye, H.J. Li, D. Cuiuri, A.M. Paradowska, Measurement of Residual Stresses in Titanium Aerospace Components Formed via Additive Manufacturing, Mater. Sci. Forum. 777 (2014) 124–129.

[29] J. Zhang, X. Wang, S. Paddea, X. Zhang, Fatigue crack propagation behaviour in wire+arc additive manufactured Ti-6Al-4V: Effects of microstructure and residual stress, Mater. Des. 90 (2016) 551–561.

[30] M.T. Hutchings, P.J. Withers, T.M. Holden, T. Lorentzen, Introduction to the characterization of residual stress by neutron diffraction, CRC Press, 2005.

[31] S. Jayanath, A. Achuthan, A Computationally Efficient Finite Element Framework to Simulate Additive Manufacturing Processes, J. Manuf. Sci. Eng. 140 (2018) 041009.

[32] D. Deng, FEM prediction of welding residual stress and distortion in carbon steel

considering phase transformation effects, Mater. Des. 30 (2009) 359–366.

[33] D. Radaj, Heat Effects of Welding, 1992. https://doi.org/10.1007/978-3-642-48640-1.

[34] R.L. Ash, (MAE 607 Lecture Notes), 2018.

[35] E.M. van der Aa, Local cooling during welding: Prediction and control of residual stresses and buckling distortion, 2007.

[36] E.M. van der Aa, Local cooling during welding: Prediction and control of residual stresses and buckling distortion, 2007.

[37] H.L. Wei, T. Mukherjee, T. DebRoy, Grain Growth Modeling for Additive, Proc. 6th Int. Conf. Recryst. Grain Growth, ReX GG 2016. (2016) 265–269.

[38] P. Promoppatum, S.C. Yao, P.C. Pistorius, A.D. Rollett, A Comprehensive Comparison of the Analytical and Numerical Prediction of the Thermal History and Solidification Microstructure of Inconel 718 Products Made by Laser Powder-Bed Fusion, Engineering. 3 (2017) 685–694.

[39] D. SIMULA, Abaqus 2016 Documentation, (2016).

[40] C. England, Recommended Values of Thermophysical Properties for Selected Commercial Alloys, 2002.

[41] B. Silwal, M. Santangelo, Effect of vibration and hot-wire gas tungsten arc (GTA) on the geometric shape, J. Mater. Process. Technol. 251 (2018) 138–145.

[42] P. Michaleris, J. Song, Sensitivity analysis and optimisation of thermo-elasto-plastic process with applications to welding side heater design, Comput. Eng. 4 (2003) 33–42.

[43] P. Michaleris, Modeling metal deposition in heat transfer analyses of additive manufacturing processes, Finite Elem. Anal. Des. (2014).

[44] M. Gouge, P. Michaleris, Thermo-Mechanical Modeling of Additive Manufacturing, First edit, Elsevier Inc., 2017.

[45] and M.B. JOHN GOLDAK, ADITYA CHAKRAVARTI, A New Finite Element Model for Welding Heat Sources, (1984).